
Rheology of Martian Lava Flows: An Experimental Approach

Magdalena Oryaëlle Chevrel



München 2013

Rheology of Martian Lava Flows: An Experimental Approach

Magdalena Oryaëlle Chevrel

Dissertation
an der Fakultät für Geowissenschaften
der Ludwig-Maximilians-Universität
München

vorgelegt von
Magdalena Oryaëlle Chevrel
aus Beaumont sur Lèze, France

München, den 18. Februar 2013

Erstgutachter: Prof. Dr. Donald Bruce Dingwell

Zweitgutachter: Dr. David Baratoux

Tag der mündlichen Prüfung: 08.05.13

*A Notre Mère,
La Terre.*

Contents

Abstract	5
Zusammenfassung	7
Résumé	9
List of Figures	11
List of Tables	13
1 Introduction	15
1.1 Martian volcanism: activity through history	17
1.2 Martian volcanism: iron-rich magmas	19
1.3 Rheology of Magma	22
1.4 Main tools and goals of this study	23
2 Effect of iron on viscosity: case study of the physical properties of CaAl₂Si₂O₈- CaMgSi₂O₆ - FeO - Fe₂O₃ melts: analogues for extra- terrestrial basalt	27
2.1 Introduction	31
2.2 Experimental methods	32
2.2.1 Starting material	32
2.2.2 High-temperature viscometry in air	33
2.2.3 High-temperature viscometry and loop fusion experiment under re- duced conditions	33
2.2.4 Low temperature viscometry	34
2.2.5 Differential scanning calorimetry (DSC) methodology	35
2.2.6 Samples redox state	36
2.3 Results	37
2.3.1 High temperature viscosity	37

2.3.2	Low temperature viscosity	40
2.3.3	The calorimetric glass transition temperatures and derived viscosity	41
2.3.4	Viscosity behavior over the entire temperature range	43
2.4	Discussion	44
2.4.1	Structure-property relations affecting viscosity	44
2.4.2	Effect of redox state	46
2.4.3	Experimental limitation for oxidized iron-rich melts	47
2.4.4	Applications to extra-terrestrial magmatism	48
2.5	Conclusion	49
3	Planetary lava flow rheology: a comparison of morphological and rheological methods	51
3.1	Introduction	55
3.2	Methods	57
3.2.1	Morphological analysis	57
3.2.2	Sampling and analytical methods	59
3.2.3	Crystallization sequence	60
3.2.4	Viscosity modeling	61
3.3	Results	64
3.3.1	Description of the flow morphology	64
3.3.2	Viscosity estimate from the morphology	64
3.3.3	Chemistry and Petrography	66
3.3.4	Crystallization sequence	69
3.3.5	Transient viscosity model of the crystallizing lava flow	71
3.4	Discussion	74
3.4.1	Implications for the rheological mapping of extra-terrestrial lava flows	75
3.5	Conclusion	77
4	Viscous flow behavior of tholeiitic and alkaline Fe-rich Martian Basalts	79
4.1	Introduction	83
4.2	Samples	85
4.3	Experimental methods	87
4.3.1	Melt preparation	87
4.3.2	Superliquidus viscometry under controlled oxygen fugacity	87
4.3.3	Chemical composition and redox state	88
4.3.4	Low temperature viscosity at the glass transition temperature	88
4.4	Results: compositions and redox state	89
4.4.1	Chemical compositions	89
4.4.2	Iron Redox-state	91
4.4.3	Evidence of immiscibility at high-temperature or phase separation during slow quenching?	91
4.5	Results: melt viscosity and comparison with models	94
4.5.1	Viscosity in the superliquidus regime	94
4.5.2	Calorimetric glass transition	98
4.5.3	Viscosity near the glass transition	100
4.5.4	Non-Arrhenian parameterization over the entire range of temperature	101
4.6	Discussion	101

4.7	Conclusion	107
4.8	Supplementary material	108
5	Conclusion	113
6	Outlook	117
7	Annex 1: Detailed experimental methods	121
8	Annex 2: Review of synthetic lunar lava viscosity	131
	Bibliography	160
	Acknowledgments	161

Abstract

In recent years, high-resolution topographic images from Mars' surface as well as mineralogical and chemical data, have rapidly become more accessible. Martian volcanic landforms are characterized by giant low slope shield volcanoes, abundant lava flood plains and long lava flows. *In-situ* rock analysis and remote sensing spectroscopy reveal mainly basaltic compositions with particularly high iron concentrations, distinct from terrestrial basalts. As yet, very little is known about the rheological properties of such iron-rich Martian magmas that are essential to understand magmatic processes. Understanding the chemical and physical contributions to lava rheology is fundamental to provide constraints on magma ascent and lava flow emplacement that shaped the volcanic landforms on Mars. This study provides an experimental investigation of the rheological properties of Martian lavas and discusses the diversity of compositions in terms of lava viscosity / flow morphology relationship. The effect of iron, and its redox state on silicate melt viscosity is experimentally investigated and the viscosities of five synthetic silicate liquids having compositions representative of the diversity of Martian volcanic rocks were measured under controlled ambient oxygen fugacity. The results highlight the low viscosity of the iron-rich Martian melts that is consistent with viscosity values derived from morphological observations. A solidified lava flow on Earth was studied by combining analyses of remote sensing images (as commonly done on Mars), as well as experimental investigations of the rheological properties of the sampled rocks, in order to describe the viscous behavior of lava as emplacement, cooling, and crystallization occur. We show that a cooling-limited basaltic flow seemingly stop flowing when it reaches a critical viscosity value that is function of crystals content and shapes. As a result, the lava apparent viscosity appears to be largely influenced by the details of the crystallization sequence and is not uniquely

and simply related to the bulk chemical composition of the erupted material. Variation of the chemical evolution of Martian primary mantle melts through the volcanic history is not large to produce an significant shift of the viscosity range that could be observed them from their morphologies. Low apparent viscosities inferred from lava flow morphology on Mars may in turn be attributed to lavas with primary mantle melt composition crystallizing high proportion of olivine and possibly forming spinifex textures. Higher viscosity values derived from the morphology are compatible with mildly alkaline or trachybasalts and do not necessarily imply the occurrence of silica-rich lavas.

Zusammenfassung

Über die letzten Jahre sind hochauflösende topographische Bilder der Oberfläche des Mars, sowie chemische und mineralogische Daten der Marsgesteine zunehmend verfügbar geworden. Die vulkanischen Formationen des Mars beinhalten gigantische Schildvulkane flacher Ausprägung, grosse Flutbasaltebenen und weitfließende Lavaströme. In-situ Analysen der Mars Gesteine und "Remote Sensing Spectroscopy" zeigen grösstenteils basaltische Zusammensetzungen, jedoch mit besonders hohem Eisengehalt, der Marsgesteine von terrestrischen Proben unterscheidet. Bis dato sind die rheologischen Eigenschaften dieser eisen-reichen Mars Magmen wenig erforscht. Das Verständnis der physikochemischen Parameter, die die Lava Rheologie beeinflussen, ist jedoch fundamental, um Magmaaufstieg und die Ablagerung von Lavaströmen auf dem Mars zu verstehen.

In dieser Studie wurden die rheologischen Eigenschaften marsianischer Laven experimentell untersucht und die Variabilität der natürlich vorkommenden Zusammensetzungen in Beziehung zu Lava-Viskosität und Lava-Morphologie gesetzt.

Der Effekt von Eisen und seines Redox Zustandes auf die Viskosität von Silikatschmelzen wurde experimentell untersucht. Unter kontrollierten Sauerstoffugazitäten wurden die Viskositäten von fünf synthetischen Silikatschmelzen untersucht, deren Zusammensetzungen repräsentativ für die Spannbreite der Zusammensetzungen der vulkanischen Gesteine des Mars ist. Die niedrige Viskosität der eisenreichen, marsähnlichen Schmelzen ist konsistent mit den Viskositätswerten, die durch morphologische Analysen bestimmt wurden. Als terrestrisches Analog wurde ein erkalteter Lavastrom mit Hilfe von fernerkundlichen Bildern, die in der gleichen Weise für Mars angewendet werden, sowie Messungen der Rheologie an Gesteinsproben dieser Lava untersucht, um Änderungen in der Viskosität während der Ablagerung, des Abkühlens und der Kristallisation zu charakterisieren. Laut

unserer Ergebnisse wird ein durch Abkühlen limitierter basaltischer Lavastrom aufgrund von erhöhtem Kristallgehalt und als Funktion von Kristallhabitus gestoppt. Die apparente Viskosität scheint daher grösstenteils von der Kinetik der Kristallisationssequenz beeinflusst und weniger von der Gesamtzusammensetzung des eruptierten Materials. Als Folge hätte die Variabilität in der Zusammensetzung der primären, marsianischen Mantelschmelzen über die vulkanische Historie keinen signifikanten Effekt auf die apparente Viskosität, die durch Lava-Morphologie-Analysen bestimmt wird. Niedrige apparente Viskositäten aus diesen Morphologie-Analysen erklären sich dadurch hauptsächlich als Folge von primären Mantelschmelzen, die einen hohen Anteil von Olivin kristallisieren und möglicherweise Spinifex Texturen ausbilden. Wenn Morphologieanalysen höhere Viskositäten ausgeben ist dies kompatibel mit schwach alkalinen Basalten oder Trachybasalten, bedeutet jedoch nicht notwendigerweise das Vorkommen felsischer Laven.

Résumé

Ces dernières années, des nouvelles données satellites de la surface de Mars de haute résolution (topographiques ainsi que minéralogiques et chimiques), sont devenues accessibles à la communauté scientifique. Sur Mars, les paysages volcaniques sont caractérisés par des volcans boucliers géants à pentes faibles, des plaines de lave et des longues coulées de lave. L'analyse des roches *in situ* et par spectroscopie orbitale révèlent que la composition des roches est essentiellement basaltique contenant une quantité de Fer particulièrement élevée, clairement distincte des basaltes terrestres. À ce jour, les propriétés rhéologiques des magmas martiens riches en Fer, qui sont essentielles pour comprendre les processus magmatiques, n'ont pas été étudiées en détails. Définir comment la teneur en Fer contrôle la rhéologie des laves est fondamental pour comprendre l'ascension des magmas et interpréter la mise en place des coulées de lave qui façonnent les paysages volcaniques sur Mars. Cette thèse fournit une étude expérimentale des propriétés rhéologiques des laves martiennes et discute de la diversité des compositions en termes de relation entre viscosité et morphologie des coulées.

L'effet du Fer et son état d'oxydo-réduction sur la viscosité des liquides silicatés sont étudiés expérimentalement et les viscosités de cinq laves ayant des compositions représentatives de la diversité des roches volcaniques martiennes ont été mesurées en fonction de la température. Les résultats mettent en évidence la faible viscosité de ces liquides martiens riches en fer, ce qui est compatible avec la viscosité déduite des observations morphologiques. Afin de décrire le comportement visqueux d'une coulée de lave pendant sa mise en place (refroidissement et cristallisation), une coulée terrestre a été étudiée, en combinant l'analyse des images de télédétection (comme on le fait sur Mars) et l'étude expérimentale des propriétés rhéologiques des roches échantillonnées. Nous montrons que

la forme des coulées basaltiques qui ont cessé d'avancer à cause de leur refroidissement, atteignent une limite rhéologique qui dépend des détails de la séquence de cristallisation et de la forme des cristaux. Leur viscosité apparente n'est pas uniquement et simplement liée à la composition chimique de la lave. Ainsi, l'évolution chimique des liquides primaires issus de la fonte partielle du manteau martien à travers l'histoire volcanique de Mars n'a pas d'effet significatif sur la viscosité apparente déterminée par la morphologie des coulées. Les faibles viscosités apparentes déduites de la morphologie des laves sur Mars peuvent être attribuées à des compositions de liquides primaires qui cristallisent des olivines en forte proportion et pouvant former une texture spinifex. Les viscosité plus élevées dérivées de la morphologie sont elles compatibles avec des basaltes légèrement alcalins ou trachytique et n'impliquent pas nécessairement la présence de laves riches en silice de type andésitique.

List of Figures

1.1	Mars global volcanism distribution	17
1.2	Volume and chronology of Martian volcanism	19
1.3	Primitive mantle composition of Mars and of the Earth	20
1.4	Iron content of primary melts from the Martian mantle	21
2.1	Method to estimate T_f' and heat capacity curves for AD-10 at various cooling	35
2.2	Iron redox state as a function of oxygen fugacity for the set of samples AD-10	36
2.3	Temperature dependence of viscosity of the iron-bearing AD melts	37
2.4	Viscosity variation as a function of total Fe_2O_3 in mol. %	39
2.5	Enthalpy variation vs. total Fe_2O_3	40
2.6	Variation of the glass transition temperature vs. total Fe_2O_3 and redox state	42
2.7	Viscosity calculated at T_f' for the iron-bearing AD melts	43
2.8	Isothermal viscosity curves as a function of the degree of polymerization . .	46
2.9	Viscosity of basaltic melts experimentally determined, comparison between this study and terrestrial and lunar data.	48
3.1	Location of the lava flow in the Western Volcanic Zone (WVZ), Iceland . .	58
3.2	Data Elevation Model of the distal section of the lava flow and topographic cross-section of the profiles	65
3.3	Petrographic analyses of the sample	68
3.4	Crystallization sequence as a function of temperature	70
3.5	Apparent viscosity of the crystallizing lava as a function of temperature . .	72
3.6	Apparent yield strength of the crystallizing lava as a function of the tem- perature	73
4.1	Total Alkalies and FeO_{tot}/MgO ratio vs. Silica content of Martian rock com- positions	84
4.2	Electron microprobe analyses (FeO vs. SiO_2) of the Martian synthetic melts	90
4.3	Back Scattered Electron images of IAMB-S4 glass chip	91
4.4	Redox state (FeO/FeO_{tot}) of the melts as a function of the ambient fO_2 . .	92
4.5	Chemical profile across the OMB-S2 glass	93

4.6	The viscosity at superliquidus regime of the investigated melts as a function of their redox state expressed as $\text{FeO}/\text{FeO}_{\text{tot}}$	97
4.7	Comparison of the measured viscosity with empirical models	97
4.8	Heat capacity curves of the Martian melts	99
4.9	Viscosity of basalts from Mars, Moon and Earth	102
4.10	Crystallization sequence at 1bar and QFM-1 for all investigated compositions	104
4.11	Apparent viscosity of crystallizing Martian lavas as a function of temperature	106
4.12	BSE images of IAMB-S1	112
7.1	Calibration for Concentric Cylinder method	125
7.2	Scheme of the gas-tight vertical tube furnace	126
7.3	Example of temperature calibration for the box furnace at a thermocouple immersion of 2.5 cm.	127
7.4	Screen caption of the interface of the ViscosityLauman software	128
7.5	Estimation of the limiting fictive temperature	129
8.1	Composition of Lunar sample	133
8.2	Viscosity measurements collected from the literature.	134
8.3	Viscosity measurements collected from the literature.	135
8.4	Comparison of the experimental data from the literature and estimation. .	136
8.5	Comparison of literature data with synthesized and measured by this study.	136

List of Tables

2.1	Chemical compositions of the iron-free and iron-bearing anorthite-diopside melts in wt. %	33
2.2	High- and low- temperature viscosities measured in air for the iron-bearing AD melts	38
2.3	Enthalpy variation calculated at high and low temperature and TVF parameters	39
2.4	Isothermal viscosity measurements under controlled fO_2	40
2.5	Glass transition temperatures collected at T_f' , the onset (T_g^{onset}), at the maximum (T_g^{peak}) and at the onset of the liquid field (T_g^{liquid})	41
3.1	Equations to calculate the yield strength as a function of crystal fraction. .	63
3.2	Geometric flow parameters and resulting lava flow viscosity and yield strength.	66
3.3	Bulk rock geochemical composition and petrological characteristic of the samples	67
3.4	Representative chemical compositions of the crystals.	69
3.5	Fitting parameters for calculation of the relative viscosity	71
4.1	Chemical composition of the investigated Martian synthetic melts.	86
4.2	Viscosity of the synthetic Martian melts at 1 atm in air and at under reduced oxygen fugacity.	95
4.3	Fitting parameters of the Arrhenian equation within the single superliquidus regime and near the glass transition	96
4.4	Effect of iron redox on the viscosity at superliquidus regime	96
4.5	Limiting fictive temperatures for all samples	98
4.6	Fitting parameters of the TVF equation for the oxidized and reduced melts	101
4.7	Electron microprobe analyses of the Martian synthetic melts	108
4.8	Electron microprobe analyses of crystals within IAMB-S1	112

CHAPTER **1**

Introduction

1.1 Martian volcanism: activity through history

The release of high-resolution topographic data of the planetary surface has offered new insight into the characteristics of volcanic landforms in the solar system. In particular, our understanding of the Martian volcanic history is essentially inferred from the morphological approach, including volume and effusion rate estimates and relative chronology, whereas the chemistry and mineralogy of volcanic rocks of the red planet are now also well documented.

Mars' accretion and differentiation into core, mantle and crust took place within a few tens of millions of years. Most of the subsequent geologic activity was confined to the first 1.5 Ga of its history (50 % of the surface is older than 3.5 Ga). The volcanic provinces represent 60 % of the surface (main volcanic provinces are highlighted in Figure 1.1) and volcanic evidences comprise shield volcanoes, domes and composite cones, highland pateras, volcano-tectonic features but also swamp of clusters of low volcanic shields and a great number of long lava flows and flood basaltic plains.

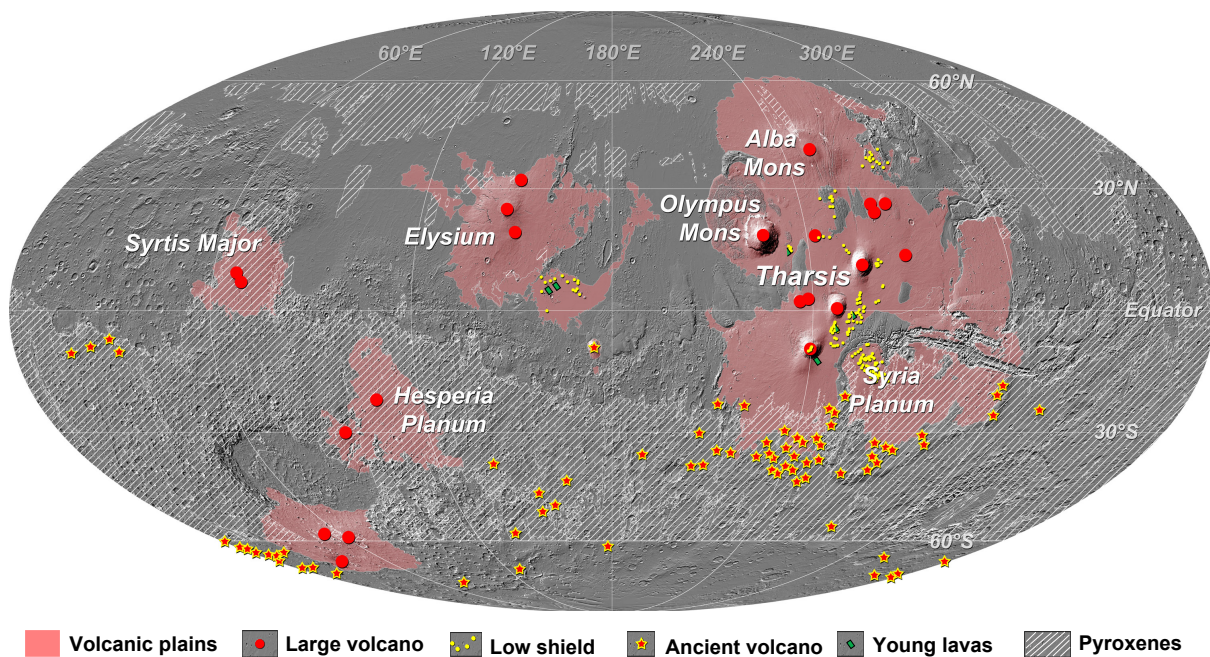


Figure 1.1: Distribution of the main volcanic provinces on Mars (Grott et al., 2013)

The heavy cratering and/or covering by more recent volcanism have left only sparse evidences of the volcanic activity in the early time of Mars, corresponding to the Noachian age (>3.8 Ga). The few volcanic landforms that still remain are some small edifices, called Tholi, mainly situated in the southern highlands. Despite the scarcity of geomorphic evidence for volcanism, most of the materials exposed in the cratered uplands are probably primary volcanic rocks reworked by impacts (Bandfield et al., 2000; Mustard et al., 2005;

Baratoux et al., 2013). During the Hesperian period (3.8 - 3.2 Ga), the volcanic activity resulted in the resurfacing of approximately 30 % of the planet and is now largely observable in the form of extensive lava plains, large low shield-like edifices, known as Paterae and giant shield volcanoes (Greeley and Spudis, 1981). The large areas covered by lava plain results from flood basaltic activity with probably high effusion rates. The Paterae (e.g., Apollonaris, Alba, Peneus, Hadriaca, Amphitrites, etc...) are characterized by large calderas that suggest explosive volcanism (Greeley and Crown, 1990; Hynes et al., 2003) although recent studies showed that the density of such volcanoes is too high to be made out of pyroclastic material and a effusive origin is now favored (Grott and Wieczorek, 2012). The giant shield volcanoes, the Mons (Olympus, Arsia, Pavonis, Ascreus, Elysium), are build by low viscosity lavas that have probably started to accumulate in this period or even earlier, though they expose young surfaces of only a few hundreds of million years (Werner, 2005; Vaucher et al., 2009a, Figure 1.2). The volcanic activity in the last two thirds of the Martian history, corresponding to the Amazonian period that extends from approximately 3.2 Ga ago (the middle of the terrestrial Archean era) to present, was considerably reduced. The large shield volcanoes continued slowly to grow and lava plains continued to accumulate here and there. Dating of volcanic features suggests that the eruption rate was highly episodic (Neukum et al., 2004; Wilson, 2001; Werner, 2009). Recently, small lava flows and swamp of small shield volcanoes, mainly localized in Tharsis and Central Elysium Planitia volcanic provinces, were dated of only tens of millions of years old (Hartmann et al., 1999; Vaucher et al., 2009b; Hauber et al., 2011). Mars could then still be episodically active, although at very low rates.

Characteristics of volcanic edifices, layered volcanoclastic deposits and mainly lava flow morphology are commonly used to interpret the volcanic activity in terms of eruption dynamics (magma volume, effusion rate and effusive vs. explosive activity) and to extract the rheological properties of the erupted material and consequently their nature (Pinkerton, 1987; Wilson and Head, 1994). With the increase of high-resolution images and data elevation models, interpretation of lava flows morphology, by the mean of simple rheological models, have been extensively used to infer the viscosity of lava flow. Typical viscosity values of Martian lava flows estimated in this way range from 10^2 to 10^8 Ps.s. These values are qualitatively compatible with effusive low viscosity magmas such as micro-basaltic to andesitic compositions (e.g. Zimbelman, 1985; Glaze et al., 2003; Hiesinger et al., 2007; Vaucher et al., 2009b; Hauber et al., 2011; Pasckert et al., 2012, and references therein). However, the simple isothermal rheological models (Newtonian or Binghamian) have not been validated considering the lack of independent constrains on Martian lava flow viscosity. This is an important issue for the interpretation of lava morphology in planetary science. How well are we able to interpret morphological ob-

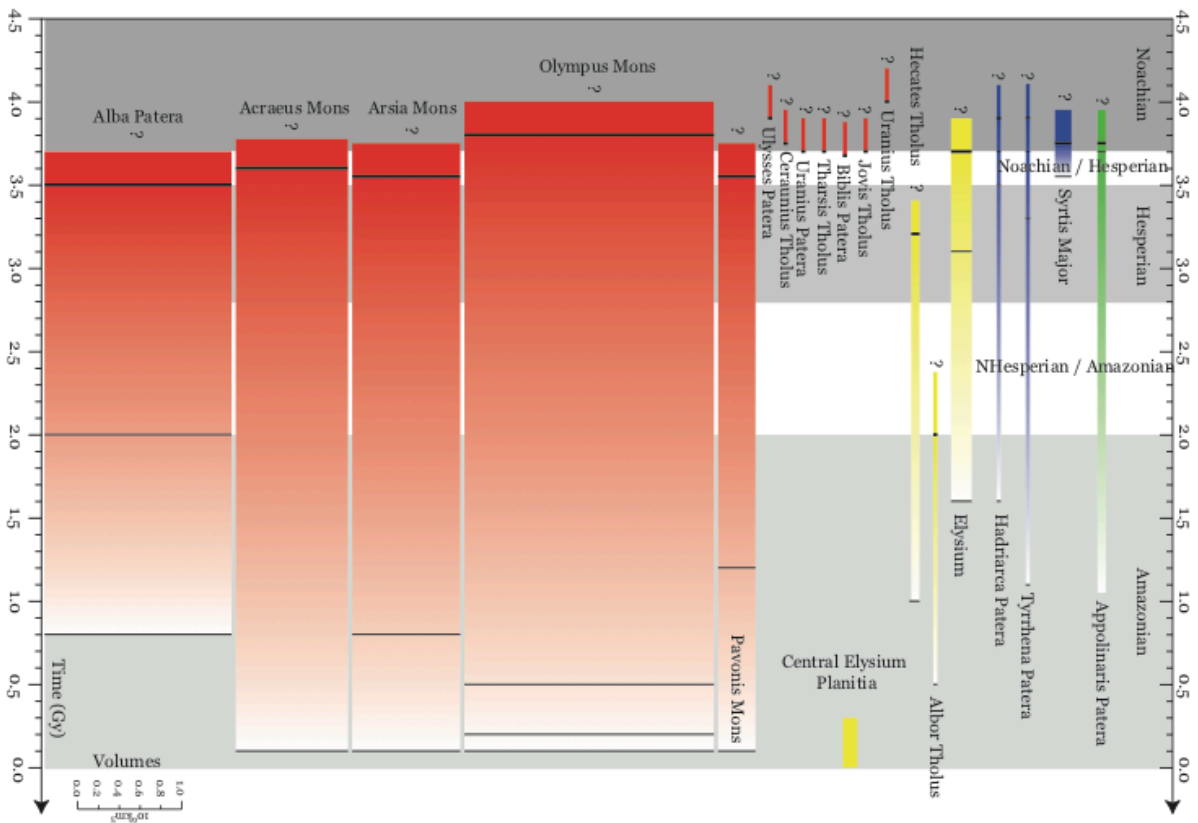


Figure 1.2: Volume and chronology of Martian volcanism (Vaucher et al., 2009)

servations in terms of lava rheology and hence composition? Are these interpretations consistent with the known compositions of Martian volcanic rocks?

1.2 Martian volcanism: iron-rich magmas

The chemical composition of Martian magmas is now well known from remote sensing chemical and mineralogical analyses of Mars surface, as well as from Martian meteorites and in-situ rock analyses. All data have confirmed the widespread occurrence of basaltic composition over the whole planet (e.g. Binder, 1976; Gellert et al., 2004; McSween, 2004; McSween et al., 2006a; Boynton et al., 2007; Bost et al., 2012; Grott et al., 2013). In details, most of the recognized compositions are iron-rich tholeiitic basalts and micro-basalt as well as iron-rich mildly alkali- and trachy-basalt (McSween et al., 2009). The chemical compositions of the Martian basalts are significantly enriched in iron (13 to 22 wt.% FeO_{tot}) with respect to terrestrial basalts (characterized by an average of FeO_{tot} abundance of 12 wt.%). This difference is attributed to the composition of the Martian mantle.

The mantle composition of the rocky planets depends on the concentration of elements

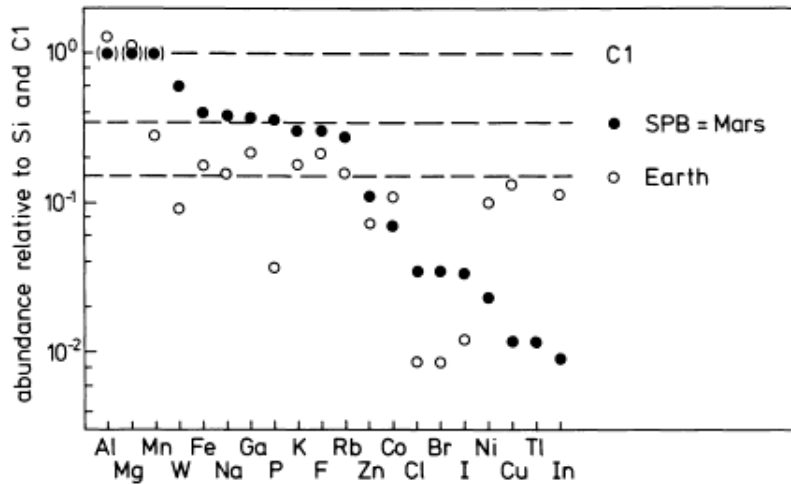


Figure 1.3: Primitive mantle composition of Mars and of the Earth, (Dreibus and Wänke, 1985)

present during accretion and on the degree of oxidation state that controls the partitioning between metallic iron that sinks in the core and iron oxide that stays in the mantle. As the concentration of volatiles increases with distance from the sun, the degree of oxidation would appear to increase simultaneously (Wänke, 1981). Since Mars is farther from the Sun than the Earth, it is then expected to be enriched in volatiles and would be therefore more oxidized at the stage of differentiation. Therefore, the partitioning between iron oxide and metallic iron would favor a smaller core and an iron-rich mantle relative to the Earth (Lewis, 1972; Dreibus and Wänke, 1984, 1985). This theoretical rationale was confirmed by several independent observations and approaches. Anderson (1972) indicated that a small core and an iron-rich mantle would be compatible with the moment of inertia of the planet. Lodders and Fegley (1997) and Sanloup et al. (1999) proposed a composition of the bulk Mars from a mixing-model of chondritic components, respectively (CI, CV, H) and (H, EH), constrained from the oxygen isotope ratios in the Martian meteorites (Lodders and Fegley, 1997). The abundances in Mg, Al, Si and Ca were calculated to compose the mantle with the stoichiometric amount of oxygen. The remaining oxygen is then combined with Fe. This calculation yields a Martian mantle enriched in iron with respect to the Earth, with a Mg number ($Mg\# = \text{molar Mg}/(\text{Mg} + \text{Fe})$ ratio) lesser than 0.80 (the terrestrial $Mg\#$ is 0.89). Dreibus and Wänke (1985) calculated Mars' mantle composition by assuming a chondritic abundance of the refractory lithophile elements in the mantle, and using the nearly constant Fe/Mn ratio in Martian meteorite, two elements which are not significantly fractionated during magmatic processes. They found that the Martian mantle contains twice as much Fe than the Earth's mantle ($Mg\# = 75$; Figure 1.3)

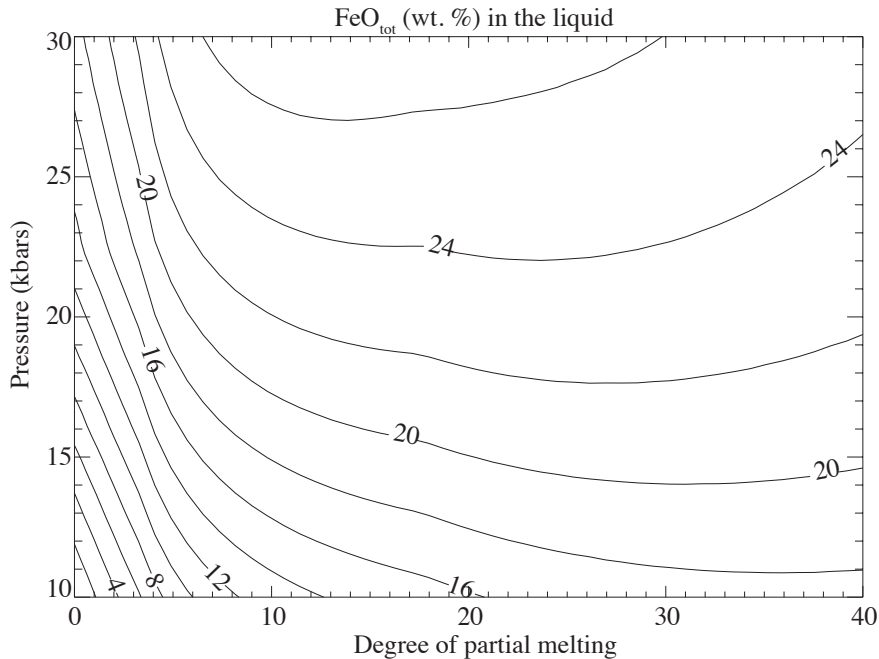


Figure 1.4: Iron content of primary melts from the Martian mantle formed over a wide range of possible conditions of partial melting. The lines represent primary melts isocomposition. The compositions of the primary melts were calculated according to Baratoux et al. (2011) using the primitive Martian mantle composition given by Dreibus and Wänke, (1985) and using pMELTS with applications of corrections for iron-rich compositions as described in El Maarry et al. (2009).

Additionally, Khan and Connolly (2008) confirmed the same Fe-rich composition from a global inversion of the second degree tidal Love number, the tidal dissipation factor, the mean density and the moment of inertia as given by Yoder (2003). Finally, this primitive mantle composition is now widely accepted as partial melts composition matches the mineralogy and chemistry of the Mars' surface (Bertka and Holloway, 1994; El Maarry et al., 2009; Baratoux et al., 2011). The occurrence of Fe-rich magmas is therefore not a bias in our current knowledge of the surface Mars. Such magmas were formed from early Mars until the most recent activity as describe by Baratoux et al. (2011) who confirms that Fe-rich melts result of a large range of possible conditions of mantle partial melting (Figure 1.4).

Moreover, Baratoux et al. (2011) showed that the chemical composition of the main volcanic provinces follows a trend that corresponds to the partial melting of the Martian mantle during the natural cooling of the mantle associated with the thickening of a stagnant lithosphere. In addition, the fact that Noachian rocks are characterized by significantly higher proportion of low calcium pyroxene while Hesperian surfaces contains large proportion of high calcium pyroxene (Mustard et al., 2005; Baratoux et al., 2007; Poulet et al., 2009) appear to be also explained by this thermal evolution of the interior of

the planet (Baratoux et al., 2013). Although, there is no particular mineralogy associated with Amazonian terrains, the elemental maps displays enrichment in Fe compare to older terrains, which is also consistent a deep origin of the source associated with colder mantle temperature in recent times (Baratoux et al., 2011).

Viscosity is intimately dependent on the chemical composition of the lava. The main target of this work is to investigate the viscosity of iron-rich Martian silicate melts and whether the diversity of Martian basalt compositions and the chemical variation over time are significant to affect the morphology of the lava flows?

1.3 Rheology of Magma

Viscosity is the main physical parameter affecting the evolution of molten bodies from their formation at great depth, during their ascent and emplacement as intrusions or at the surface as volcanic flows (e.g. Pinkerton and Stevenson, 1992; Dingwell, 1996). It controls the speed of magma ascent through the crust, the ease of crystal and bubble to grow, and therefore defines the type of eruption. Depending on the ambient pressure and temperature conditions and at lesser extend oxygen fugacity, the magma viscosity follows different flow paths and may range over tens of orders of magnitude (typically for volcanic products from 10^0 to more than 10^{14} Pa·s).

At high temperature, in superliquidus regime, magmas are liquids and their viscosity is Newtonian. The atomic scale flow mechanism of silicate liquids is thought to be controlled by the structural organization of the cation-oxygen network (Mysen, 1988; Mysen and Richet, 2005; Stebbins et al., 1995; Perchuk and Kushiro, 1991; Dingwell and Webb, 1990). To date, the viscosity-temperature relationship of silicate melts can be estimated from their composition (molar proportion of the major elements) by the mean of empirical models based on experimental viscosity measurements (Bottinga and Weill, 1970; Shaw, 1972; Hess and Dingwell, 1996; Giordano and Dingwell, 2003; Hui and Zhang, 2007; Giordano et al., 2008). The most recent models are calibrated using a large set of volcanic melts covering basaltic to rhyolitic compositions. However, they do not incorporate Fe-rich Martian-like compositions. Previous studies have investigated the effect of iron on viscosity for binary or tertiary systems (e.g. Dingwell and Virgo, 1987; Mysen and Virgo, 1989; Dingwell and Webb, 1990) or for industrial slag purpose (e.g. Kondratiev et al., 2008) but only few measured the viscosity of iron-rich terrestrial basalts (e.g. Bouhifd et al., 2004; Toplis et al., 1994) and iron-rich lunar basalts (e.g. Murase and McBirney, 1970; Cukierman et al., 1972, 1973; Uhlmann et al., 1974; Uhlmann and Klein, 1976; Handwerker et al., 1978). Although, iron is expected to lower the viscosity of silicate melts, which is compatible with low viscosity lava observed on Mars, quantitative inves-

tigation must be conducted to improve our understanding of Martian melt behavior and volcanic dynamism on Mars.

Furthermore, magmas are polyphasic systems made of a viscous melt and suspended particles. The presence of particles (either crystals or bubbles) within the magma affects dramatically the viscosity. Magma viscosity is thus a combination of complex geochemical and physical interactions strongly dependent on the chemical composition of the melt, temperature, volatile content and crystal and bubble content. When the lava is extruded, gas exsolves and bubbles nucleate and the heat lost induces crystallization and consequently, changes in the residual liquid composition, which, in combination, may increase the apparent viscosity of the flow by several orders of magnitude. The rheological implication of increasing crystal content in the lava involves that the viscosity is no longer controlled by the melt but by the particles network and become non-Newtonian, strain-rate dependent (Caricchi et al., 2007; Lavallée et al., 2007; Costa et al., 2009; Petford, 2009; Cordonnier et al., 2012). The effect of crystals on viscosity depends on their quantity and their shape and can be estimated using analytical and empirical models (e.g. Ryerson et al., 1988; Pinkerton and Stevenson, 1992; Lejeune and Richet, 1995; Pinkerton and Norton, 1995; Saar et al., 2001; Sato, 2005; Dingwell, 2006; Ishibashi and Sato, 2007; Caricchi et al., 2007; Costa, 2005; Costa et al., 2009; Petford, 2009; Ishibashi, 2009; Mueller et al., 2010; Castruccio et al., 2010; Vona et al., 2011; Cimarelli et al., 2011). The viscosity of flowing basaltic lava thus increases during emplacement as the lava cools and depend on the crystallisation sequence (e.g. Shaw, 1969; Marsh, 1981; Pinkerton and Stevenson, 1992; Crisp et al., 1994; Villeneuve et al., 2008).

The method used in planetary science to estimate the viscosity of lava flow from morphology assuming simple flow laws is therefore questionable. The eruption dynamics as well as the final morphology of lava flows is dependent on a complex viscous path of the cooling lava and the viscosity of Martian melts has never been experimentally measured. Robust experimental description of the physico-chemical processes of Martian iron-rich basalts, together with the modeling of the viscosity evolution as a function of cooling and crystallization is required to interpret correctly the morphology of Martian lava flow.

1.4 Main tools and goals of this study

The aim of my PhD project is to experimentally explore the rheological properties of Martian magmas, both above and below the liquidus and to correlate it with the morphology of lava flows in order to better understand magma dynamics and volcanic evolution throughout the entire history of Mars.

The following key questions have been identified and will be answered here: Does iron

have a significant effect on viscosity of silicate melts? What is the viscosity of Martian basaltic melts? How well are we able to interpret morphological observations in terms of lava rheology and hence composition? Are the viscosities derived from morphology coherent with the chemical compositions and mineralogy we know from Martian rocks? Does the diversity of Martian basalt compositions (including the variations over time) have a significant effect on viscosity and hence on the volcanic activity and can it be observed from lava flow morphology?

This research is multidisciplinary in essence and involves experimental, fieldwork and modeling approaches. The experimental part consists in measuring the viscosity molten or partially molten state lavas. Silicate melts were synthesized by mixing reagent powders in order to get the desired chemical composition. Their viscosity was measured via the concentric cylinder method, in air and controlled oxygen fugacity. The melts were quenched to get glasses being further chemically analyzed. These resulting glasses were also used to measure the viscosity near the glass transition using the differential scanning calorimeter. Details on the experimental procedure are given in the Annex A. Fieldwork was conducted on a basaltic lava flow in the Western Volcanic Zone, Iceland, to investigate the morphology and texture of flow (ground proof), and to collect samples, that were further analyzed in the lab. This fieldwork was completed by collaboration with the DLR and FU, that provided aerial images and elevation model of the lava flow acquired by a high resolution scanning camera. Modeling was used to evaluate the increase of magma viscosity as a function of its crystallization sequence. The modeling takes into account the composition of the interstitial melt as well as the shape and content of the crystals at a given temperature, pressure and oxygen fugacity. We use the most recent empirical models to evaluate the effect of crystals on the viscosity in combination with thermodynamic calculation (using MELTS) to simulate crystallization sequence.

Each chapter and part of the introduction are based on articles that have been submitted to scientific international journals, namely:

Chevrel M.O., Giordano D., Potuzak M., Courtial P. and Dingwell D.B. (2012), Physical properties of $\text{CaAl}_2\text{Si}_2\text{O}_8$ - $\text{CaMgSi}_2\text{O}_6$ - FeO - Fe_2O_3 melts: Analogues for extraterrestrial basalt. *Chemical Geology*, Vol. 346, Pages 95-105, 2013;

Chevrel M.O., Platz T., Hauber E., Baratoux D., Lavallée Y. and Dingwell D.B. Planetary lava flow rheology: a comparison of morphological and rheological methods. Submitted in Oct. 2012 to *Earth and Planetary Science Letters*, in review;

Chevrel M.O., Baratoux D., Hess K-U. and Dingwell D.B. Viscous flow behavior of tholeiitic and alkaline Fe-rich Martian Basalts. Submitted in Feb. 2013 to *Geochimica Cosmochimica Acta*, in review.

CHAPTER 2

Effect of iron on viscosity: case study of the physical properties of $\text{CaAl}_2\text{Si}_2\text{O}_8$ - $\text{CaMgSi}_2\text{O}_6$ - FeO - Fe_2O_3 melts: analogues for extra-terrestrial basalt

Abstract

The effects of increasing quantities of iron on the viscosity and glass transition temperature of a haplobasaltic base composition (anorthite–diopside eutectic) have been determined. The viscosity was measured at 1 atm at superliquidus regime and near the glass transition temperature using the concentric cylinder and the micropenetration method (for the melts that could be quenched to glasses), respectively. The effect of iron oxidation state on viscosity was investigated above the liquidus under reduced fO_2 and at the glass transition temperature from quenched samples of varying redox state. Results show that iron significantly decreases the melt viscosity and lowers the activation energy, especially near the glass transition temperature. The reduction of iron from Fe^{3+} to Fe^{2+} produces a slight viscosity decrease at high temperature but affects properties near the glass transition more strongly. Thus, for iron-rich compositions, the redox state must be taken into account to obtain accurate estimates of the physical and thermodynamic properties. Here we also show that the iron-bearing anorthite–diopside system approaches the viscous behavior of terrestrial and extra-terrestrial basaltic compositions and then appears to be good analogue for basaltic systems. It is then suggested that at temperature of eruption, the viscosity of iron-rich lunar or Martian -like basalt is expected to be 0.5 to 1 order of magnitude lower than common terrestrial basalt.

2.1 Introduction

The physico-chemical processes behind magmatic and volcanic phenomena (including partial melting, crystallization, degassing, fragmentation and explosive eruption) are governed by transport dynamics and by magma properties, which determine the extent and efficiency of energy, momentum and mass exchange between phases in multiphase magmatic mixtures (e.g., Dingwell, 1996; Papale, 1999; Sparks, 2003). The viscoelasticity (e.g., viscosity and elastic moduli), together with the density, control the fluid dynamics of transport and the buoyancy forces, respectively. The thermodynamic properties (enthalpy, entropy, and volume) and their P–T derivatives (specific heat capacity, compressibility, and thermal expansivity) provide information about the energy budget of the magmatic mixtures and define the thermodynamic state of the system (e.g., Richet, 1987a). To identify and quantify the physical mechanisms dominating magmatic and volcanic processes, and their impact on the environment, a robust comprehensive experimental description of the physico-chemical properties, together with the application of modeling, is required to evaluate and forecast the evolution of such processes. To date, despite a considerable number of experimental studies (e.g., Mysen et al., 1984; Richet and Bottinga, 1995; Lange and Carmichael, 1987; Dingwell and Brearley, 1988; Dingwell and Virgo, 1987, 1988; Toplis et al., 1994; Solvang et al., 2004; Magnien et al., 2004; Webb, 2005; Richet, 2009) and modeling (Russell et al., 2002, 2003; Giordano and Dingwell, 2003; Hui and Zhang, 2007; Giordano et al., 2008; Kondratiev et al., 2008), the chemical and structural role of iron in silicate melts still remains incomplete (Wilke, 2005). The situation is especially critical for iron-rich volcanic products, which are particularly experimentally challenging.

In both melts and crystals, iron may be found in a variety of coordination environments ranging from tetrahedral ($^{\text{IV}}\text{Fe}$), to pentahedral ($^{\text{V}}\text{Fe}$), and to octahedral ($^{\text{VI}}\text{Fe}$) (Mysen et al., 1984; Giuli et al., 2003; Wilke et al., 2007) and it can occur either as a reduced, ferrous (Fe^{2+}) or oxidized, ferric (Fe^{3+}) component. The oxidation state of iron (i.e., $\text{Fe}^{2+}/\text{Fe}_{\text{tot}}$ hereafter) describes the redox state of the magma (Carmichael, 1991; Christie et al., 1986; Herd, 2008) and represents a first-order influence on the crystallization sequence of phases and on resultant degassing (Brooks et al., 1991; Toplis and Carroll, 1995; Lattard and Partzsch, 2001; Moretti and Papale, 2004). Iron is the most abundant transition metal present in the rocky planets and a major element in basaltic melts that volumetrically dominate (~ 95 vol. %) products erupted at the Earth’s surface and presumably those of other rocky planets (e.g., for Mars Boynton et al., 2007; Baratoux et al., 2011). On Earth, the iron content of magma commonly ranges between 3 and 12 wt. % FeO_{tot} (Manson, 1967). Remarkable iron-rich compositions (12–16 wt. % FeO_{tot}) do exist but are rare, typically associated with ultrabasic lavas (ferropicrite)

in large igneous provinces (e.g. Parana-Etendeka, Siberia) (Francis et al., 1999; Gibson et al., 2000); or exhibited by low-silica effusive rocks such as ultramafic Komatiitic lavas (Arndt et al., 1977); or found in hot spot related volcanic provinces, e.g., Hawaii, Galapagos, Craters of the Moon lava field, Iceland (Fisk et al., 1982; Stout et al., 1994; Norman and Garcia, 1999; Eason and Sinton, 2009). Extremely high iron contents (up to 22 wt. % FeO_{tot}) have been inferred for the majority of volcanic products of both Mars and the Moon (Binder, 1976; Gellert et al., 2004; Boynton et al., 2007; McSween et al., 2009). The composition and the morphology of both terrestrial ultrabasic flows and Martian and lunar volcanic landforms suggest fast eruption rates, high eruption temperatures and very low viscosity magmas (e.g., Huppert and Sparks, 1985; Cas et al., 1999; Baratoux et al., 2009; Hauber et al., 2009; Vaucher et al., 2009a).

This study combines viscometric and calorimetric measurements to address the rheological description of iron-rich melts like extra-terrestrial lunar and Martian volcanic products. Anorthite-Diopside ($\text{CaAl}_2\text{Si}_2\text{O}_8$ - $\text{CaMgSi}_2\text{O}_6$) eutectic composition was selected to serve as analogue to basalt, to which amounts of iron (5, 10, 20, 30 wt. % Fe_2O_3) were added. This composition was chosen because its physico-chemical properties are well characterized and it has long been considered a suitable analogue for basaltic composition (Scarfe et al., 1983) with only minor restrictions (Giordano et al., 2008).

2.2 Experimental methods

2.2.1 Starting material

Five batches of synthetic melts having Anorthite-Diopside eutectic composition ($\text{An}_{42}\text{Di}_{58}$: AD) were synthesized from oxides and carbonate powders, previously dried at 120 °C for 24 hours. Each batch was fused in a platinum crucible for two hours at 1873 K. The melts were poured onto a stainless steel plate for cooling and the resulting glasses were finely ground. Pure iron oxide powder was added to the individual batches to provide samples containing 5, 10, 20 and 30 wt. % Fe_2O_3 , named AD-5, AD-10, AD-20 and AD-30, respectively. The mixtures were melted for 3 hours at 1873 K in platinum crucibles that were previously doped with iron to minimize the iron loss to the crucible wall. In order to eliminate bubbles and promote homogenization, each melt was stirred for 24 hours using a rotational viscometer. Sample compositions of the homogenized samples are presented in Table 2.1.

Sample	AD		AD-5		AD-10		AD-20		AD-30	
	wt. %	mol. %	wt. %	mol. %	wt. %	mol. %	wt. %	mol. %	wt. %	mol. %
SiO ₂	49.23 (0.47)	50.12	47.39 (0.26)	49.24	45.64(0.21)	48.82	40.42 (0.19)	46.48	35.87 (0.62)	44.10
Al ₂ O ₃	14.96 (0.07)	8.98	14.22 (0.11)	8.71	13.52 (0.1)	8.53	11.93 (0.1)	8.08	10.35 (0.11)	7.50
Fe ₂ O ₃ ^a	0.00	0.00	5.06 (0.16)	1.98	9.03 (0.09)	3.64	20.20 (0.17)	8.74	29.93 (0.82)	13.84
MgO	10.01 (0.1)	15.20	9.76 (0.08)	15.12	9.24 (0.06)	14.74	8.12 (0.06)	13.92	6.3 (0.12)	11.54
CaO	23.57 (0.2)	25.71	22.41 (0.17)	24.95	21.18 (0.14)	24.28	18.49 (0.12)	22.78	17.47 (0.45)	23.02
Total	97.77	100	98.84	100	98.61	100	99.17	100	99.92	100

Table 2.1: Chemical compositions of the iron-free and iron-bearing anorthite-diopside melts in wt. % (average of 5 to 10 electron microprobe analyses for each sample) and normalized mol. %.

Numbers in brackets are the associated standard deviation

^a Total iron as Fe₂O₃

2.2.2 High-temperature viscometry in air

High-temperature viscosity of the dry liquid samples was determined via the concentric cylinder method (Dingwell, 1986) by decreasing the temperature in 25 K increments. The apparatus consists of a Deltech furnace heated by MoSi₂ elements and a Brookfield rheometer model RVTD (Rotary Variable Transducer Displacement) with a full range torque of 7.2×10^{-4} N.m. Instrument drift was checked by reacquisition of the highest temperature data-point at the end. The precision on the viscosity for this apparatus was derived from replication of viscosity determination of standard melt NBS SRM 711 standard lead-silica glass and is estimated at $\pm 3\%$ at the 2σ (Dingwell, 1986). The temperature calibration was determined by the immersion of a S-type (Pt/Pt₉₀-Rh₁₀) or B-Type (Pt/Pt₃₀-Rh₆) thermocouple into the melt over a large range of temperatures. After measurements, the melts were poured onto a stainless steel plate to quench large samples used for micropenetration experiments. For AD-20 and AD-30, those large samples showed extensive crystallization, preventing for further analysis.

2.2.3 High-temperature viscometry and loop fusion experiment under reduced conditions

The role of iron oxidation state on viscosity at high temperature was investigated for the iron-rich melts AD-10 and AD-20. The measurements were acquired with the same concentric cylinder technique, but using a vertical alumina muffle tube furnace equipped with a CO₂-CO gas-mixing line. The top of the furnace was fitted with an iris diaphragm to allow the spindle to pass through (Dingwell and Virgo, 1987). At isothermal conditions, the melt was initially equilibrated in air and then reduced using mixed CO₂-CO gas flows within the muffle tube. The oxygen fugacity (fO_2) was monitored with a differential voltmeter linked to a yttria-stabilized zirconia oxygen sensor placed just below

the crucible. Several oxidation states were achieved by changing the $\text{CO}_2:\text{CO}$ ratio. At each reduction step at least 24 hours was required to permit melt equilibration (i.e., time invariant viscosity record). After the last step (i.e. the most reduced condition) the gas flow was shut off and the melt oxidized to reacquire the initial condition in equilibrium with air. Sampling was performed after each equilibration at the new $f\text{O}_2$ by “dip quench technique”. This technique consists of inserting an alumina-oxide rod into the melt which is then withdrawn and plunged into distilled water to ensure a rapid quench. Although the action was performed as quickly as possible, some melts may have undergone some oxidation during the process. The effect of iron oxidation state on viscosity was not measured for AD-5 at high temperature; instead samples were reduced via loop fusion experiments under controlled $f\text{O}_2$. Approximately 30 mg of glass sample were suspended on a platinum wire loop within a similar vertical alumina muffle tube furnace tightly capped and equipped with a $\text{CO}_2\text{-CO}$ gas-mixing facility. After 24 hours at isothermal condition, when the sample reaches equilibrium with the surrounding atmosphere, the platinum wire was severed, dropping the sample into distilled water to quench. The temperature and $f\text{O}_2$ were monitored continuously using a S-type thermocouple and a yttria-stabilized zirconia oxygen sensor placed together close to the sample.

Glass chips resulting from these experiments were mounted as polished sections for petrographic and chemical analysis carried out with a CAMECA SX 100 Electron Micro-Probe Analyser (EMPA) at the University of Munich using an accelerating voltage of 15 kV and a beam current of 20 nA with counting time of 5 s for the background and 10 s for the elements. The standards used were Wallastonite for Si and Ca, Albite for Al, Hematite for Fe and Periclase for Mg. The data were corrected according to the PAP procedure (Pouchou and Pichoir, 1985). Samples were also used for determination of $\text{Fe}^{2+}/\text{Fe}_{\text{tot}}$ ratio by potassium dichromate titration and to accomplish calorimetric measurements (see detailed methods in Annex 1).

2.2.4 Low temperature viscometry

The low-temperature viscosities were measured using a micropenetration technique. The measurements were accomplished near the glass transition in the range of $10^{8.6}$ to $10^{11.5}$ Pa·s using a vertical pushrod Bähr 802 V dilatometer (Hess et al., 1995, and reference within). The present assembly uses hemispherical Ir indenters with a force of 1.2 N and the indentation depths were up to 150 to 200 μm . Although this technique required small amount of material, the samples need to have polished parallel faces. Therefore only samples quenched from pouring melt (equilibrated in air) could be measured. Each measurement was carried out on a different sample and under isothermal conditions (15 min after the target temperature was reached) to insure a fully relaxed state. Analyses were

conducted under a sustained Argon atmosphere to avoid further oxidation. Measurements that showed evidence of oxidation or crystallization were not used.

2.2.5 Differential scanning calorimetry (DSC) methodology

The glass transition temperature was estimated from calorimetric measurements (Moynihan et al., 1974; Scherer, 1984) using a Differential Scanning Calorimeter (DSC 404 Pegasus from NETZSCH® Gerätebau). The samples used here were small glass chips (<50 mg) that resulted from the “dip quench” technique or loop fusion experiments. After initial heating into the liquid field (i.e., approximately 50 K above the glass transition temperature), the sample were exposed to four cycles of cooling and subsequent heating at fixed rate of 20, 15, 10 and 5 K/min.

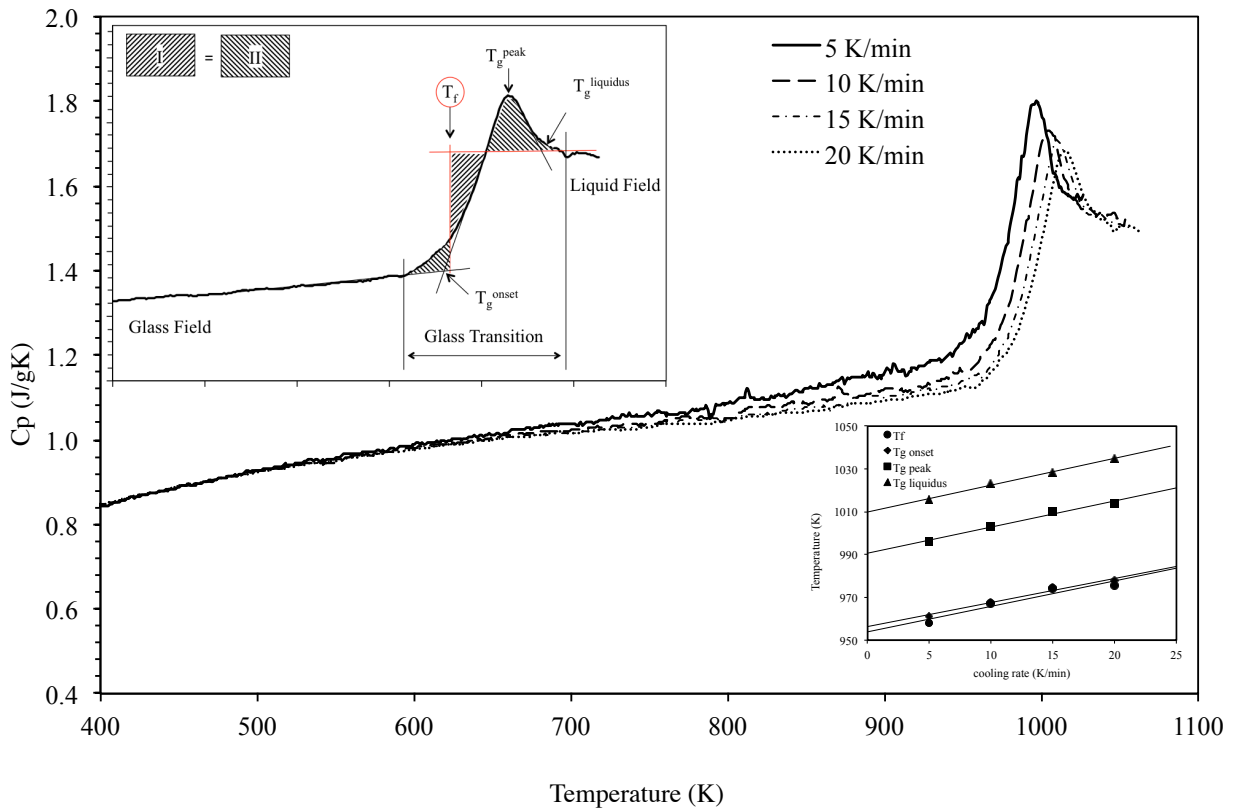


Figure 2.1: Example of heat capacity (C_p) curves for AD-10 at various cooling]The left high inset shows the method to collect the T_f and T_g values at the onset, peak and liquid position. The bottom right inset is the variation of the different temperatures values as a function of cooling rate.

For each sample and each rate, individual heat capacity (C_p) curves were measured against a sapphire of the equivalent mass. The time spent above the glass transition was minimized to reduce the occurrence of crystallization or oxidation. The reproducibility of the C_p curves obtained is a clear indication that no significant degradation of the samples

occurred. From the C_p curves, the limiting fictive temperature (T_f') describing at which temperature the liquid structure is frozen in, was determined according to the method of Moynihan (1995) (Fig. 2.1).

In order to compare the peak shape of all runs, temperature were also collected at the onset of the peak (T_g^{onset}), at the maximum value of the peak (T_g^{peak}) and at the onset of the stable liquid heat capacity (T_g^{liquid}) (Fig. 2.1). The reproducibility of the run and instrument deviation lead to a temperature deviation of ± 4 °C.

2.2.6 Samples redox state

The oxidation state of each investigated glasses was determined by potassium dichromate titration, a wet-chemistry method based on a simple potentiometric titration Giuli et al. (2011). The $\text{Fe}_{2+}/\text{Fe}_{\text{tot}}$ values for the set of AD-10 samples reduced under controlled atmosphere are reported in Figure 2.2 as a function of $f\text{O}_2$ and compared with the model of Kress and Carmichael (1991) and Moretti (2005). We note that the $\text{Fe}^{2+}/\text{Fe}_{\text{tot}}$ values for melts that were quenched from low $f\text{O}_2$ are too “oxidized” relative to the models. In contrast, the agreement is very reasonable for sample quenched from melts equilibrated in air. Samples quenched from lower $f\text{O}_2$ could be affected by oxidation during the quenching process and during the digestion of the sample in solution.

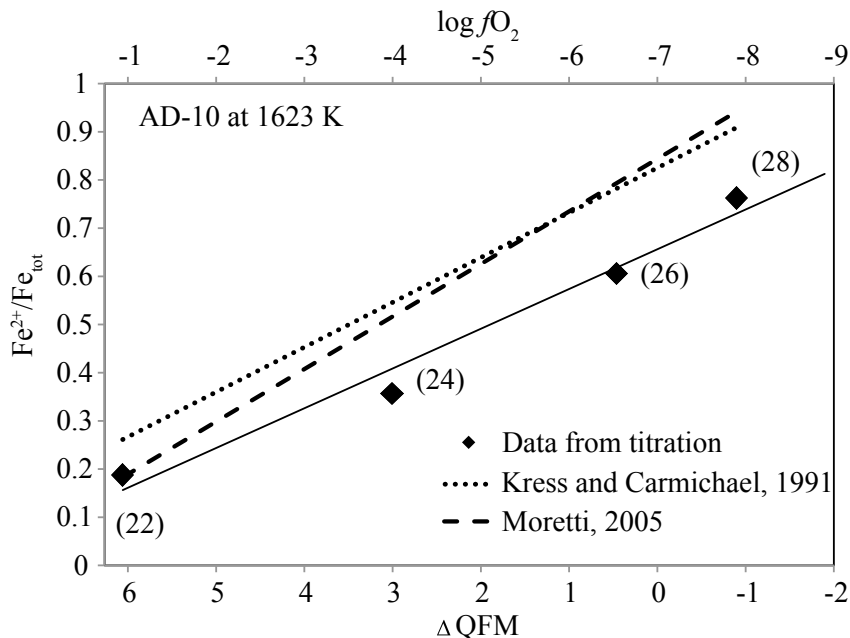


Figure 2.2: Iron redox state of the set of AD-10 melts obtained by potassium dichromate titration as a function of ambient oxygen fugacity. The full line is the linear trend of the data, the dotted line represents the estimation according to the model of Kress and Carmichael (1991) and the dashed line according to the model of Moretti (2005).

2.3 Results

2.3.1 High temperature viscosity

The high-temperature viscosities measured in air, respectively with the concentric cylinder are presented in Figure 2.3 and reported in Table 2.2. Liquidus temperatures for the samples AD-10, AD-20 and AD-30 were indirectly observed to be as high as 1498 K, 1572 K and 1670 K, respectively; below those temperatures clear onsets of crystallization were inferred from sudden increase of the measured viscosity.

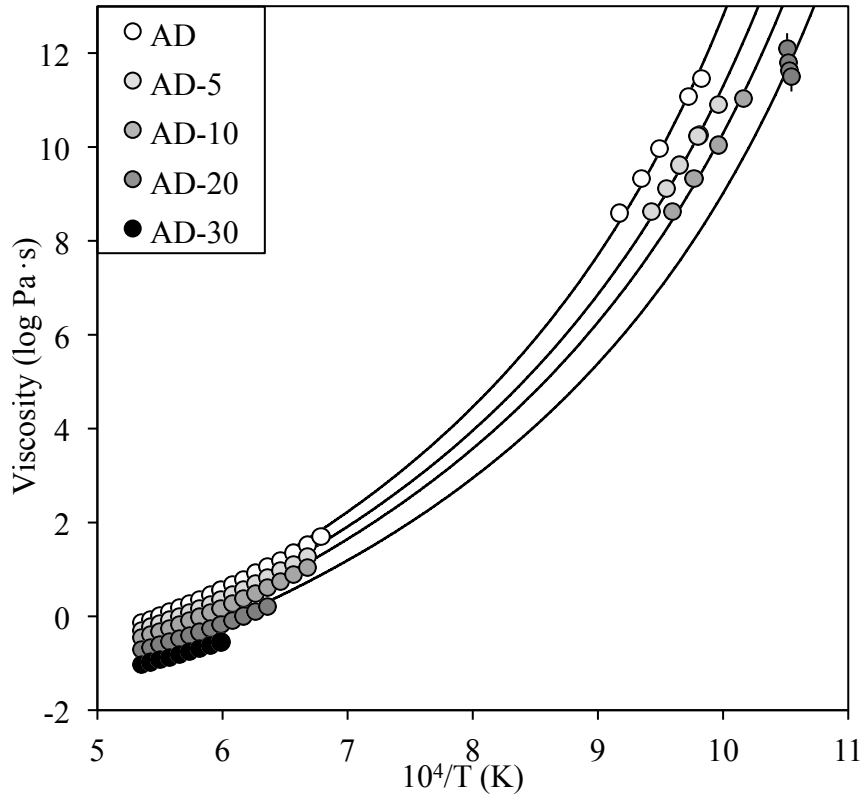


Figure 2.3: Temperature dependence of viscosity measured in air using the concentric cylinder and micro-penetration methods. The low temperature viscosities for AD-20 were obtained using viscosity estimation at T_f' using Eq. 2.2. The viscosity of AD-30 at low temperature could not be obtained. The bold lines are the TVF fit calculated from Eq. (2.3).

Regardless of the redox state, the isothermal viscosity variations show that the addition of 20 wt. % iron (8.7 mol. % Fe_2O_3) causes a decrease of one log unit at 1470 K (Fig. 2.4). The data were first fitted within the same temperature interval (1867 to 1670 K) using an Arrhenian relationship:

$$\ln \eta = A_A + \frac{\Delta H_\eta}{RT} \quad (2.1)$$

where η is the viscosity, A_A a pre-exponential term, ΔH_η , the enthalpy variation equivalent to activation energy of viscous flow, R the ideal gas constant and T the temperature. Although the Arrhenian relationship is invalid over a large temperature range (e.g. Richet and Bottinga, 1995; Hess et al., 1995; Whittington et al., 2001; Russell et al., 2002, 2003) this approximation is suitable for data comparison over limited temperature or viscosity ranges. The terms of Eq. 2.1 are presented in Table 2.3 together with their Root Mean Square Error (hereafter RMSE).

T (K)	$\log \eta$ (Pa s)	AD	AD-5	AD-10	AD-20	AD-30
1867		-0.14	-0.30	-0.45	-0.71	-1.03
1842		-0.06	-0.22	-0.39	-0.66	-0.98
1818		0.02	-0.15	-0.32	-0.60	-0.93
1793		0.10	-0.08	-0.25	-0.54	-0.87
1769		0.18	0.00	-0.18	-0.48	-0.82
1744		0.27	0.08	-0.10	-0.41	-0.75
1719		0.36	0.16	-0.01	-0.34	-0.69
1695		0.45	0.25	0.07	-0.26	-0.62
1670		0.56	0.35	0.17	-0.18	-0.55
1646		0.67	0.46	0.27	-0.09	-
1621		0.79	0.57	0.38	0.01	-
1596		0.92	0.69	0.49	0.11	-
1572		1.06	0.83	0.61	0.21	-
1547		1.18	0.97	0.74	-	-
1523		1.35	1.10	0.88	-	-
1498		1.52	1.27	1.04	-	-
1473		1.70	-	-	-	-
1090		8.59	-	-	-	-
1070		9.34	-	-	-	-
1054		9.97	-	-	-	-
1029		11.07	-	-	-	-
1018		11.46	-	-	-	-
1061		-	8.63	-	-	-
1048		-	9.12	-	-	-
1036		-	9.62	-	-	-
1020		-	10.23	-	-	-
1019		-	10.25	-	-	-
1004		-	10.90	-	-	-
1042		-	-	8.63	-	-
1024		-	-	9.33	-	-
1003		-	-	10.04	-	-
984		-	-	11.03	-	-
951		-	-	-	12.11 ^a	-
950		-	-	-	11.81 ^a	-
949		-	-	-	11.64 ^a	-
948		-	-	-	11.51 ^a	-

Table 2.2: High- and low- temperature viscosities measured in air, respectively with the concentric cylinder and micro-penetration.

^a Viscosity calculated at T_f' for AD-20, see results part 2.3.3

Figure 2.5 shows the linear decrease of the high-temperature from 210 kJ/mol for the iron-free AD sample to 145 kJ/mol for the iron-rich AD-30 sample (equivalent to 31 %

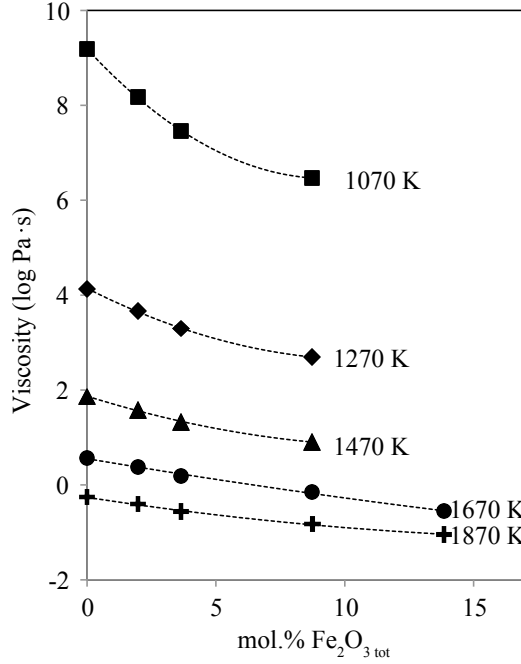


Figure 2.4: Isothermal viscosity variation as a function of the bulk molar fraction of iron expressed as Fe_2O_3 .

	A_{AHT}	$\Delta H_{\eta\text{H}}$	RMSE ^a	A_{ALT}	$\Delta H_{\eta\text{LT}}$	RMSE ^a	A_{TVF}	B_{TVF}	C_{TVF}	RMSE ^a	m^b	SM ^c	NBO/T
	(kJ/mol)			(kJ/mol)			(log Pa s)	(log Pa s / K)	(K)				
AD	-13.87	210	0.041	-76.20	869	0.078	-4.129	4362	742	0.117	60.40	40.91	0.94
AD-5 (42)	-12.45	183	0.041	-71.90	810	0.062	-4.099	4227	725	0.088	60.58	40.63	0.87
AD-10 (22)	-13.08	183	0.034	-71.62	792	0.270	-4.146	4147	713	0.092	60.95	40.18	0.81
AD-20 (S1)	-12.18	163	0.017	-94.90	962	0.169	-4.125	3829	709	0.167	64.24	39.51	0.66
AD-30	-11.73	145	0.006	-	-	-	-	-	-	-	-	-	-
AD-5 (39)*	-	-	-	-86.83	936	0.177	-4.125	4318	718	0.162	59.37	42.34	0.99
AD-10 (28)*	-	-	-	-80.76	863	0.119	-4.125	4419	686	0.175	56.48	43.44	1.05
AD-20 (S2)*	-	-	-	-93.87	935	0.112	-4.125	3788	692	0.073	63.65	41.42	0.80
AD-20 (S3)*	-	-	-	-92.84	921	0.190	-4.125	3791	687	0.084	63.22	43.41	0.94
AD-20 (S4)*	-	-	-	-91.21	909	0.170	-4.125	3839	684	0.153	62.43	45.46	1.09

Table 2.3: Enthalpy variation calculated at high temperature ($\Delta H_{\eta\text{HT}}$) and at low temperature ($\Delta H_{\eta\text{LT}}$) from Eq. 2.1, TVF fitting parameters calculated from Eq. 2.3 and fragility index is calculated from Plazek and Ngai (1991) at $T_g = T_{\log \eta=12}$.

*Sample equilibrated under reduced conditions, $\Delta H_{\eta\text{LT}}$ is calculated between $\eta = 10^{8.5}$ and 10^{11} Pa·s from Eq. 2.3

^aRoot Mean Square Error

^bFragility index

^cCalculated considering Fe^{3+} to be network former and Fe^{2+} to be modifier

decrease).

The results of the superliquidus viscosity measurements under varying controlled oxygen fugacity, together with the corresponding melt redox states are reported in Table 2.4. The maximum decrease of viscosity due to iron reduction is dependent on the total iron concentration. For the AD-10 and AD-20 melts the increasing amount of Fe_{2+} lowers the viscosity by 0.03 log Pa·s and 0.12 log Pa·s, respectively.

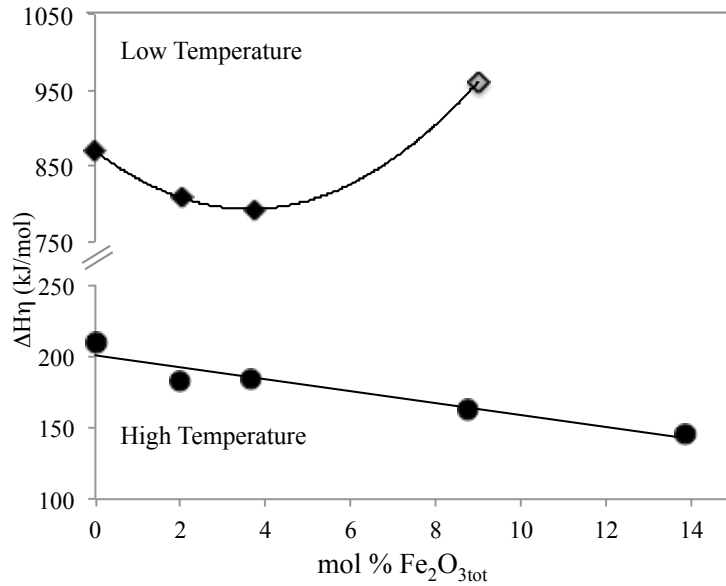


Figure 2.5: Enthalpy variation ($\Delta H_{\eta}LT$) calculated from Eq. 2.1 in the high and low temperature interval as a function of the bulk molar fraction of iron expressed as Fe_2O_3 . The $\Delta H_{\eta}LT$ for AD-20 (grey diamond) was calculated from Eq.2.3.

	Sample n°	$\log f_{\text{O}_2}$	$\text{Fe}^{2+}/\Sigma\text{Fe}$	$\log \eta$ (Pa s)
AD-10	#22	-0.705	0.18 (0)	0.56
	#24	-3.758	0.32 (0.05)	0.54
	#26	-6.301	0.50 (0)	0.53
	#28	-7.660	0.73 (0.04)	0.53
	#31	-8.763	0.74 (0.03)	0.54
	#32	-0.674	0.17(0)	0.56
AD-20	#S1	-0.737	0.18 (0)	-0.121
	#S2	-3.139	0.36 (0)	-0.198
	#S3	-7.024	0.52(0.01)	-0.232
	#S4	-9.240	0.67(0.02)	-0.236

Table 2.4: Isothermal viscosity measurements obtained under controlled f_{O_2} for AD-10 at 1623 K and AD-20 at 1658 K. In brackets are the standard deviation of titration measurements calculated from two samples under the same conditions. Sample n° 32 has been collected at the end of the melt reduction steps, once the melt is back in equilibrium with air

2.3.2 Low temperature viscosity

The low-temperature viscosities measured by micropenetration are presented in Figure 2.3 and reported in Table 2.2. The low-temperature viscosities presented here for sample AD-20 were inferred from the calorimetric glass transition temperature (see section 2.3.3). For sample AD-30, neither micropenetration nor calorimetric measurements on a pure glass sample could be obtained because of widespread crystallization during quenching.

The addition of 20 wt. % of iron causes a viscosity drop of 3 orders of magnitude at 1070 K (Fig. 2.4). The data were fitted with Eq. 2.1 within the viscosity interval of the measurements ($10^{8.6}$ to $10^{11.5}$ Pa·s). For AD-20, $\Delta H_\eta LT$ was estimated within the same range from the non-Arrhenian fit obtained in section 3.4. As iron is added to the base composition, the enthalpy variation decreases non-linearly between iron-free AD and AD-10 (Fig. 2.5); the addition of 5 wt. % of iron to the iron-free composition causes a decrease of 47 kJ/mol, and additional 5 wt. % induces a lesser decrease of 18 kJ/mole. An addition of further 10 wt. % yields a large increase in the enthalpy variation; the $\Delta H_\eta LT$ for AD-20-S1 is estimated to be 962 kJ/mol.

2.3.3 The calorimetric glass transition temperatures and derived viscosity

The temperatures measured at the calorimetric glass transition include the limiting fictive temperature (T_f') and temperatures collected at the onset (T_g^{onset}) and at the maximum (T_g^{peak}) of the peak and at the onset of the liquid field (T_g^{liquid}) are listed in Table 2.5 for each melts (oxidized and reduced). The T_g^{liquid} of the AD-20 sample equilibrated in air (AD-20-S1) could not be obtained because of the occurrence of crystallization after crossing of the glass transition, which prevented reproducible measurements on the same sample.

Sample n°	Fe ²⁺ /Fe _{tot}	T _f ' (K)				T _g ^{onset} (K)				T _g ^{peak} (K)				T _g ^{liquid} (K)			
		q (K/min)				q (K/min)				q (K/min)				q (K/min)			
		5	10	15	20	5	10	15	20	5	10	15	20	5	10	15	20
AD	-	1001	1006	1012	1018	1001	1011	1013	1014	1034	1042	1048	1053	1049	1059	1067	1072
AD-5	#42 0.17	978	985	990	1001	982	990	989	1002	1015	1024	1028	1039	1031	1042	1049	1059
	#41 0.32	974	983	987	993	981	983	991	994	1012	1021	1026	1030	1029	1038	1048	1053
	#40 0.70	974	983	989	991	981	983	989	993	1012	1019	1026	1029	1029	1038	1045	1052
	#39 0.71	981	989	994	998	982	991	997	1000	1015	1024	1030	1033	1031	1040	1049	1053
AD-10	#22 0.18 (0)	958	967	974	976	961	968	975	978	996	1003	1010	1014	1016	1023	1028	1035
	#24 0.32 (0.05)	956	963	968	973	961	968	971	974	994	1001	1006	1012	1010	1019	1030	1033
	#26 0.50 (0)	950	958	965	968	953	962	965	970	989	997	1003	1006	1005	1015	1020	1027
	#31 0.74 (0.03)	956	961	969	972	961	966	971	973	989	998	1003	1010	1008	1019	1023	1029
	#28 0.73 (0.04)	950	962	965	971	958	961	969	968	988	997	1003	1006	1006	1014	1021	1025
AD-20	#S1 0.18 (0)	951*	950*	949*	948*	952	951	950	949	983	981	982	980	997	995	998	995
	#S2 0.36 (0)	926	930	932	936	926	933	932	937	960	963	966	970	983	981	984	990
	#S3 0.52(0.01)	920	924	929	930	917	924	925	930	952	958	966	966	969	981	987	992
	#S4 0.67(0.02)	918	924	928	932	917	921	926	928	944	954	961	965	1010	1010	1020	1015

* calculated from the linear relationship: $T_f' = 0.964 T_g^{\text{onset}} + 32.83$; $R^2 = 0.981$

Table 2.5: Limiting fictive temperatures and glass transition temperatures collected at the onset, peak and liquid position of the Cp curves for all oxidized and reduced samples at 5, 10, 15 and 20 K/min cooling/heating rate.

For this sample, T_f' was calculated from its linear correlation with T_g^{onset} obtained from the other measurements ($T_f' = 0.964 T_g^{\text{onset}} + 32.83$; $R^2 = 0.981$). In contrast, the reduced samples ($\text{Fe}^{2+}/\text{Fe}_{\text{tot}} > 0.3$) are more “stable”, with no crystallization taking place immediately above the glass transition; the liquid field could be reached and the

measurements were reproducible. The shift of the glass transition temperatures towards lower values as a function of iron content is non-linear as shows in Fig. 2.6a. For the most oxidized samples the addition of 10 wt. % of iron to the base composition decreases T_f' by 40 K while an additional 10 wt. % of iron decreases T_f' by only an additional 20 K. For the reduced samples T_f' is shifted to lower values and the glass transition temperature dependence on iron content become more linear. The effect of redox state on T_f' is dependent on the iron content (Fig. 2.6b), logically; the more iron the more the redox state affects T_f' . The increase of $\text{Fe}^{2+}/\text{Fe}_{\text{tot}}$ from 0.16 to 0.50 leads to a decrease of T_f' by 30 K in AD-20; 10 K in AD-10; and no decrease in AD-5. Upon further iron reduction ($\text{Fe}^{2+}/\text{Fe}_{\text{tot}} > 0.5$) T_f' remains constant. Therefore, a minimum T_f' value is reached at approximately 50 % iron reduction.

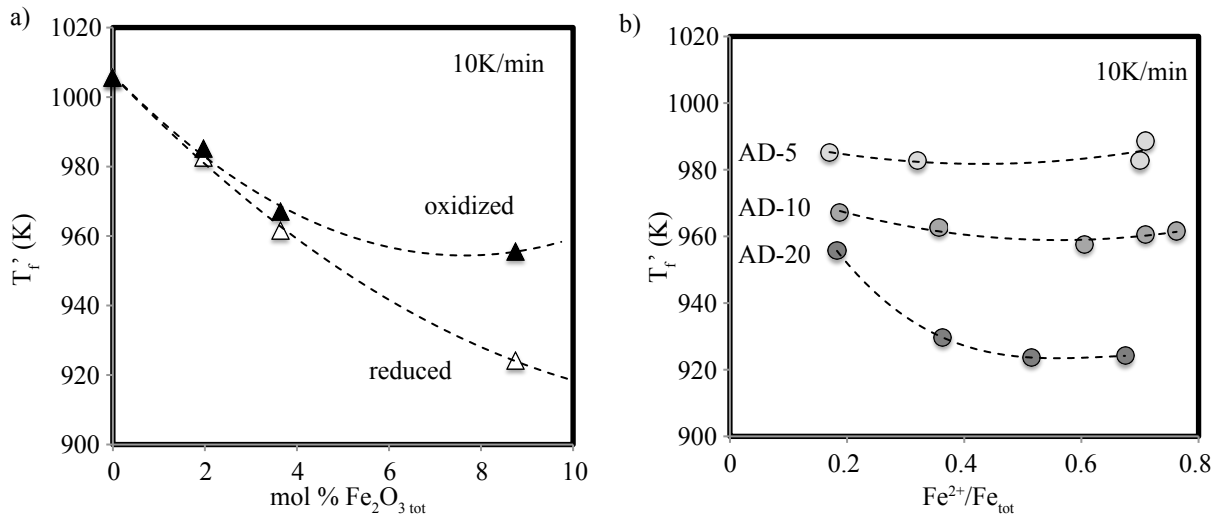


Figure 2.6: a) Variation of the glass transition taken at T_f' for cooling/heating rate of 10 K/min as a function of the bulk molar fraction of iron. Full symbols represent the values for the samples equilibrated in air (AD-5-42, AD-10-22 and AD-20-S1) and empty symbols for the most reduced samples (AD-5-40, AD-10-28, AD-20-S4). b) Variation of T_f' for cooling/heating rate of 10 K/min as a function of the redox state for all investigated melts. Dotted lines in (a) and (b) are intended as a guide for the eye.

The viscosity at T_f' is estimated considering that the enthalpic relaxation time is identical to that of viscous flow (e.g. Scherer, 1984; Dingwell and Webb, 1990) leading to an equivalence between the cooling rate and the viscosity at T_f' via:

$$\log \eta(at T_f') = K - \log |q| \quad (2.2)$$

where K is a constant, the so called shift factor and q is the cooling rate. K is calculated using Eq.2.1 from the samples that could be measured with the micropenetration

technique (AD, AD-5 and AD-10). Although K is sometimes considered independent of composition (Toplis et al., 2001; Sipp and Richet, 2002), other studies have evidenced a non-linear decrease of K with increasing excess oxides (e.g. Gottsmann et al., 2002). Here, K is found to be the same (10.88 ± 0.14) when calculated for AD-5 and AD-10 however it is 11.2 ± 0.09 when calculated for the iron-free AD composition. Apart from this slight difference, a systematic compositional dependence of K cannot be inferred. Therefore the viscosity at T_f' was calculated using an averaged K value of 11.04 ± 0.2 . The maximum error on the viscosity is then estimated at ± 0.2 log unit. At T_f' , iron reduction has a little effect on the viscosity of AD-5 and AD-10 but a larger influence on AD-20 (Fig. 2.7). In the case of AD-20 near the glass transition, the most reduced melt ($Fe^{2+}/Fe_{tot}=0.67$) has a viscosity of one order of magnitude lower than the melt equilibrated in air. Further melt reduction, above $Fe^{2+}/Fe_{tot} = 0.5$, does not affect T_g , and hence, not affect the viscosity.

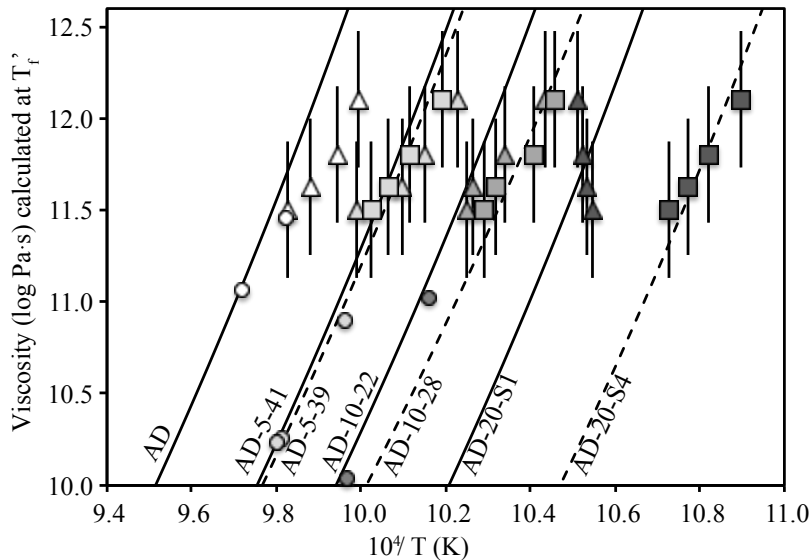


Figure 2.7: Viscosity calculated at T_f' using Eq.2.2 for the melts equilibrated in air (circles), and the most reduced samples (square). The errors bars are the maximum error of 0.3 log Pa·s. The full lines represent the TVF fit for the melts equilibrated in air and the dashed lines for the reduced samples. Data from micropenetration are also plotted as small circles.

2.3.4 Viscosity behavior over the entire temperature range

Looking at the temperature dependence of viscosity over the entire range of investigated temperatures, the data can be fitted using the Tammann-Vogel-Fulcher (TVF)

equation (Tammann and Hesse, 1926; Vogel, 1921; Fulcher, 1925):

$$\log\eta = A_{TVF} + \frac{B_{TVF}}{T - C_{TVF}} \quad (2.3)$$

where A_{TVF} represents a lower limit of silicate melt viscosity at high temperature; B_{TVF} , the pseudo-activation energy; and C_{TVF} represents the temperature at which viscosity would become infinite. The employment of this equation is justified by comparison purposes as most of experimental rheological studies of melts relevant to geological studies use this equation. The parameter A_{TVF} is considered as a constant for all silicate melts according to several numerical and theoretical studies (Myuller, 1955; Eyring et al., 1982; Angell, 1985). Because of model optimization issues, Russell et al. (2003); Giordano et al. (2008, 2009) determined that A_{TVF} is approximated to a value of $-4.55 \pm 0.21 \log \text{Pa}\cdot\text{s}$ for natural and synthetic analogues Arrhenian to non-Arrhenian silicate liquids. Here, A_{TVF} was estimated from AD, AD-5 and AD-10 to be -4.125 ± 0.4 and input in Eq.2.3 to estimate B_{TVF} and C_{TVF} . The fitting parameters, together with the associated uncertainty of the fit are reported in Table 2.3. The fragility of a melt is commonly used to track departures of viscosity from Arrhenian behavior and to distinguish strong Arrhenian-like (low fragility values) and fragile non-Arrhenian (high fragility values) melts. The fragility index is calculated in terms of the steepness index (m) (Plazek and Ngai, 1991) at $T_g = T_{\log \eta=12}$ (Table 2.3). For all melts, oxidized or reduced, the fragility index varies between 56.5 and 64.2. The addition of iron slightly increases the fragility, while it is decreasing with Fe reduction (Table 2.3).

2.4 Discussion

2.4.1 Structure-property relations affecting viscosity

One model for describing the viscous behavior of silicate melts is based on the configurational rearrangement of the melt structure with temperature (e.g. Richet, 1987b). The Adam-Gibbs theory (Adam and Gibbs, 1965) is commonly used to describe the temperature dependence of silicate melts viscosity as a function of the configurational entropy (e.g. Neuville and Richet, 1991; Richet and Bottinga, 1995; Sipp et al., 1997; Toplis et al., 1997; Romano et al., 2003) via:

$$\log\eta = A_{AG} + \frac{B_{AG}}{T \cdot S^c} \quad (2.4)$$

where A_{AG} is a pre-exponential factor equivalent to a lower limit of silicate melt viscosity at high temperature; B_{AG} the activation energy; and S^c , the configurational entropy of

the liquid. A_{AG} is a constant independent of temperature and composition (Russell et al., 2003; Giordano and Russell, 2007) whereas B_{AG} is dependent upon composition and S^C is both temperature and compositionally dependent (Toplis, 1998). This theory represents a reliable way to incorporate the viscosity data into a model, since the theoretical basis outlined here allow confident extrapolation beyond the range of conditions of the viscosity measurements. As discussed in previous contributions (e.g. Richet and R., 1992; Toplis et al., 1997; Giordano et al., 2009), S^C can be expressed as the sum of two competing bonding mechanisms, namely the “topological” and the “chemical” contributions. The “topological” contribution has to be referred as the distribution of the bonding angles and lengths at the short- and intermediate-range order in the oxygen lattice of the silicate network (e.g. Henderson, 2005; Stebbins, 2008). On the other hand, “chemical” contribution is a reflection of the ability of various cations, competing with their neighbourhoods, to adopt new configurations. This contribution is proportional to the degree of polymerization, and to the viscosity of silicate melts Giordano et al. (2009). To represent the degree of polymerization, NBO/T (Mysen, 1988) or, as suggested by Giordano and Dingwell (2003), the sum of structure modifiers (SM parameter) can be used. Here, both parameters have been calculated on the basis of the measured iron redox ratio considering Fe^{3+} as a network former and Fe^{2+} as network modifier (Mysen et al., 1984) and are reported in Table 2.3. For a given redox state, the depolymerisation is therefore directly proportional to iron content. Treating the investigated melts as pseudo-binary mixture between iron-free and iron-bearing AD component, the variation of ΔH_η in Figure 2.5 represents the activation energy of mixing due to the addition of total iron, hence decreasing polymerisation. At low-T, the non-linearity of indicates significant “chemical” interactions between the components of the mixture. This observation is strongly supported by previous studies on silicate melts (e.g. Neuville and Richet, 1991; Toplis et al., 1997) and has been recently extended for a large body of anhydrous and hydrous natural multicomponent melts by Giordano et al. (2009). A comparison with this latter study is shown in Figure 2.8 where the isothermal viscosity variation of natural multicomponent melts is plotted as a function of the structure modifiers parameter. The viscosity distribution becomes gradually more scattered and curved towards the lower temperatures where chemical interactions are more significant. At the lowest temperature (1070 K), the isothermal viscosity variation for the samples measured in this work (SM > 40 mol. %) show a marked contrast with the overall trend. The discrepancy is stronger for the pure AD sample (higher viscosity) and tends to vanish as iron is added to the AD melt. This observation demonstrates that a simplified melt such as the AD-eutectic does not follow the overall viscosity trend of natural multicomponent melts. On the other hand, it appears that the dissolution of a certain amount of iron is of critical importance to reduce

the chemical interaction between the cations in the AD-eutectic system and yield the overall trend of multicomponent melts for these compositions. This suggest that iron-bearing AD melts are better analogue to natural systems.

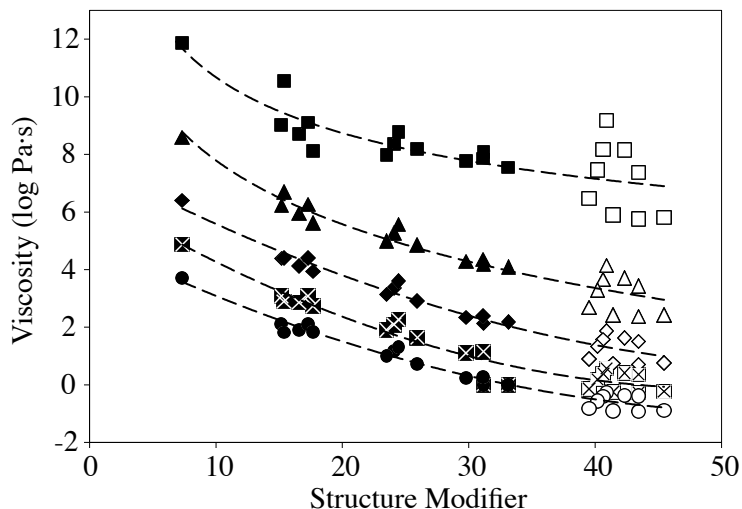


Figure 2.8: Isothermal viscosity curves as a function of the SM parameter approximating the degree of polymerization. Numbers in the figures are isotherm temperatures and are the same for all panels. The full symbols are from previous study (Giordano et al., 2009) and empty symbols from this study.

2.4.2 Effect of redox state

At high temperature, investigation of the effect of iron redox on viscosity reveals a slight viscosity decrease as the melt is reduced that is in the same order of magnitude as previous observation on basaltic composition (Bouhifd et al., 2004). However, for other compositions, the redox effect was observed to be stronger (Dingwell and Virgo, 1987). This difference may be attributed to 1) the lack of highly oxidized melt compositions in this study; 2) the fact that ferric and ferrous iron may have similar structural roles in the present melts at very high temperatures or 3) the presence of alkaline earths (e.g., Mg and Ca), which render the effect of iron on the melt structure less effective with respect to alkalis (Dingwell, 1991; Dingwell and Virgo, 1987, 1988; Toplis et al., 1994). Although the viscosity decrease is small, the non-linear trend is consistent with the observations of Dingwell (1991). Near the glass transition temperature the viscosity is more sensitive to the redox state. For AD-20, a decrease of one log unit is observed between the sample equilibrated in air ($\text{Fe}^{2+}/\text{Fe}_{\text{tot}}=0.18$) and the most reduced sample ($\text{Fe}^{2+}/\text{Fe}_{\text{tot}}=0.67$). The non-linear decrease of the calorimetric limiting T_f' with reduction of the melts leads to non-linear decrease for the calculated viscosity. As in high temperature studies, viscosity

decreases with iron reduction until a minimum value is reached around $\text{Fe}^{2+}/\text{Fe}_{\text{tot}} = 0.5$ and then remains constant with further reduction. This observation is consistent with the previous study of Cukierman and Uhlmann (1974) on lunar iron-rich basalt. In their study, melt reduction (from $\text{Fe}^{2+}/\text{Fe}_{\text{tot}} = 0.2$ to 0.76) involved a viscosity decrease of two orders of magnitude whereas further reduction ($\text{Fe}^{2+}/\text{Fe}_{\text{tot}} = 0.94$) yielded no further viscosity change. Liebske et al., 2003 also found in experiments on andesite composition that, in the same way, viscosity decreases non-linearly with iron reduction; the difference between an oxidized ($\text{Fe}^{2+}/\text{Fe}_{\text{tot}} = 0.42$); and the reduced sample ($\text{Fe}^{2+}/\text{Fe}_{\text{tot}} = 0.79$) was 1.6 log units at 1061 K. The decrease of viscosity with reduction of iron that is correlated to an increase of depolymerisation suggests that Fe^{3+} acts as network former while Fe^{2+} acts as network modifier. In contrast, the invariant viscosity after further reduction than $\text{Fe}^{2+}/\text{Fe}_{\text{tot}} = 0.5$ hints that iron may develop different coordination state at low $f\text{O}_2$. Mysen (1991) suggested that an octahedral coordination is preferred by ferric iron under reducing conditions. We recommend that future studies incorporate iron redox state in multicomponent viscosity models applicable to natural systems.

2.4.3 Experimental limitation for oxidized iron-rich melts

The calorimetric measurements for the sample AD-20-S1 ($\text{Fe}^{2+}/\text{Fe}_{\text{tot}} = 0.18$) that was equilibrated in air were experimentally challenging. For the same heating/cooling rate the cycles were not reproducible. As soon as the glass transition peak was overcome the heat capacity curve shows an exothermal peak and the calorimetric liquid field could never be reached. Even if the heating is stopped as soon as the peak is reached, the next cycle with the same heating/cooling rate shows a shift toward higher temperatures. In contrast, samples equilibrated in reduced conditions are more “stable” through the glass transition until the liquid field and measurements were reproducible by crossing the glass transition back and forth. As shown by Bouhifd et al. (2004), crystal nucleation strongly increases with increase of iron content and iron oxidation. Although no crystals are visible with Secondary Electron Microprobe images, we suspect that nano-crystals could be evidenced within the oxidized sample using Transmission Electron Microscopy (Bouhifd et al., 2004; Liebske et al., 2003). The shift of the glass transition temperature toward higher value is in agreement with the possible crystallization, as the matrix would evolve toward higher silica content and hence higher T_g values. The T_f value presented here for AD-20-S1 are therefore the best that could be obtained, but should be treated with caution. The properties of iron-rich melts near the glass transition temperature must be investigated with care for oxidized sample, avoiding nano-crystallization.

2.4.4 Applications to extra-terrestrial magmatism

Figure 2.9 displays a comparison of the viscosity measured in this study with data available in the literature on undersaturated iron-rich natural composition from the Earth (Giordano and Dingwell, 2003; Toplis et al., 1994; Kushiro et al., 1976; Gottsmann et al., 2002; Bouhifd et al., 2004) and from the Moon (Murase and McBirney, 1970; Cukierman et al., 1973; Uhlmann et al., 1974).

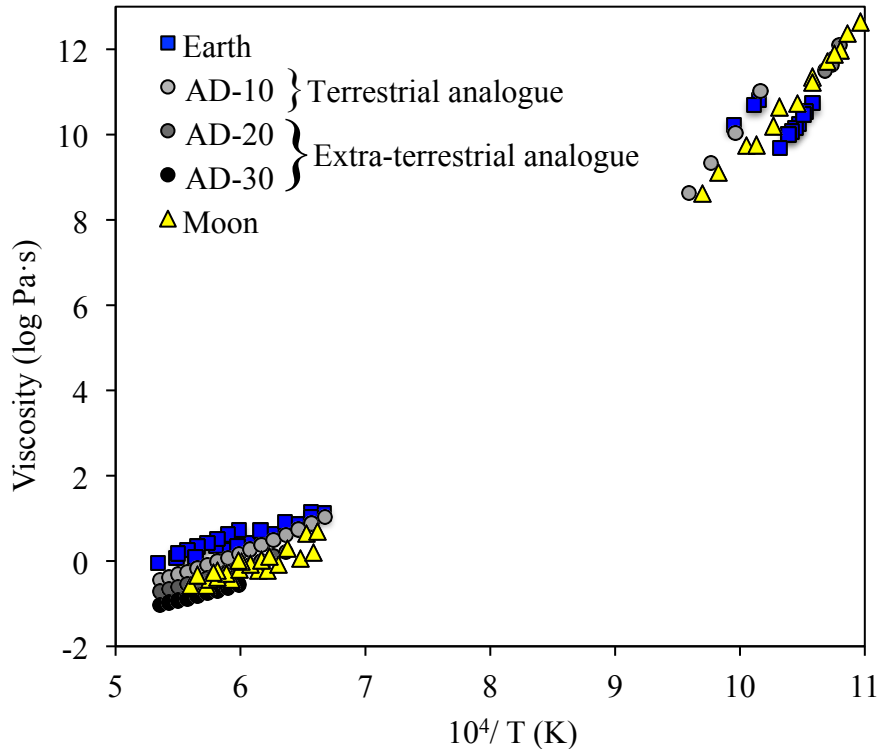


Figure 2.9: Viscosity of basaltic melts experimentally determined, comparison between this study (circles) and terrestrial (square) and lunar (triangles) data. Terrestrial compositions include trachy-basalt from Etna (Giordano and Dingwell, 2003), ferro-basalt (Toplis et al., 1994), basalt from Hawaii (Kushiro et al., 1976; Gottsmann et al., 2002, and R839-5.8) and basalt from Stein Frenz (Bouhifd et al., 2004). Lunar compositions include Ti-rich basalt from Apollo 11 (Murase and McBirney, 1970), green glass basaltic composition from Apollo15 (Uhlmann et al., 1974) and mare basalt from Hadley rille (Cukierman and Uhlmann, 1974).

Iron-bearing AD melts cover the same viscosity range, and have similar patterns, to those observed for terrestrial and extra-terrestrial melts. Giordano et al. (2008) showed that Anorthite-Diopside eutectic melt cannot be used as quantitative analogue for calculating the viscosity of Etna basalt because of the differing fragilities of the two melts. However, here we show that iron significantly lowers the activation energy of viscous flow at low temperature and brings the iron-bearing Anorthite-Diopside system closer to ap-

proximate the behavior of natural multicomponent melts. Iron is therefore a requirement in the construction of a basaltic equivalent for terrestrial and extra-terrestrial magmas. Based on our results on iron-bearing Anorthite-Diopside, the difference in viscosity at temperatures of eruption between AD-10, analogous to ‘common’ terrestrial basalts (with 10 wt. % $\text{Fe}_2\text{O}_{3\text{tot}}$) and AD-20, analogous to lunar or Martian basalt (with 20 wt. % $\text{Fe}_2\text{O}_{3\text{tot}}$), is estimated to be between 0.5 and 1 order of magnitude. This belief is consistent with the experimental investigation of lunar basalt viscosity displayed in Figure 2.9. The predicted low viscosities are also coherent with morphological interpretation of lava flow on the Moon and on Mars (Huppert and Sparks, 1985; Cas et al., 1999; Baratoux et al., 2009; Hauber et al., 2009; Vaucher et al., 2009a). The low viscosity calculated in Vaucher et al. (2009a) for young lava flows in CEP province on Mars could partly be explained by high iron content. Although no chemical data are available on this area, the nearest volcanic province, Elysium Mons contains the highest iron content observed on Mars (21-22 wt. %). Furthermore iron-rich basalt has a high liquidus temperature and this implies that during eruption a solid crust would form rapidly, forming tubes and allowing the lava to travel very long distances. However, it is important to highlight that the relationship between the viscosity of extruded lava and the final morphology of a flow is not yet well defined. The lava flow behavior depends more on the crystallization sequence than on the pure melt viscosity. The crystallization sequence of such iron-rich basalt needs further attention in order to draw solid conclusions on the quantitative behavior of extraterrestrial lava flows (as described in the next chapter).

2.5 Conclusion

This is the first systematic study of the physical and thermodynamic properties of iron-bearing Anorthite-Diopside-eutectic melts as a proxy for extra-terrestrial magmas. Our investigation shows that viscosities of the investigated analogue melts match the viscosities of natural terrestrial and extra-terrestrial basalts well. We outline here that iron can dramatically affect viscosity and the glass transition temperatures. The addition of 20 wt. % of iron to the Anorthite-Diopside eutectic composition produces a significant absolute viscosity decrease of up to two log units near the glass transition and, one log unit at magmatic temperature. The iron-rich basaltic compositions such as those found on the Moon or on Mars should have, at eruption temperature, a lower viscosity than ‘common’ terrestrial basalts. To conclude the low viscosity of iron-bearing melts would enhance the transport distance of magma traveling through the crust and or at the surface, however the crystallization sequence should be investigated to draw quantitative conclusions on extra-terrestrial lava flow behavior.

The investigation of the effect of iron redox state is consistent with previous studies that also observed a viscosity decrease with reduction of iron. Iron speciation appears to influence viscosity strongly above a certain concentration and near T_g . From calorimetric measurements we infer that there is a threshold at $Fe^{2+}/Fe_{tot} = 0.5$ beyond which the glass transition temperature ceases decreasing and viscosity becomes constant. The reduced supercooled melts are more ‘stable’ through the glass transition and show lower fragility than oxidized melts. Even if at high temperature the redox state of iron does not have a massive effect on viscosity, care should be taken when oxidized iron-rich melt (equilibrated in air) are analysed near the glass transition. To conclude, for basaltic magmas that contain high iron concentration (above 10 wt. %), the redox state must be determined in order to obtain more accurate estimation of the physical and thermodynamic properties, especially at low temperatures.

CHAPTER 3

Planetary lava flow rheology: a
comparison of morphological and
rheological methods

Abstract

In planetary sciences, the emplacement of lava flows is commonly modeled using a single rheological parameter (apparent viscosity or apparent yield strength) calculated from morphological dimensions using Jeffreys' and Hulme's equations. The rheological parameter is further interpreted in terms of the nature and chemical composition of the lava (e.g., mafic or felsic). Without the possibility of direct sampling of the erupted material, the validity of this approach has remained largely untested. In modern volcanology, the complex rheological behavior of lavas is measured and modeled as a function of temperature, chemical composition and crystal content. Here, we test the planetary approach on a terrestrial basaltic lava flow from the Western Volcanic Zone in Iceland. The geometrical parameters required to employ Jeffreys' and Hulme's equations are accurately estimated from high-resolution Digital Elevation Models. Samples collected along the lava flow are used to constrain a detailed model of the transient rheology as a function of cooling, crystallization, and chemical composition evolution of the residual melt during emplacement. We observe that the rheological properties derived from the morphology correspond to a critical value estimated near solidification of the material, where significant crystallization inhibits viscous deformation, causing the flow to halt. Our results indicate that the rheological values typically derived from the morphological approach is highly dependent on the details of the crystallization sequence and crystal shapes, and as such, is neither uniquely nor simply related to the bulk chemical composition of the erupted material. This conclusion, drawn for a mafic lava flow where crystallization is the primary process responsible for the increase of the viscosity during emplacement should apply to most of martian, lunar, or mercurian volcanic landforms, which are dominated by basaltic compositions.

3.1 Introduction

The morphology of lava flows is commonly used to infer the eruption setting (vent size, effusion rate) and the rheological properties (e.g., viscosity, yield strength) of the erupted material (Pinkerton, 1987; Wilson and Head, 1994). In recent decades, the release of high-resolution topographic data, in the context of the exploration of our solar system, has offered new perspectives on extraterrestrial volcanism, which has in turn led to a surge of studies on the dynamics of magmatic and volcanic processes (e.g., Greeley and Spudis, 1981; Greeley, 2005; Wilson and Head, 1983, 1994; Wilson et al., 2009; Zimbelman, 1985, 1998; Glaze et al., 2003; Baloga et al., 2003; Neukum et al., 2004; Fairen and Dohm, 2004; Hiesinger et al., 2007; Garry et al., 2007; Glaze and Baloga, 2007; Baptista et al., 2008; Hovius et al., 2008; Vaucher et al., 2009b,a; Williams et al., 2009; Byrne et al., 2009; Carr and James, 2010; Hauber et al., 2009, 2011; Jaeger et al., 2010; Lang et al., 2010; Pasckert et al., 2012; Baratoux et al., 2009, 2011; Platz and Michael, 2011; Platz et al., 2011, and references therein). In these studies, simple isothermal models of lava flow emplacement have been used and, importantly for the present study, the assumption that a single rheological parameter may be inferred from the final morphology of a lava flow has been made. Nichols (1939) proposed the Jeffreys' equation (Jeffreys, 1925) to extract the viscosity of a lava flow from its morphology, assuming that it exhibits a Newtonian viscous response. Recognizing that crystallizing lava may no longer behave as a Newtonian fluid (e.g. Shaw, 1969; Murase and McBirney, 1973), a method was later proposed to approximate the rheological behavior of the lava with a Bingham law, which employed the concept of yield strength ($\tau_{0,\text{flow}}$) to describe the final morphology of a flow as a function of its underlying surface topography (Hulme, 1974; Moore et al., 1978). Experiments with analogue material demonstrate that the morphology of lava flow may be used to infer the rheology (e.g., Fink and Griffiths, 1992; Gregg and Fink, 1996, 2000; Lyman et al., 2004). Walker (1973) and Pinkerton and Wilson (1994) went further proposing that the silica content of a lava flow, which strongly influences the viscosity, may in turn be estimated by morphological approaches. They distinguished between three chemical compositions based on the viscosity: basaltic below 10^5 Pa·s, andesitic between 10^5 and 10^9 Pa·s, and rhyolitic above 10^9 Pa·s. Application of this approach to lava flows observed on Mars yields lava viscosities ranging between 10^2 and 10^8 Pa·s, and thus having basaltic or basaltic-andesitic compositions (e.g. Zimbelman, 1985; Glaze et al., 2003; Hiesinger et al., 2007; Vaucher et al., 2009b; Hauber et al., 2011; Pasckert et al., 2012, and references therein). For lava flows in the region of Central Elysium Planitia, some peculiar, very low viscosities on the order of 10^2 Pa·s have been estimated, which have been inferred to express the eruptions of silica-poor, iron-rich basaltic lavas (Vaucher et al., 2009a).

Generally speaking of course, the viscosity of lava during emplacement is transient,

as it is cooling and crystallizing during flowing. Thus the approximation of a single viscosity value neglects important physico-chemical processes, which are expected to affect considerably the rheology of lava. Thus further validation of morphological methods, is becoming increasingly imperative. The study of silicate melt rheology has rapidly advanced in the last three decades. We now have a reasonable description of the rheology of silicate liquids as a function of temperature and chemical composition (e.g. Shaw, 1972; Bottinga and Weill, 1972; Dingwell, 2006, 1996; Giordano and Dingwell, 2003; Hui and Zhang, 2007; Giordano et al., 2008). Furthermore, a reasonable understanding of the rheological effects of crystals (e.g. Ryerson et al., 1988; Pinkerton and Stevenson, 1992; Lejeune and Richet, 1995; Pinkerton and Norton, 1995; Saar et al., 2001; Sato, 2005; Dingwell, 2006; Ishibashi and Sato, 2007; Caricchi et al., 2007; Costa, 2005; Costa et al., 2009; Petford, 2009; Ishibashi, 2009; Mueller et al., 2010; Castruccio et al., 2010; Vona et al., 2011; Cimarelli et al., 2011), bubbles (Bagdassarov and Dingwell, 1992; Lejeune et al., 1999; Stein and Spera, 2002; Manga et al., 1998; Saar and Manga, 1999), and their combined effects (Bagdassarov et al., 1994; Stein and Spera, 1992; Lavallée et al., 2007, 2012; Harris and Allen, 2008; Pistone et al., 2012) is emerging. The rheological implication of crystals and bubbles are composed of contributions to the Newtonian description as well as the onset of non-Newtonian effects (e.g. Lavallée et al., 2007; Caricchi et al., 2007). The apparent viscosity (η_{app}) of a polydispersed particle mixture (crystals and bubbles of various shapes and sizes) in a liquid phase (the silicate melt) may be defined by:

$$\eta_{app} = \eta_{melt} \times \eta_r = \eta_{melt}(T, \chi) \times \eta_r(\phi, r, \dot{\gamma}) \quad (3.1)$$

where η_{melt} , the viscosity of the interstitial silicate melt, is Newtonian and depends on temperature T and composition (χ), and η_r , the relative viscosity, depends on the particles' volume content (ϕ) and aspect ratio (r) as well as strain-rate ($\dot{\gamma}$). The suspension may further be sensitive to strain as crystals and bubbles deform and align in the flow lines but these effects are not yet sufficiently well-accounted for. Therefore, the rheology of magmatic suspensions, with its phenomena of strain and strain rate dependence, needs, in general, a non-Newtonian description. Complexity in describing the non-Newtonian nature has led to the proposal that above a critical crystal fraction, the rheology may be simplified to a Bingham fluid (Ryerson et al., 1988; Pinkerton and Stevenson, 1992) defined by its yield strength τ_0 , (T, ϕ). Despite of recent experiments on multiphase magmas that refuted the existence of a yield strength (Lavallée et al., 2007; Caricchi et al., 2007), its assumption persists in the modeling of lava flows because it permits simplifications for computation. How robust is then the description of the morphology of a lava flow in terms of a single effective rheological parameter (either viscosity or yield strength) reflecting the chemical composition and crystallization sequence associated with a particular cooling

history? From a rheological point of view, this approach is highly insufficient as during the emplacement of a cooling-limited, basaltic lava flow, heat lost induces crystallization and consequently, changes in the residual liquid composition, which, in combination, may increase the apparent viscosity of the flow by several orders of magnitude between the vent and the point at which the flow halts. Nevertheless, it was shown by Giordano et al. (2007) that under compositional conditions, the concept of a rheological cut-off does provide an effective rheological proxy for flow emplacement temperature. Our approach combines 1) the determination of the rheological parameters from high-resolution morphological analysis, and 2) the determination of the rheological evolution of the lava due to crystallization from onset of the eruption until solidification. To address this question, we focus here on a 4000 year old basaltic lava flow from the Western Volcanic Zone in Iceland. As volcanic flows on Mars, the Moon and Mercury are dominated by basaltic compositions, the applications of our results to planetary data should be straightforward.

3.2 Methods

3.2.1 Morphological analysis

Topographic imaging

In 2006, the HRSC-AX, an airborne version of the High Resolution Stereo Camera (HRSC) on board Mars Express, was used for the acquisition of stereo and color images of the Western Volcanic Zone, Iceland (Figure 1). The HRSC-AX is a multi-sensor push-broom instrument with 9 CCD line sensors and has the particular value of having a stereo capability, which can systematically produce high-resolution Digital Elevation Models (DEMs). The principles of HRSC-AX data processing are similar to that of Mars Express-HRSC processing (see Scholten et al., 2005; Gwinner et al., 2010). The orientation data of the camera is reconstructed from a GPS/INS (Global Positioning System/Inertial Navigation System). The ortho-images acquired here have a map projected resolution of 25 cm/pixel, and the DEM has a vertical resolution of 10 cm, an absolute accuracy of ~ 20 cm, and a horizontal grid spacing of 1 m.

Extracting rheological parameters

Rheological parameters of remotely observed lava flows are calculated using Jeffreys' and Hulme's equations commonly used in planetary sciences (Nichols, 1939; Hulme, 1974; Zimbelman, 1985; Glaze et al., 2003; Hiesinger et al., 2007; Vaucher et al., 2009a; Hauber et al., 2011; Pasckert et al., 2012, and references therein). The cooling-limited length of a lava flow is related to the dimensionless Grätz number, G_Z (Knudson and Katz, 1958;

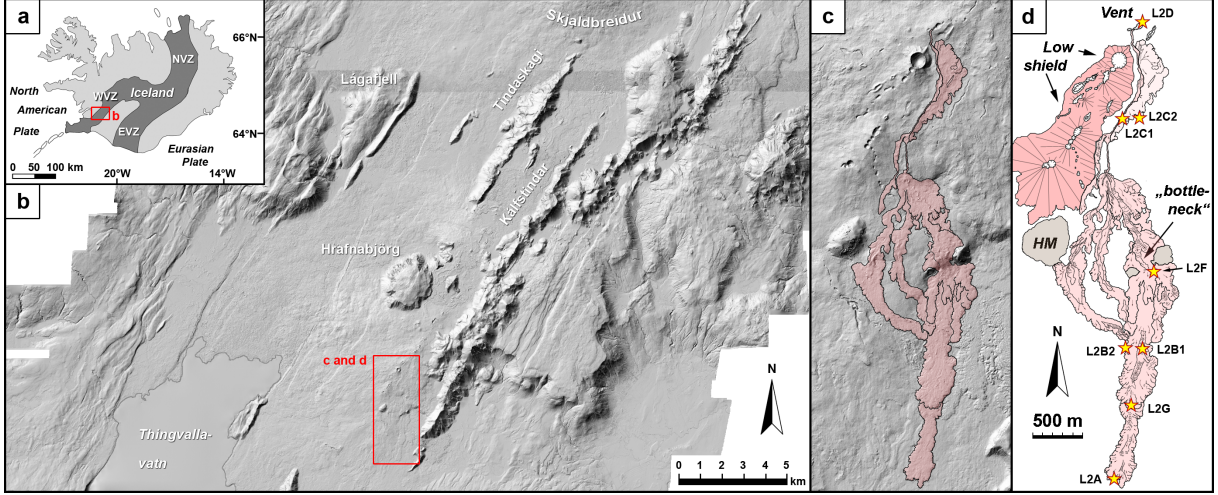


Figure 3.1: (a) Location of the Western Volcanic Zone (WVZ) in Iceland; (b) Orthophoto of the area acquired with the HRSC-AX camera and location of the lava flow. (c) Highlight of the lava flow on the Data Elevation Model; (d) Mapping of the lava flow (light pink) and location of the sampling (stars). *HM (Hyaloclastite mount)

Pinkerton and Wilson, 1994), which considers conductive heat losses to heat advection along the flow length:

$$G_z = \frac{ud_e^2}{\kappa L} \quad (3.2)$$

where u is the mean flow velocity, L is the length of the lava flow, κ is the thermal diffusivity and d_e is the equivalent diameter of the flow (Knudson and Katz, 1958). Several studies have described the relationship between the effusion rate and the flow length (Walker, 1973; Pinkerton and Wilson, 1994; Pinkerton and Sparks, 1976) and concluded that cooling-limited flows halted when G_z falls to a critical value of 300. This value was later confirmed by extrapolation of the relationship between the calculated G_z numbers and the drainage distance for 20 episodes of lava flows at Pu'u'Ō'o, Hawaii (Pinkerton and Wilson, 1994). The velocity of the extruded lava is related to the effusion rate Q by:

$$Q = uWH = \frac{G_z \kappa LW}{H} \quad (3.3)$$

where W and H are the flow width and flow height, respectively.

Assuming that a lava flow behaves as a Newtonian fluid, its geometry on an inclined surface depends on its viscosity, density, effusion rate, and the force that drives the flow (i.e., gravity), and is given by (Jeffreys, 1925; Nichols, 1939):

$$\eta_{flow,1} = \frac{\rho g H^3 W \sin \alpha}{nQ} \quad (3.4)$$

where $\eta_{flow,1}$ is the flow viscosity, g is gravity, ρ is the density, and α is the slope of the

underlying surface. The parameter, n , is a constant of 3 or 4 for wide and narrow flows, respectively. A simplified equation was later proposed by (Warner and Gregg, 2003):

$$\eta_{flow,2} = \frac{\rho g H^4}{Q} \quad (3.5)$$

which omits the effect of lateral extent of the flow and the slope. Results of equations 3.4 and 3.5 generally agree well if the flow does not develop levees and if the flow width is considerably wider than the flow height (Moore and Schaber, 1975). Alternatively, assuming that the flow obeys a Bingham law the yield strength of the flow may be related to the geometric parameters (Hulme, 1974; Moore et al., 1978) according to:

$$\tau_{0,flow,1} = \rho g H^2 \sin \alpha \quad (3.6)$$

The yield strength can also be calculated using the lateral spreading of the Bingham fluid, which is independent of the topographic gradient in the flow direction:

$$\tau_{0,flow,2} = \frac{\rho g H^2}{W} \quad (3.7)$$

In the context of channelized lava flows, the yield strength and viscosity can be derived using (Wilson and Head, 1983; Zimbelman, 1985):

$$\tau_{0,flow,3} = \rho g (W - w) \sin^2 \alpha \quad (3.8)$$

and

$$\eta_{flow,3} = \frac{w^3 W \tau_{0,flow,3} \sin^2 \alpha}{24Q} \quad (3.9)$$

with $\frac{w}{W-w} < 1$ and w being the channel width.

3.2.2 Sampling and analytical methods

One particular lava flow was select within the area surveyed by the HRSC-AX camera in the Western volcanic zone, Iceland (Figure 3.1). This lava flow is part of the Thjó-fahraun volcanic unit, resulting from the late pause of a fissure eruption event, which was dated at approximately 4000 years B.P. (Sinton et al., 2005; Eason and Sinton, 2009). It was chosen because it has a main strait stream that is ideal to evaluate the geometrical parameters. Moreover it is easily accessible to do a ground proof and to be sampled. The lava flow was surveyed during a field campaign in August 2010. Eight samples were selected at several distances from the vent to the flow front (Figure 3.1). For two sampling sites, pairs of samples were collected from the flow margin and centre (L2B1-L2B2 and L2C1-

L2C2). Specimens from the flow top and outer margins were obtained, but the interior and the base of the flow could not be reached owing to the lack of erosion and crevasses. To check for the homogeneity of the flow, bulk rock geochemical analyses of five samples were carried out at the Service d'Analyse des Roches et des Minéraux (Nancy, France) via Inductively Coupled Plasma Optical Emission Spectrometry (ICP-OES) technique. Details of the methodology and uncertainties of this technique can be found in Carignan et al. (2001). Quantitative elemental analysis and back-scattered electron images were collected using a CAMECA SX100 Electron MicroProbe Analyser at the University of Munich according to the PAP procedure (Pouchou and Pichoir, 1985). Single images acquired with a polarized microscope were merged to portray the entire thin sections. Vesicles and crystals larger than 200 μm were colorized in an area of $\sim 1000 \times 1000$ pixels. The resulting images were then processed by color threshold separation for each phase using the free software package ImageJ (<http://rsb.info.nih.gov/ij/>). The proportion of vesicles and crystals are obtained by area pixel counting on binary images (crystals count are done on a bubble-free area).

3.2.3 Crystallization sequence

The crystallization sequence was first determined by petrographic observations. The temperature of the onset of olivine crystallization was calculated using the ‘Olivine-liquid thermometer’ (Putirka, 2008) in which the core of the olivine was considered in equilibrium with a liquid having the bulk rock composition. The modal abundance of each phase as a function of temperature was then determined using the thermodynamic calculator MELTS (Ghiorso and Sack, 1995). MELTS calculates from minimization of Gibbs energy the composition and proportions of solids and liquids at thermodynamic equilibrium for prescribed pressure-temperature path and oxygen fugacity constraints. The crystallization sequence was run in three steps to simulate the eruptive history of the lava from (i) phenocryst crystallization in the magmatic chamber, to (ii) adiabatic ascent, and (iii) cooling and micro-crystallization at the surface. Crystallization in the magma chamber was simulated by decreasing the temperature from the liquidus to the eruption temperature at a constant pressure of 1 kbar. As suggested by Eason and Sinton (2009), 0.4 wt.% of water was added to the initial composition. The temperature of eruption is constrained by the temperature that is modeled by MELTS to achieve the crystallinity of the phenocryst assemblage observed in the thin sections. Crystallization induced by the eruption during the ascent of the magma, was simulated using isothermal conditions and a pressure gradient from magma chamber conditions to the surface pressure of 1 bar. [Note: The increase temperature due to adiabatic decompression was neglected]. Finally the cooling of the lava flow at the surface was simulated from eruptive temperature to

complete crystallization, using a pressure of 1 bar. The oxygen fugacity was held constant at two log units below the QFM buffer (QFM-2) in all steps (Eason and Sinton, 2009).

3.2.4 Viscosity modeling

The calculation of viscosity during crystallization combines thermodynamic modeling and empirical rheological models. The composition of the interstitial residual liquid is calculated for every temperature increment from the calculations obtained with MELTS and its viscosity (η_{melt}) is estimated via the GRD model (Giordano et al., 2008). This model was chosen over other models (e.g., Shaw, 1969; Bottinga and Weill, 1972; Hui and Zhang, 2007) because it considers a wide range of chemical compositions and includes the non-Arrhenian temperature dependence of silicate melt viscosity following the Tammann-Vogel-Fulcher equation (Tammann and Hesse, 1926; Vogel, 1921; Fulcher, 1925):

$$\log \eta_{\text{melt}} = A + \frac{B(\chi)}{T - C(\chi)} \quad (3.10)$$

where T is the temperature and A is a constant representing the lower limit of silicate melt viscosity at high temperature; and B and C are fitting parameters, which are calculated from the melt composition (χ).

The presence of suspended particles (crystals and/or bubbles) drastically modifies the apparent viscosity of the liquid. In the conduit, volatile exsolution and subsequent bubble growth can cause an increase or in some cases a decrease of apparent viscosity, depending on strain rate, volume fraction and ability of bubbles to deform (Lejeune et al., 1999). This ability depends mainly on the capillary number that is highly variable in lava flows (Manga et al., 1998); if the vesicles remain inviscid (i.e., do not deform), their presence will increase the apparent viscosity of the suspension but if they deform (i.e., stretching), the apparent viscosity might decrease. Vesicles are present in our samples, and bubbles have likely affected the flow behavior (e.g., Pinkerton and Sparks, 1978; Lipman et al., 1985). However, at present, there exists no general law describing their effect on the apparent viscosity of a bubbly lava (Stein and Spera, 1992; Pistone et al., 2012). Here we will use current state-of-the-art rheological laws and focus only on the effect of the crystalline phases. As a general observation, the relative viscosity (η_r) increases with increasing crystal volume fraction. A first attempt to quantify the effect of crystals in a magma was proposed by Shaw (1969) using the Einstein-Roscoe equation:

$$\eta_r = (1 - 1.35\phi)^{-2.5} \quad (3.11)$$

where ϕ is the particle volume fraction. This equation was suggested to apply only for

dilute concentration of spherical particles. Krieger and Dougherty (1959) modified this equation to:

$$\eta_r = \left(1 - \frac{\phi}{\phi_m}\right)^{B\phi_m} \quad (3.12)$$

where ϕ_m represents the maximum packing fraction that is the maximum crystal fraction achieved by accumulation of randomly oriented solids for a given size and shape distribution (e.g., Mueller et al., 2010; Cimarelli et al., 2011), where B is the Einstein coefficient (a dimensionless number representing the “intrinsic viscosity”). The effect of the mixture of coarse phenocrysts modeled as spheres and finer microlites modeled as needles is approximated by the product of the relative effect of each particles ($\eta_r = \eta_r(\phi_c) \times \eta_r(\phi_f)$ Farris, 1968; Cimarelli et al., 2011). The analytical expression predicts a sharp viscosity increase when solid fraction approaches the maximum packing, commonly associated with the onset of apparent yield strength, τ_0 (Zhou et al., 1995; Hoover et al., 2001; Saar et al., 2001). When considering time-scales shorter than those required to observe deformation, rheological studies have therefore employed Bingham flow laws, accounting for a yield strength (see Barnes, 1999). Under such conditions, the relationship between yield strength and particle volume fraction has been tested, but the answer is not unique (Castruccio et al., 2010, see Table 3.1 for a compilation of the models available in the literature). Under sufficiently long time-scale, it has been observed that the behavior of crystal-bearing magmas is better described by a shear thinning law with a strain rate dependency and absence of yield strength (e.g., Caricchi et al., 2007; Lavallée et al., 2007). In a complementary attempt, Costa (2005) and Costa et al. (2009) compiled a large experimental data base and formulated a semi-empirical non-Newtonian relationship for dilute- to highly-concentrated polydisperse suspensions, taking into account the shape of the particles and the strain-rate dependency. This equation also reproduce the transition from the regime where the strength is controlled by melt viscosity up to the beginning of the regime where strength is controlled by the solid framework, avoiding the singularity predicted by classical models at the maximum packing fraction.

$$\eta_r(\phi) = \frac{1 + \left(\frac{\phi}{\phi_m}\right)^\delta}{\left[1 - F\left(\frac{\phi}{\phi_m}, \xi, \gamma\right)\right]^{B\phi_m}} \quad (3.13)$$

with F is given by:

$$F = (1 - \xi) \operatorname{erf} \left[\frac{\sqrt{\pi}}{2(1 - \xi)} \frac{\phi}{\phi_*} \left(1 + \frac{\phi^\gamma}{\phi_*^\gamma}\right) \right] \quad (3.14)$$

where ϕ_* represents the critical solid fraction at the onset of the exponential increase of η depending on ϕ_m and ξ , γ and δ are empirical parameters that depend on strain rate

Equation	Reference	Notes
(1) $\tau_0 = 1.26\rho g(D_p/(\phi_m - \phi))(\phi_m/(1 - \phi_m))^2 (1/(\xi^{1.5} - \sigma^2))$	Gay et al., 1969	ρ is the density of the lava (2600 kg.m ⁻³); D_p is the mean diameter of particles; ξ is the shape factor defined as the ratio of the surface area of a sphere of equivalent volume to the surface area of the particle, σ is the geometric standard deviation that is estimated from a plot of particle diameter versus the cumulative proportion of particles less than a given size. The values used here are similar to Pinkerton and Stevenson (1992); $D_p = 100\mu\text{m}$, $\xi = 0.5$; $\sigma = 1.5$
(2) $\tau_0 = 6500\phi^{2.85}$	Ryerson et al., 1988	Experimental fit obtained from crystallisation of picritic lava
(3) $\tau_0 = a(\exp(b(Tl - T)) - 1)$	Dragoni et al., 1989	Tl is the liquidus temperature, a et b are fitting parameters given by Dragoni et al., 1989: $a = 0.01$ and $b = 0.08$. This equation is based on a linear relationship between temperature and crystallization.
(4) $\tau_0 = \tau_c (((\phi/\phi_c) - 1)/(1 - (\phi/\phi_m)))^{1/p}$	Zhou et al., 1995; Saar et al., 2001	τ_c reflects the total inter-particulate cohesion resisting to hydrodynamic forces and p may reflect the response of the aggregate state to shearing; ϕ_c is the critical minimum particles concentration at which the suspension can sustain some external stress (onset of yield strength). The values used here are similar to Hoover et al., 2001, for prism with $p = 1$ and $A = 6.9$, however the absolute value of this last is not meaningful for geological material.
(5) $\tau_0 = \tau^* ((1 - (\phi/\phi_m))^{-2} - 1)$	Mueller et al., 2010; Heymann et al., 2002	τ^* is a fitting parameter related to the size of the particles. The values used here are similar to Mueller et al., 2010 with $\tau^* = 0.234$ for spheres and $= 0.087$ for needles.
(6) $\tau_0 = D(\phi - \phi_c)^8$	Castruccio et al., 2010	$D = 5 \cdot 10^6$ Pa and ϕ_c is the critical minimum particles concentration

Table 3.1: Equations to calculate the yield strength as a function of crystal fraction.

and on the particles shape. Here, we employ the Costa model with fitting parameters based on analogue experiments of polydisperse suspensions consisting of coarse, equant particles (to mimic olivine phenocrysts) and fine, prolate particles (to mimic plagioclase microlites) in a bubble-free Newtonian liquid (analogous to the interstitial silicate melt) (see Cimarelli et al., 2011). This parameterization gives adjustable parameters depending on the amount of finer particles with regard to coarser particles ($x = \phi_f/(\phi_f + \phi_c)$) and on parameters independently found for the two types of suspension:

$$\begin{cases} \phi_{*cf} = \phi_{*f}x^{1.34} + \phi_{*c}(1 - x)^{1.34} \\ \gamma_{cf} = \gamma_f x + \gamma_c(1 - x) \\ \xi_{cf} = \xi_f x + \xi_c(1 - x) \end{cases} \quad (3.15)$$

This parameterization is most suited for our purpose as we consider two populations of crystals: coarse phenocrysts with sphere-like shapes and fine microlites with needle-like shape. Ultimately, the relative viscosity and the apparent yield strength are calculated at each temperature increment according to the crystal volume fraction correspondingly obtained via MELTS.

3.3 Results

3.3.1 Description of the flow morphology

In proximal 2 km (see Figure 3.1d)), smooth, flat lava surfaces, ropy textures and multiple collapsed roofs reveals pahoehoe type lava emplaced as tube-fed flow. About 2 km from the vent, the lava advanced through a narrow passage between two hyaloclastite mounds (informally named ‘bottle neck’) and flows down a steep scarp (Figure 3.1d). This sharp increase in slope appears to have locally enhanced the lava velocity and caused the lava surface to stretch and break into a crumbly to blocky a’a-type flow. Below the scarp, no evidence of tubes was found but irregular blocks of tens of centimetre forming a clinkery texture typical of a’a type. Downstream of the bottleneck and the change in slope the flow velocity appears to have abruptly waned, partially causing the formation of pressure ridges and inflation features. About 800 m downstream of the bottleneck the bulk of the flow stops, forming a broad flow lobe from which a breakout yields the extrusion of a narrow flow tongue. Although the whole lava flow is interpreted as volume-limited (as observed by drained lava tubes at proximal reaches), the distal portion of the flow (the last 2 km) is interpreted as cooling limited flow due to undrained channel and distal breakout (Wilson and Head, 1994). A weakly visible, filled-channel facies with levees is only observed over a short flow length of about 20 m (profile 6, Figure 3.2). Consequently, the distal portion represents a cooling-limited flow system. Due to the tube-fed regime and the rather complex emplacement of the proximal to medial flow portions, rheological parameters from the morphology were only calculated using the distal area downstream of the bottleneck (Figure 3.2),

3.3.2 Viscosity estimate from the morphology

Geometric flow parameters and resulting lava flow viscosity and yield strength were determined for the distal part of the lava flow. A total of nine profiles were analyzed where flow width, height and length were measured (Figure 3.2, Table 3.2). Each profile is an average of ten individual measurements spaced one meter apart. The lava flow segment has a length of 2044.7 ± 0.8 m; its width varies from 124.7 m to 359.7 m with an average

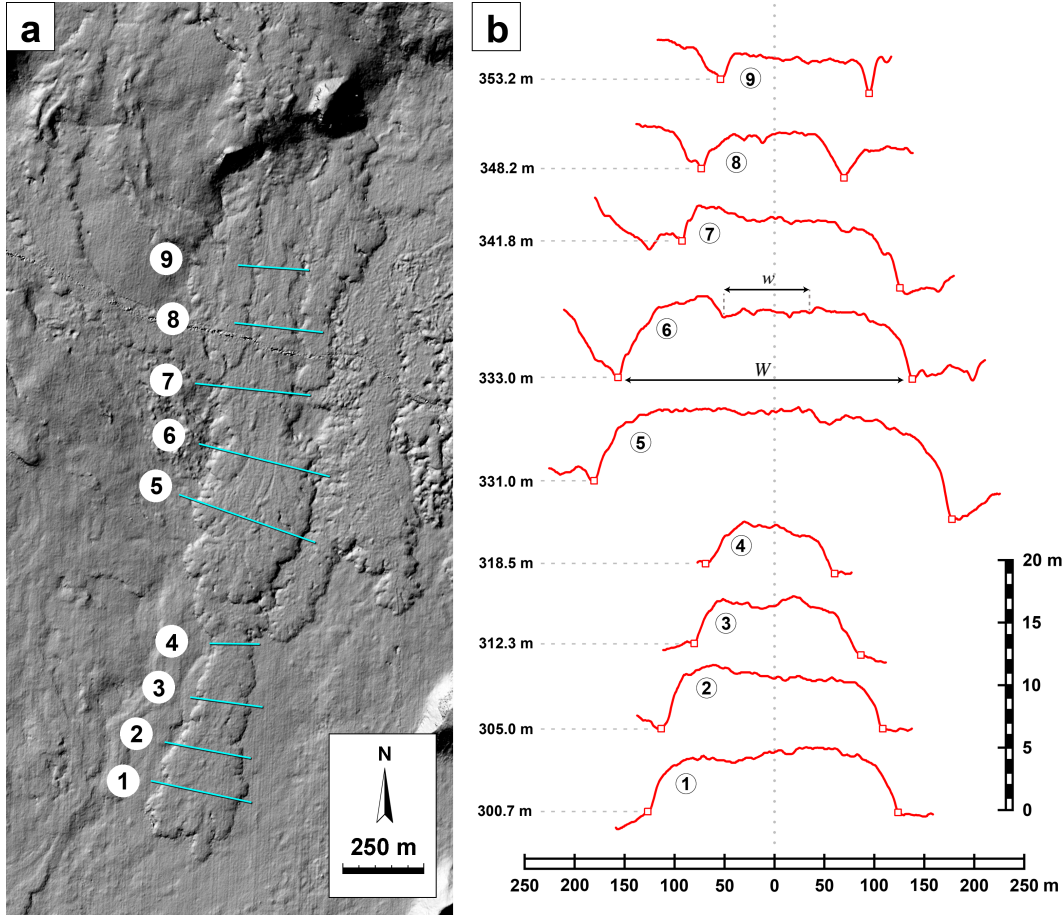


Figure 3.2: (a) Data Elevation Model of the distal section of lava flow with location of the profiles used to estimate the rheological parameter. (b) Topography cross-section of the profiles with vertical exaggeration. Numbers on the left side are the absolute elevation at the bottom of the profiles.

width of 225.6 ± 0.4 m and its height ranges from 2.1 m to 7.5 m with an average of 4.7 ± 0.3 m.

Propagation of even small errors in morphometric parameters measurements may cause a larger spread in the rheological properties derived with this remote analysis. In particular, the variation in flow height significantly affects the error analysis for viscosity and yield strength calculations, as it is factored by a power of 2 to 4. The topographic gradient was determined next to the lava flow where the underlying topography is exposed as well as on the flow surface where the pre-eruption topography is concealed by adjacent flows. The average slope is about 1.8° . Error analysis includes formal statistical errors for both morphometrical variations (i.e., in L , W , w , H , α) using repeated measurements and absolute instrumental parameters (i.e., density and resolutions of the digital terrain model and image data).

The estimated effusion rate is calculated at 20.5 ± 1.13 $\text{m}^3 \cdot \text{s}^{-1}$. The flow viscosity

Physical constants					
density [kg.m ⁻³]	ρ	2600 ± 100			
gravity [m.s ⁻²]	g	9.80665			
Grätz number [-]	G_z	300			
thermal conductivity [m ² .s ⁻¹]	κ	7.00E-07			
Average of all profiles		mean	error	% error	
W		225.6	0.4	0.18%	
L		2044.7	0.8	0.04%	
H		4.73	0.26	5.52%	
α		1.66	0.00	0.04%	
profile #6		mean	error	% error	
W		359.7	0.3	0.10%	
w		103.2	1.5	1.50%	
L		2044.7	0.8	0.04%	
H		6.50	0.33	5.10%	
α		1.20	0.00	0.10%	
Rheological parameters		mean	error	% error	
Q [m ³ s ⁻¹]		2.05E+01	1.13E+00	5.52%	Eq.3.3
$\eta_{flow,1}$ [Pa s]		2.86E+05	5.16E+04	18.01%	Eq.3.4
$\eta_{flow,2}$ [Pa s]		6.22E+05	1.43E+05	23.09%	Eq.3.5
$\eta_{flow,3}$ [Pa s]		7.90E+03	1.50E+03	15.24%	Eq.3.9
$\tau_{0,flow,1}$ [Pa]		3.49E+03	2.35E+02	6.74%	Eq.3.6
$\tau_{0,flow,2}$ [Pa]		4.83E+03	2.80E+02	5.81%	Eq.3.7
$\tau_{0,flow,3}$ [Pa]		2.80E+03	3.50E+02	12.59%	Eq.3.8

Table 3.2: Geometric flow parameters and resulting lava flow viscosity and yield strength.

obtained using Eq. 3.4 equals to within one order of magnitude the one obtained using Eq. 3.5 (on the order of 10^5 Pa.s). In contrast Eq. 3.9 provides a viscosity value some two orders of magnitude lower (3.49×10^3 Pa.s). The geometrical analysis thus provides a wide range of possible nominal viscosity estimates. However, whatever the equation considered, the apparent yield strength of the flow is estimated between 2.8 and 4.83×10^3 Pa and the errors remain between 5 and 13%.

3.3.3 Chemistry and Petrography

The bulk rock chemistry of the samples shows compositional homogeneity along the flow and is in agreement with the analyses of the Thjófahraun volcanic unit by Eason and Sinton (2009). The lava is basaltic in composition with 48 wt.% SiO₂, less than 2.5 wt.% alkali, and a Mg# of 0.63 (Table 3.3). Like most hot-spot related basaltic material, the total iron content is fairly high with 12 wt.% FeO_{tot}.

Petrographic analyses reveal no systematic variations in the volume fraction of vesicles and crystals in the samples collected along the flow (Table 3.3). Within a single sample, however, the vesicle volume fraction locally varied and the bubble shape could occasionally change from spherical to elongate/stretched bubbles suggesting strain localization and/or heterogeneity in volatile content and/or temperature. Although these

	L2D	L2B1	L2B2	L2G	L2A	Average	Stdev
SiO ₂	48.17	48.15	47.94	48.04	48.16	48.09	0.10
TiO ₂	1.75	1.74	1.74	1.73	1.75	1.74	0.01
Al ₂ O ₃	15.00	14.78	14.85	14.82	14.89	14.87	0.08
FeO _{tot}	12.03	12.17	12.18	12.10	12.07	12.11	0.06
MnO	0.20	0.21	0.21	0.21	0.21	0.21	0.00
MgO	8.72	8.92	9.15	9.06	8.72	8.92	0.20
CaO	11.63	11.55	11.45	11.55	11.69	11.57	0.09
Na ₂ O	2.11	2.10	2.11	2.12	2.13	2.11	0.01
K ₂ O	0.20	0.20	0.21	0.20	0.20	0.20	0.00
P ₂ O ₅	0.17	0.17	0.17	0.17	0.17	0.17	0.00
Total	100.00	100.00	100.00	100.00	100.00	100.00	
Mg #	0.62	0.63	0.63	0.63	0.62	0.63	
% Vesicles	20.07	12.67	16.18	12.90	15.99	15.56	
% Olivine	1.77	4.44	2.32	7.55	1.33	3.48	
% Plagioclase	7.92	4.62	2.89	2.99	1.58	4.00	

$$\text{Mg \#} = \text{Mg}100 / (\text{Mg} + \text{Fe})$$

Table 3.3: Normalized bulk rock geochemical composition and petrological characteristic of the samples. Oxide abundances are in wt.% and FeO_{tot} is the total Fe expressed as FeO.

local variations may result in a complex regime, we neglect their effects with respect to the rheological behavior of the lava flow as a whole during flow emplacement. The rock exhibits a glomeroporphyritic texture with clusters of euhedral olivine phenocrysts and some interlocking plagioclase surrounded by a microcrystalline groundmass (Figure 3.3). Vesicle diameters range from 50 μm to more than a few millimeters, and the phenocrysts can be up to 1 mm in length, sometimes occurring in clusters of up to 5 mm in diameter. Point counting reveals that all samples are comprised of, on average, 12 to 20 % vesicles and 3 to 10 % pre-eruptive phenocrysts (with lengths exceeding 200 μm). The remaining groundmass fraction, as detailed through back-scattered electron images (Figure 3.3), exhibits an intergranular texture in which olivine and pyroxene and at a later stage, oxides, fill the interstices of a framework formed by tabular plagioclase microlites of less than 200 μm (representing about 50 % of the groundmass). No interstitial glass could be identified. The microlites locally show a fluidal alignment along a flow direction and around the bubbles (Figure 3.3e). Representative chemical compositions of the crystals are presented in Table 3.4. The olivine phenocrysts have a homogeneous composition of 84 % forsterite. Thin rims of less than 20 μm , as well as olivine microlite in the groundmass, have lower forsterite contents (Fo₇₆). This more ferrous composition is associated with a lower temperature and late post eruption crystallization (in agreement with Eason and Sinton (2009)). The plagioclase (phenocrysts and microlites) is 70 to 80 % anorthitic and the pyroxene belongs mainly to the Ca-rich group (augite) with approximately 37 % wollastonite.

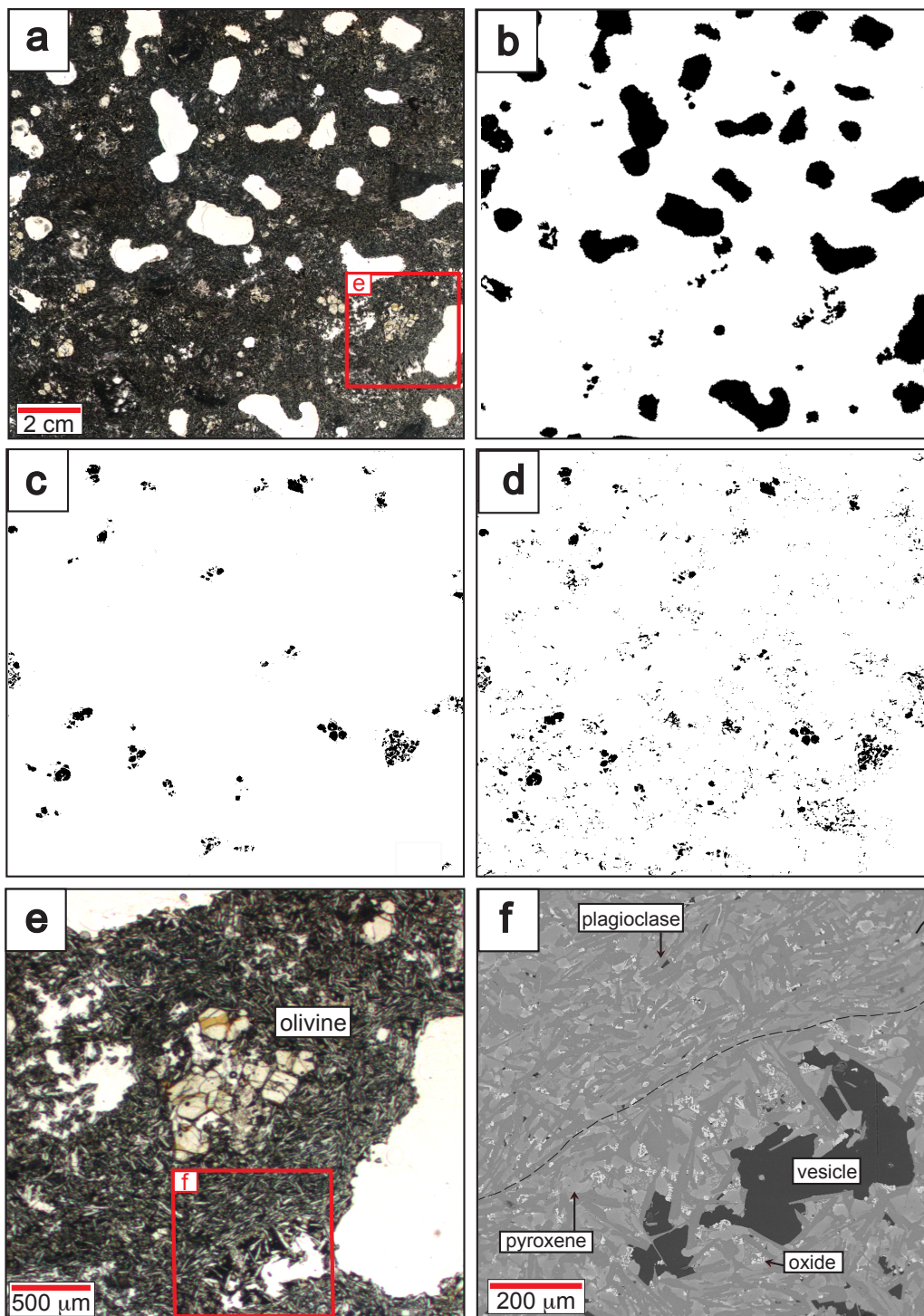


Figure 3.3: Petrographic analyses of the sample L2A. (a) Photograph in plane-polarized light; and associated binary images used to evaluate the vol.% of: (b) vesicles, (c) olivine phenocrysts and (d) all crystals larger than 200 μm . (e) Closer look at the thin section shows the petrographic assemblage and (f) back scattered electron analyses evidences the microcrystalline groundmass with pyroxene crystallized in between the plagioclase microlites and the oxides at last in the remaining space; the plagioclase microlite laths are aligned in a flow direction. In this example, plagioclase (in dark grey) represents 52 % of the total area of this picture.

	Olivine phenocryst	Olivine rim/groundmass	Plagioclase	Pyroxene
SiO ₂	40.12	38.92	50.61	50.31
Al ₂ O ₃	-	-	29.97	2.68
FeO	14.43	21.58	1.13	14.37
MgO	43.46	39.53	-	14.023
CaO	0.30	0.33	14.47	17.24
Na ₂ O	-	-	3.37	0.23
For ^a	84.3	76.6	-	-
An ^b	-	-	70.4	-
Wo ^c	-	-	-	36.9

^a Forsterite %= Mg100 / (Mg + Fe)

^b Anorthite %= Ca100 / (Ca + Na)

^c Wollastonite %= Ca100 / (Ca + Mg + Fe)

Table 3.4: Representative chemical compositions of the crystals.

3.3.4 Crystallization sequence

Optical observation and thermometry

The phenocrysts formed in the magma chamber, while the microlites crystallized during magma ascent, eruption and subsequent flow emplacement (e.g., Gill, 2010). Interpretation of the textural analyses suggest that, olivine is the first mineral to crystallize in the magma chamber, followed by plagioclase and that eruption has occurred at, or immediately after, the onset of plagioclase crystallization, as there are less than 1 % plagioclase phenocrysts within the sample. The groundmass (liquid prior to eruption) crystallizes quickly during magma ascent and lava flow emplacement. During magma ascent the drop of pressure within the magma permits nucleation of bubbles that enhances crystallization. Fast cooling of the lava in contact with the atmosphere and the Earth's surface generates abundant micro-crystallization in the groundmass, forming mainly plagioclase and small iron-rich olivine. Subsequently, the residual liquid crystallized as clinopyroxene and oxides. Considering equilibrium between the core of the phenocryst olivine and the bulk rock as a liquid, and assuming a pressure of 1 kbar, and presence of 0.4 wt.% H₂O in the magma chamber (Eason and Sinton, 2009), the temperature of the liquidus (onset of olivine) is estimated to be 1215 °C using the 'Olivine-liquid thermometer' from Putirka (2008).

Thermodynamic calculation

The thermodynamic calculator MELTS (Ghiorso and Sack, 1995) is used to describes the abundance of each crystalline and liquid phase during magma ascent, eruption and lava emplacement at every temperature (Figure 3.4). The starting chemical composition considered here is obtained by averaging the bulk-rock composition of the samples. In

the magma chamber, at 1 kbar, 0.4 %wt. H₂O and QFM-2 (Eason and Sinton, 2009), the appearance of olivine would occur at 1213 °C (consistent with the estimation from the thermobarometer obtained from olivine composition Putirka, 2008), followed by plagioclase at 1180 °C. The eruptive temperature is suggested to be 1175 ± 5 °C, based on the extent of crystallization required to produce the phenocryst content observed in the rock. The ascent of the magma is modeled by decreasing pressure from 1 kbar to 1 bar while maintaining a constant temperature of 1175 °C and oxygen fugacity at QFM-2. Due to the pressure drop, MELTS computes a loss of water from 0.4 to 0.06 wt.% and a large increase in crystallinity from 7 to 19 vol.%. The late-stage crystallization is calculated at 1 bar until the solidus. The onset of Ca-rich pyroxene nucleation occurs at 1170 °C, and oxides crystallize at 1108 °C from the remaining liquid. Complete crystallization is achieved at 1095 °C.

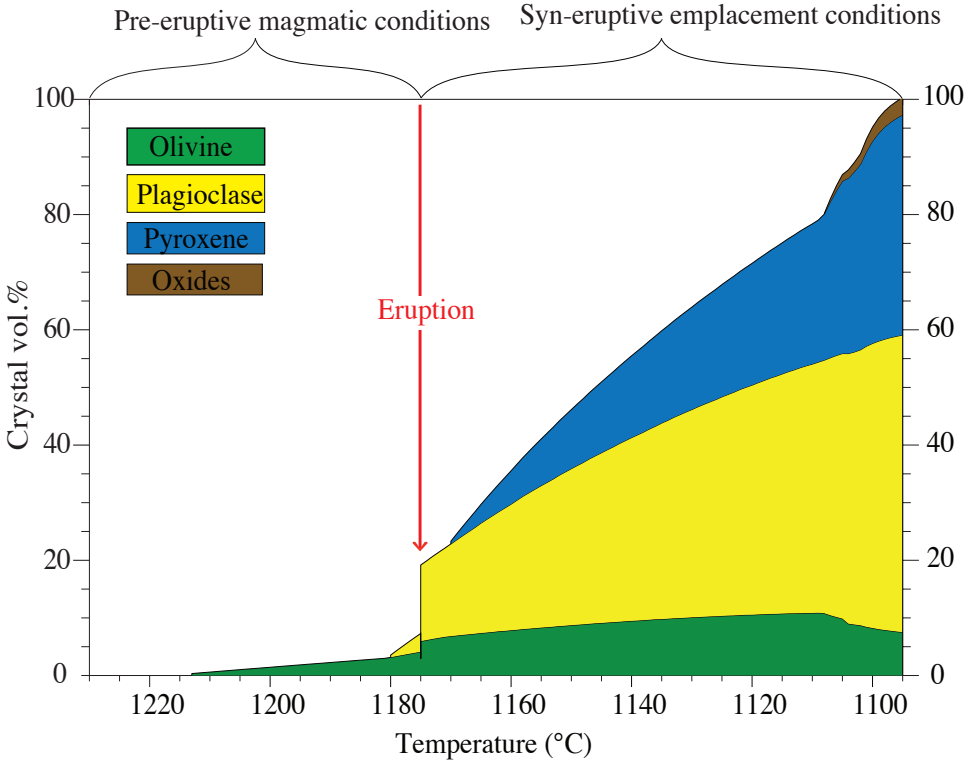


Figure 3.4: Crystallization sequence as a function of temperature calculated with MELTS from the magma chamber conditions (1 kbar, 0.4 wt.% H₂O, QFM-2) through isothermal eruption and emplacement at the surface (1 bar, QFM-2).

3.3.5 Transient viscosity model of the crystallizing lava flow

The transient apparent viscosity of the erupted material is calculated using Eq. 3.1, based on a value of relative viscosity estimated using three models: Shaw (1969), Krieger and Dougherty (1959) and Costa (via Cimarelli et al., 2011). For the Krieger-Dougherty, the relative viscosity was calculated using fitting parameters from Mueller et al. (2010) (Table 3.5). For the calculation using the Costa equation (Eq. 3.13, 3.14, 3.15), the relative proportions of phenocrysts and microlites (x) were calculated at every temperature step; the relative viscosity was calculated using the fitting parameters from Cimarelli et al. (2011) for strain rates of 10^{-6} , 10^{-4} and 1 s^{-1} (Table 3.5). [Note: that the parameters at 10^{-6} s^{-1} are extrapolated using the strain-rate dependency offered by Caricchi et al. (2007)].

	Mueller et al., 2010		Cimarelli et al., 2011					
	A	B	at 10^{-6} s^{-1}		at 10^{-4} s^{-1}		at 1 s^{-1}	
			A	B	A	B	A	B
ϕ_m	0.641	0.343	0.61	0.26	0.54	0.36	0.61	0.44
δ			11.54	9.65	11.48	7.5	2.79	4.54
γ			1.46	3.35	1.52	5.5	1.6	8.55
ϕ_c			0.53	0.25	0.62	0.26	0.67	0.28
ξ			3.8E-05	2.2E-04	5.0E-04	2.0E-04	1.0E-03	1.0E-03

Table 3.5: Fitting parameters for sphere-like (A) and needle-like (B) particles independent on strain rate (Mueller et al., 2010) and for diverse strain-rate (Cimarelli et al., 2011).

The calculated apparent viscosity obtained through all three models is presented as a function of temperature in Figure 3.5. The viscosity of the molten bulk rock and of the residual liquid (η_{melt}) calculated at each temperature (using the GRD model) are also shown; these can be used to distinguish between the effect of the compositional change in the residual melt and the effect of crystals. [Note: the viscosity of the molten bulk rock was experimentally measured on a melted sample using the concentric cylinder method (Dingwell, 1986). At super-liquidus conditions, the apparent viscosity is similar to the viscosity of the remelted whole rock.] At the onset of olivine crystallization, the apparent viscosity becomes progressively higher than the pure liquid's viscosity. At the eruption, the large increase in plagioclase and the water loss due to magma ascent of the lava result in a sharp increase in viscosity. Continuous increase of the apparent viscosity then accompanies microlite nucleation and growth during cooling at the Earth's surface. Approaching a critical crystal content, that depend on the model, the viscosity increase abruptly. Unlike the Shaw and Krieger-Dougherty models which compute an infinite viscosity increases when approaching the maximum packing values and fails to compute viscosity for crystal content exceeding the maximum packing at lower temperatures, the model provided by Costa enables us to quantify the remaining rheological evolution of

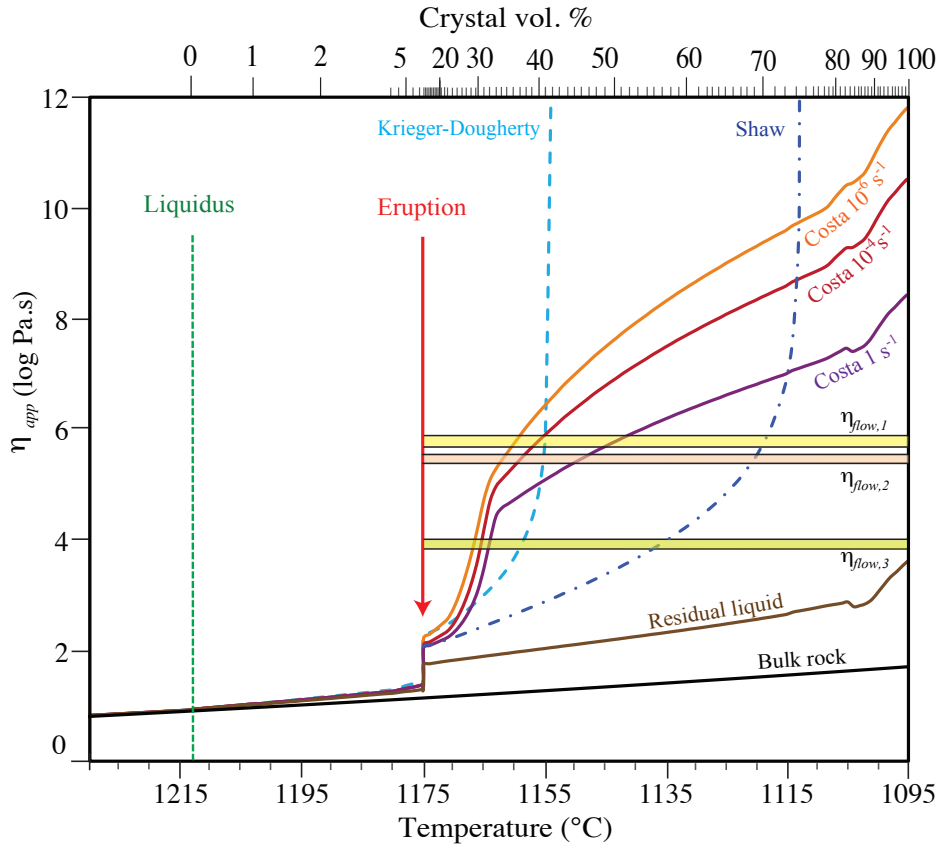


Figure 3.5: Apparent viscosity of the crystallizing lava as a function of temperature and corresponding crystallinity modeled with MELTS. The apparent viscosity is calculated according to three models: Shaw (1969) using Eq. 3.11 that considers all crystals are spheres (dashed dark blue line); Krieger and Dougherty (1959) using Eq. 3.12 that considers the sum of the effect of the mafic minerals modeled as spheres and of plagioclase modeled as needles (light blue dashed line); and Costa using Eq. 3.13, 3.14, 3.15 considering the parameterization of Cimarelli et al. (2011) for a mixture of mafic minerals (modeled as spheres) and plagioclase (modeled as needles) for strain rates of 10^{-6} , 10^{-4} and 1 s^{-1} (orange, red and purple line respectively). The liquid's viscosity of the bulk-rock (black line) and the residual liquid viscosity (brown line) are also represented. The apparent viscosity of the flow obtained from the geometric parameters, $\eta_{flow,1}$, $\eta_{flow,2}$ and $\eta_{flow,3}$ calculated using Eq. 3.4, Eq. 3.5 and Eq. 3.9 respectively, are represented independently of the crystallization sequence (colored areas correspond to the associated uncertainties of the values).

the crystallizing lava that is controlled by the solid fraction.

The yield strength calculated from the crystal content ($\tau(\phi)$) is represented in Figure 3.6 as a function of temperature and corresponding crystallinity. The yield strength of the lava increases during cooling due to the increasing crystal content. Depending on the model, the mixture may start to exhibit yield strength as soon as crystals form (Gay et al., 1969; Ryerson et al., 1988; Dragoni, 1989; Mueller et al., 2010), whereas other models

consider a minimum crystal content before onset of the yield strength (Zhou et al., 1995; Castruccio et al., 2010). A sharp increase of the yield strength is first observed due to the onset of plagioclase crystallization and then due to further crystallization after eruption, and eventually, in some cases it is extrapolated to infinite when crystallinity reaches the maximum packing (Gay et al., 1969; Zhou et al., 1995; Mueller et al., 2010). In contrast, the experimental fit of Ryerson et al. (1988) and Castruccio et al. (2010) do not consider a maximum packing value and seem to tend toward a maximum value of the order of $10^{3.5}$ to 10^5 Pa. As pure liquids have no yield strength, the dependence of the yield strength with temperature is then only due to the crystallization sequence.

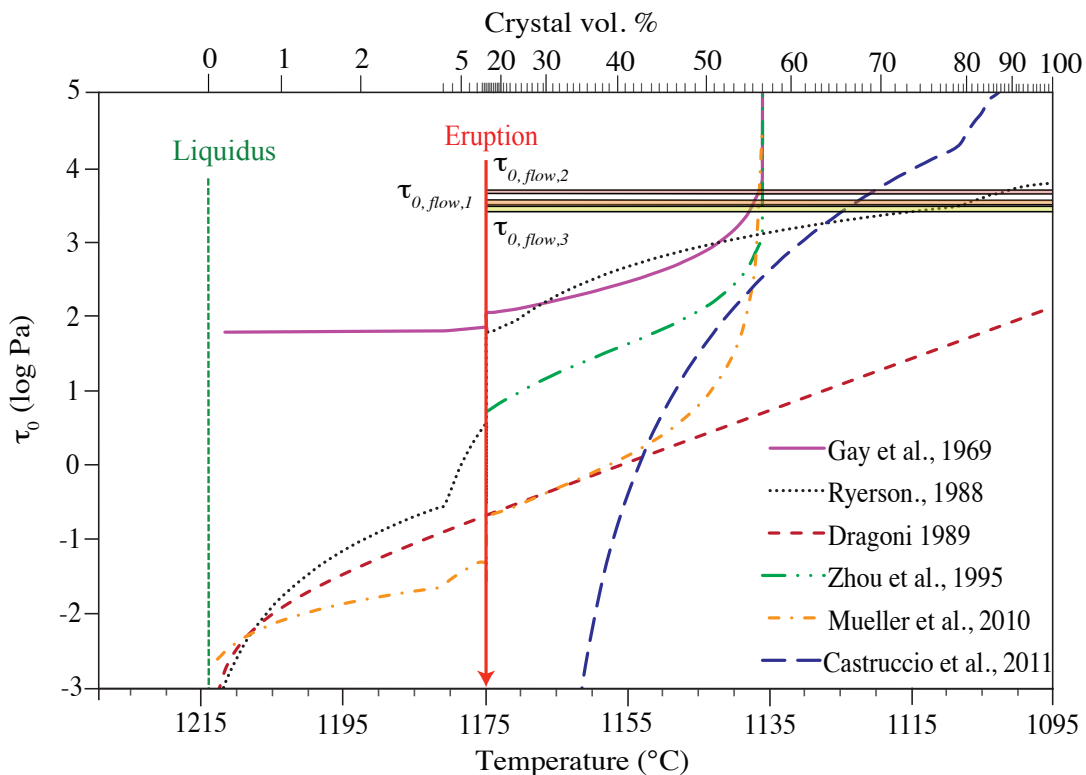


Figure 3.6: Apparent yield strength of the crystallizing lava as a function of the temperature and corresponding crystallinity modeled by MELTS. The lava’s yield strength is calculated as a function of crystal content using the various models available in the literature (see Table 3.1). As an attempt to account for the effect of bi-modal particles, the calculated yield strength was calculated as the product of the yield strength due to the mafic crystals (modeled as spheres-like shape) and plagioclase (modeled as needle-like shape): $\tau_0 = \tau_{0(\text{mafic})}\tau_{0(\text{plagioclase})}$ with $\phi_m = 0.64$ and $\phi_c = 0.3$ for mafic minerals and $\phi_m = 0.34$ and $\phi_c = 0.09$ for plagioclase. The apparent yield strength obtained from the geometric parameters of the lava flow, $\eta_{0,flow,1}$, $\eta_{0,flow,2}$ and $\eta_{0,flow,3}$ using Eq. 3.6, 3.7 and 3.8, respectively are represented independently of the crystallization sequence (colored areas correspond to the associated uncertainties of the values).

3.4 Discussion

Here, we use rheological models and thermodynamic calculation to describe the full path of the lava rheology during cooling upon eruption until its full solidification. MELTS is a convenient tool to describe the crystallization sequence of lava, providing quantities and chemical compositions of all phases in equilibrium at a given temperature. The solution provided by MELTS is, however, not unique in that a given mineral assemblage (with specific ratios of minerals) can be achieved through crystallization of a somewhat wide range of parental magmas using diverse initial conditions. Moreover, MELTS is intransigent to disequilibrium crystallization kinetics typical of volcanic environments. Owing to our ability at sampling the studied lava flow, our model revolves around well-constrained geochemical conditions; yet, it certainly does not fully account for crystallization disequilibrium associated with rapid cooling. Crystallization is considered in equilibrium, but the crystal shape for microlites was considered as elongate, which typifies rapid cooling. Future improvement will require the coupling of cooling rate and crystal growth (rate, shape and size) with the rheology in order to measure the change of viscosity as a function of the distance from the source vent and as a function of vertical location within the flow. In that sense, various cooling rates and differences in the degree of crystallization between the base or surface and the core of the flow must be accounted for. Thus, the assumption of thermodynamic equilibrium between all the crystal phases and the liquid, and at each temperature step, is a simplification employed here in a volcanic environment. Furthermore, studies have reported evidence for melt fractionation in basaltic flows as well as intra-flow melt segregation due to vesiculation (Kuno, 1965; Costa et al., 2006). Considering that the studied flow is relatively small (both in length and volume), the assumption of equilibrium crystallization appears to be reasonable but fractional crystallization should be evaluated in future studies interested in large magmatic bodies or lava flows that show well-defined cumulate textures (Komatiite-type lavas, Kinzler and Grove, 1985).

Many studies have previously attempted to estimate the apparent viscosity of crystallizing lavas at sub-liquidus temperatures (e.g., Shaw, 1969; Ryerson et al., 1988; Pinkerton and Stevenson, 1992; Harris and Allen, 2008). These studies employed earlier empirical models describing the viscosity of liquids (Shaw, 1972; Bottinga and Weill, 1972, e.g.) as well as the Einstein-Roscoe equation to determine the effect of crystals (Shaw, 1969). Although these combined methods provide reasonable approximations at low crystal contents (< 20 vol.%) associated with near-liquidus temperatures (e.g., Ishibashi and Sato, 2007; Vona et al., 2011), they fail to map the complete rheological evolution of crystallizing lava until solidification. The comparative model analysis introduced in the present study illustrates how each of the three main models (Shaw, Krieger-Dougherty, and Costa),

given a set of parameters (pressure, temperature, chemistry, crystal content and shape, etc.) can provide contrasting apparent viscosity estimates (see Figure 3.5). When trying to constrain the rheological evolution of lava undergoing complete crystallization, the model of Costa (using the fitting parameters for a bi-disperse mixture from Cimarelli et al., 2011) provides, to date, the most complete viscosity description, taking into consideration any crystal fraction, varied crystal shapes, and most importantly, strain-rate. The shallowing of the viscosity-crystallinity relationship above the maximum packing (as described by Costa’s model) suggests that in heavily loaded suspensions, deformation is strongly controlled by the crystalline network. Strain may induce crystal alignment and more particles can be accommodated. In our sample, the maximum packing is reached at a microlite content of ~ 34 vol.%, when ~ 43 vol.% of crystallization has occurred, but we observed the alignment of plagioclase which, alone, amount to approximately 50 vol.%, a fact which emphasizes the need to consider flow at degrees of crystallization beyond the maximum packing. The natural follow-up improvement ought to be the consideration of bubbles, but no comprehensive rheological laws allow undertaking such a task to date.

In the context of a cooling and crystallizing basaltic flow, the yield strength increases until it reaches the value corresponding to the time-scale for which the flow appears to be stagnant. Thus the yield strength of a lava flow, is an “apparent value” that is defined by its final morphological dimension. The attempts that have been previously established to model the relationships between shear strength and crystallinity reflect the time-scale of the experimental procedures; that is in many studies, the slower strain rate approximates 10^{-6} s^{-1} , which in some models agree on a yield strength around 10^4 Pa – a range similar to the values obtained from flow morphology characteristics (Figure 3.6).

Interestingly, the estimated single-value of viscosity ($\eta_{\text{flow},1}$ and $\eta_{\text{flow},2}$) from the flow morphology dimensions, and the estimated yield strength ($\tau_{0,\text{flow}}$), overlap with the values estimate from the crystallization sequence near the maximum packing; suggesting that the flow has recorded in its morphology the highest viscosity and yield strength when it is becoming seemingly stagnant. We wish to emphasize that in the case of polycrystalline magmatic suspensions, the crystals having the highest aspect ratio control the maximum packing: that is, higher aspect ratios lead to lower maximum packing.

3.4.1 Implications for the rheological mapping of extra-terrestrial lava flows

The potential complexity of rheological/petrological evolution during lava flow emplacement is evident from the above. The geometrical approximation of singular viscosity and yield strength values (as described by Jeffreys’ and Hulme’s equations) cannot accurately constrain the detail of the rheological evolution of a flow. Although it may

help to distinguish between extremes (e.g., mafic vs felsic flows), the non-unique rheological/petrological path evolution may severely prevent our ability to distinguish subtler between lava flow compositions.

The difficulties may be even more significant when considering apparent high-viscosity flows. Protracted extrusion of andesitic lava domes at Volcán de Colima, Mexico, for example, have been constrained to flow at viscosities of 10^{10} - 10^{12} Pa·s, a viscosity range which, according to Walker (1973) and Pinkerton and Wilson's (1994) scheme, would suggest a rhyolitic origin. In the latter, the sequence of crystallization may not be the decisive factor influencing the rheological evolution of the flow, but rather its general cooling and degassing efficiencies (e.g., Hess et al., 2005). As lava degasses, its viscosity increases and in turn slows down the rate of structural relaxation of the lava, forced to undergo the glass transition. Such lava will thus be subject to a very different rheological evolution, which may not be so intensely dependent on crystallization.

In the present study, the basaltic, iron-rich, Icelandic lava flow is considered analogous to many Martian lava flows. One may therefore assume a somewhat similar crystallization sequence and, thus, viscosity evolution during emplacement (although consideration of contrasting cooling rate, gravitational field, atmospheric pressure and degassing efficiency may temperate such a correlation to be made). The range of viscosity observed on Mars may therefore likely reflect differences in bulk rock composition associated together with different cooling history and crystallization sequence. High viscosity values of 10^{5-6} Pa·s calculated for some Martian lava flows may be best explained by basaltic compositions with high crystal content (50 vol.%). Such lava may be expected to behave like an a'a type flow, similar to the distal portion of the studied Icelandic flow. In the case of some Martian lava flows with very low inferred viscosity values of 10^2 Pa·s, high effusion rates or extremely low silica and content may favor the extreme long run-out distances of such lava, as previously proposed by Vaucher et al. (2009a). Such low viscosities may also be explained by rapid crystallization of high aspect ratio, needle-like crystals, as observed in Komatiitic lava flows forming spinifex textures that would have low maximum packing value and hence freeze the lava flow at high temperature corresponding to low apparent viscosity. Spinifex textures have recently been suggested for Martian lavas, based on crystallization experiments (Bost et al., 2012). Lava flows with seemingly low viscosities, associated with recent ultramafic volcanism in Central Elysium Planitia (e.g., Stockstill-Cahill et al., 2008), may preserve such textures. The need for optical description of petrographic textures imaged by rovers during landing missions is apparent. In this context, the interpretation of Martian flows should combine morphological analysis with the mineralogical observation from high-resolution visible and near-infrared spectroscopy. Using such multidisciplinary approach may significantly reduce uncertainties on lava flow

compositions and rheological behavior during flow emplacement.

3.5 Conclusion

The rheology (viscosity, yield strength) of a lava flow of the Western Volcanic Zone in Iceland has been estimated from its morphology via the methodology widely used in planetary sciences. In order to evaluate the physical meaning of such estimates, we have constrained the transient rheology of the erupted lava considering the observed crystallization sequence, further modeled through MELTS based on chemical composition, crystal content and shape, and published geothermobarometric data. The viscosity is shown to depend strongly on the crystallization sequence. The results demonstrate that the flow viscosity is inevitably transient and increases by more than 6 orders of magnitude during emplacement from the vent to the flow front. The lava viscosity quickly becomes non-Newtonian as the groundmass crystallizes. Using combined thermodynamic and empirical models, which consider both, the composition and crystals' morphologies is an important step towards improved viscosity estimates. We show that rheological properties obtained from the morphology of the flow are distinct from the lava behavior at the eruption onset and during most of its emplacement, corresponding rather to transient values occurring near flow cessation.

The present comparative approach should be applied to a wide range of compositions (andesitic, dacitic) in order to verify the use of such a method in planetary sciences. Complementary analyses (e.g., radar, direct sampling) should be employed to constrain potential geochemical differences. We recommend that thermodynamic calculations and rheological models be deployed in tandem to better understand the complex behavior of extra-terrestrial lava flows. In the case of Mars, where chemical and mineralogical compositions are becoming relatively well constraint through the ages (Baratoux et al., 2011), such a combined morphological/rheological/petrological solution may prove invaluable to the surface description of the planet's geodynamics.

CHAPTER

4

Viscous flow behavior of
tholeiitic and alkaline Fe-rich
Martian Basalts

Abstract

The chemical compositions of Martian basalts are enriched in iron with respect to terrestrial basalts. Their rheology is poorly known and liquids of this chemical composition have not been experimentally investigated or incorporated in models of terrestrial melt viscosity. Here, we determine the viscosity of five synthetic silicate liquids having compositions representative of the diversity of Martian volcanic rocks over time including primary Martian mantle melts and alkali basalts. The concentric cylinder method has been employed between 1500 °C and the respective liquidus temperatures of these liquids, and the viscosity near the glass transition has been derived from calorimetric measurements of the glass transition. Although some glass heterogeneity limits the accuracy of the data near the glass transition, it was nevertheless possible to determine the parameters of the non-Arrhenian temperature-dependence of viscosity over the entire temperature range (1500 °C to the glass transition temperature). At superliquidus conditions, the Martian basalt viscosities are as low as those of the Fe-Ti-rich lunar basalts, similar to the lowest viscosities recorded for terrestrial ferrobasalts, and 0.5 to 1 orders of magnitude lower than terrestrial tholeiitic basalts. Comparison with empirical models reveals that Giordano et al. (2008) offers the best approximation, whereas the model proposed by Hui and Zhang (2007) is inappropriate for the compositions considered. The slightly lower viscosities exhibited by the melts that are thought to represent primary melts in the Amazonian period (< 3.0 Ga) versus those of the Hesperian period (age <3.7 Ga), is not deemed sufficient to lead to viscosity variations large enough to produce an overall shift of Martian lava flow morphologies over time. Rather, the details of the crystallization sequence (and in particular the ability of some of these magmas to form spinifex texture) is proposed to be a dominant effect on the viscosity during Martian lava flow emplace-

ment and may explain the lower range of viscosities (10^2 - 10^4 Pa·s) inferred from lava flow morphology for the Amazonian period flows. In contrast, differences between the rheological behaviour of tholeiitic vs trachy-basalts are significant enough to affect their emplacement as intrusive bodies or as effusive lava flows. The upper range of viscosities (10^6 - 10^8 Pa·s) suggested from lava flow morphology may indicate the occurrence of alkali basalt rather than basaltic-andesite, or andesite flows.

4.1 Introduction

Both *in-situ* and remote sensing-based chemical and mineralogical analyses of fresh igneous rocks on Mars indicate the wide occurrence of Fe-rich tholeiitic basalts as well as Fe-rich mildly alkali- and trachy-basalts (13 to 22 wt.% of total iron content expressed as FeO: FeO_{tot}) (e.g., Binder, 1976; Gellert et al., 2004; McSween, 2004; McSween et al., 2006a; Boynton et al., 2007; Bost et al., 2012; Grott et al., 2013, Figure 4.1). The chemical compositions of the Martian basalts are significantly shifted toward Fe-rich compositions in comparison with terrestrial basalts (characterized by an average of FeO_{tot} abundance of ~12 wt. %). In contrast to Mars, Fe-rich magmas on Earth are rare, being associated with the ultramafic Archean lavas such as Komatiites (Arndt et al., 1977); originating from a peculiar Fe-rich mantle source (Francis et al., 1999; Gibson et al., 2000) and/or hot spot related volcanism (Fisk et al., 1982; Stout et al., 1994; Norman and Garcia, 1999; Eason and Sinton, 2009); or resulting from melt immiscibility and phase separation at a late stage of the crystallization sequence as observed at the Skaergaard intrusion (e.g., Philpotts, 1979; Veksler, 2009). While the physical properties of very Fe-rich melts have limited applications on Earth, they appear to be of primary importance to understand the dynamics of volcanic materials on Mars. Recent Martian lava flows (less than 50 Ma Hartmann et al., 1999; Vaucher et al., 2009b; Hauber et al., 2011) suggest the possibility of magma migrating through a thick lithosphere of more than 150-200 km. Morphological characteristics of volcanic edifices with gentle slopes as well as long lava flows indicate effusive activity of very fluid lavas (e.g., Hiesinger et al., 2007; Greeley, 2005; Baratoux et al., 2009; Vaucher et al., 2009b) and layers of pyroclastic deposits hint at the existence of explosive activity (Hynek et al., 2003).

Viscosity is the main physical parameter affecting the evolution of molten bodies from their formation, during their ascent and emplacement in the subsurface as intrusions (Michaut, 2011; Michaut and Baratoux, 2013, submitted) or at the surface as volcanic flows (e.g., Pinkerton and Stevenson, 1992; Dingwell, 1996). It controls the speed of magma ascent through the crust, the ease of crystal and bubble growth, and therefore defines the type of eruption. The lower the viscosity, the faster the transport of the melt, (or the lower the driving stresses) will be during both ascent and surface emplacement. Further, for the same initial concentration of volatiles, inefficiently degassed highly viscous bubbly magma experiences more explosive behavior whereas efficiently degassed low viscosity magmas erupt effusively. The lava flow viscosity values inferred from morphologic analysis on Mars range from 10² to 10⁸ Pa·s. These are attributed to ultrabasic, basaltic or more evolved compositions (Grott et al., 2013, and references therein). In fact, the occurrence of very fluid lavas on Mars represents a possible source of confusion for the recognition of channels associated with effusive flows against fluvial channels associated

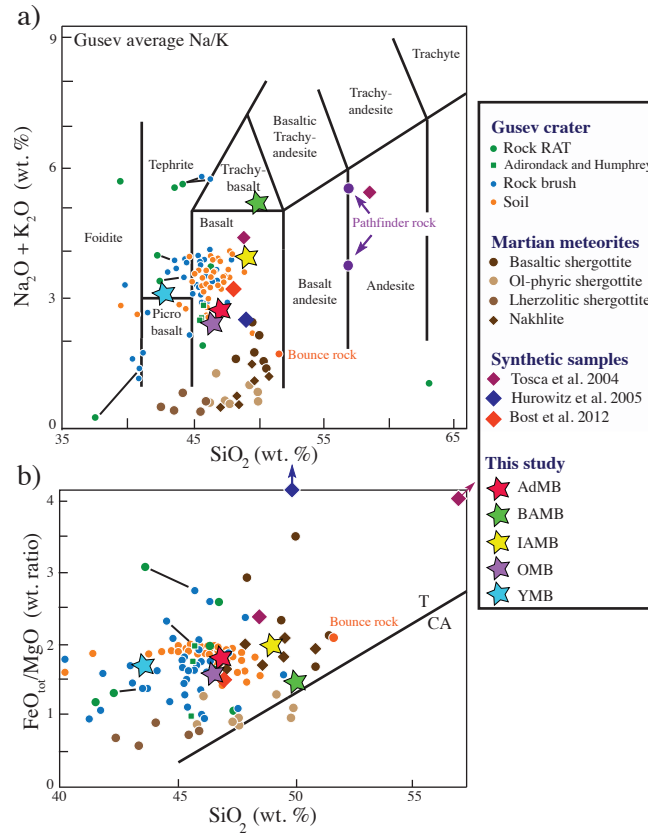


Figure 4.1: Composition of the synthetic samples of this study (stars) plotted in the total alkalis ($\text{Na}_2\text{O} + \text{K}_2\text{O}$) and $\text{FeO}_{\text{tot}}/\text{MgO}$ ratio vs. silica content (in wt. %) diagrams (modified figure from McSween et al., 2009; Bost et al., 2012). The data includes the *in-situ* analyzed rocks at Gusev craters (compositions of brushed rock and after abrasion, RAT, are connected by tie-lines), Pathfinder rocks and Martian meteorites. The Bounce rock is the only sample of basaltic origin that was analyzed in the Meridiani Planum by the Opportunity rover (Rieder et al., 2004; Zipfel et al., 2004). Also shown for comparison are the synthetic Pathfinder rock and soil from Tosca et al. (2004), the synthetic Los Angeles sample from Hurowitz et al. (2005) as well as the synthetic sample from Bost et al. (2012).

with liquid water flows. For instance, outflow channels have been principally associated to catastrophic water release (the dominant hypothesis) but an alternative possibility would be the effusion of low viscosity magmas (Leverington, 2011, and references therein). The interpretation of landforms within one of the youngest regions of Mars, Central Elysium Planitia, has also been the focus of controversial interpretations (Jaeger et al., 2007, 2010; Page, 2008, 2010). Such ambiguities are a strong motivation for constraining the range of possible viscosities of Martian lavas. Low apparent viscosities are qualitatively compatible with the known compositions of Martian basaltic rocks containing a relatively low Si and high Fe content (Greeley, 2005; Baratoux et al., 2009; Hauber et al., 2009; Vaucher et al., 2009b; Chevrel et al., 2012). However, the viscosity of such Fe-rich Martian lavas has

never been directly measured. The closest Fe-rich compositions that have been measured are some synthetic lunar lavas that have a lower viscosity than terrestrial basaltes (e.g., Murase and McBirney, 1970; Cukierman et al., 1972). Here we measure the viscous behavior of Fe-rich Martian lavas and test whether currently available empirical models relating the chemical composition to the melt viscosity (Shaw, 1972; Giordano et al., 2008; Hui and Zhang, 2007) are well-adapted to the specificity and diversity of the Martian lavas compositions (tholeiitic and alkaline). The dry melt viscosity is investigated over a very wide temperature range: at superliquidus temperatures as well as at low temperatures (near the glass transition) in order to describe well their non-Arrhenian behavior (Hess and Dingwell, 1996; Russell and Giordano, 2005; Hui and Zhang, 2007; Giordano et al., 2008). The experimental viscosity results are then compared to terrestrial and lunar Fe-rich melts and the increase of viscosity caused by crystallization is then modeled and discussed as a function of the crystallization sequence at surface conditions. This study provides a framework to interpret the diversity of morphologies of effusive flows on Mars' surface, to address which empirical models may be used to calculate the viscosity of silicate melts that may be used in turn in models of intrusion emplacement or lava flow emplacement.

4.2 Samples

The five samples investigated in this study are Fe-rich basalts chosen to be representative of the known diversity of Martian basalts (Figure 4.1, Table 4.1). Three samples have a chemical composition directly given by *in-situ* analysis of Hesperian volcanic rocks at Gusev crater. In detail, selected compositions correspond to the chemical analyses from the Alpha Particle X-Ray Spectrometer of Adirondack, Irvine and Backstay rocks after grinding several millimeters into the rock (Gellert et al., 2004, 2006; McSween et al., 2006b; Ming et al., 2008).

The Adirondack basalt (referred as AdMB) is a dark, fine-grained, vesicular rock interpreted as lava. It is an olivine-rich primitive basalt with high Mg and low K (similar to a tholeiitic basalt). It is enriched in Fe (19.5 wt. % FeO_{tot}) and depleted in Al (10.9 wt. % Al_2O_3) compared to common terrestrial tholeiitic basalt and is the dominant type on the Gusev plains. The Irvine and Backstay rocks (referred respectively as IAMB and BAMB respectively) are the first alkali basalts recognized on Mars and were found at the Columbia Hills inside the Gusev Crater. They are interpreted as lavas or possibly dike rocks. Backstay is enriched in Al and alkaline ($\text{Na}_2\text{O} + \text{K}_2\text{O} = 5$ wt.%) and depleted in Fe, Mn, and Cr compared to the Adirondack basalts covering the floor of Gusev crater. The Irvine class rocks are geochemically similar to Backstay except that they are depleted in

	Tholeiitic basalt	Mildly- alkaline basalt	Trachy-basalt	Primary mantle melt	Primary mantle melt
	Adirondack class rock	Irvine	Backstay	Hesperian basalt	Amazonian basalt
	AdMB	IAMB	BAMB	OMB	YMB
SiO ₂	47.01	49.09	50.22	46.72	43.38
TiO ₂	0.59	1.10	0.94	0.56	0.68
Al ₂ O ₃	10.86	8.58	13.46	10.61	10.28
FeO _{tot}	19.43	20.36	13.87	18.99	21.19
MnO	0.42	0.38	0.24	0.11	0.14
MgO	10.14	9.82	8.43	11.39	11.73
CaO	8.09	5.99	6.12	8.41	8.20
Na ₂ O	2.66	3.10	4.21	2.25	3.03
K ₂ O	0.15	0.62	1.09	0.17	0.25
P ₂ O ₅	0.65	0.97	1.41	0.79	1.13

Table 4.1: Chemical composition of the investigated Martian synthetic melts.

Al, P, and alkaline elements ($\text{Na}_2\text{O}+\text{K}_2\text{O}= 3 \text{ wt.}\%$), and enriched in Fe with an average 19.7 wt. % FeO_{tot} compared to 13.2 wt. % FeO_{tot} in Backstay (McSween et al., 2006a; Ming et al., 2008). The two other samples are compositions based on variations of the partial melting conditions of Mars’ mantle as a function of time (Baratoux et al., 2011) Considering a homogeneous composition of the mantle, Baratoux et al. (2011) have found variations of Si and Fe in the major volcanic provinces that reflect the secular evolution of the conditions of partial melting. In detail, a decrease of SiO₂ from 46.6 to 43.2 wt. % and increase of FeO_{tot} from 18.4 wt. % to 20.7 wt. %, associated with an increase in Na₂O+K₂O from 2.42 to 3.28 wt. % and a slight increase in P₂O₅ from 0.79 to 1.13 wt. % would have occurred during the Hesperian (3.7-3.2 Ga) to Amazonian ages (> 3.2 Ga) (Table 4.1). In particular, the Fe-enrichment of young volcanic surfaces with respect to older terrains is supported by Gamma Ray Spectrometer data. Therefore, two additional compositions have been calculated to represent primary melts of the primitive mantle of Mars (Dreibus and Wänke, 1985) during the Hesperian and the Amazonian. These compositions neglect possible variations of source and extraction from distinct geochemical reservoirs that have been previously depleted (e.g. during the magma ocean scenario – Elkins-Tanton et al., 2005, or related to volcanism). Nevertheless, these compositions offer a framework to study the rheological consequences of these systematics affecting the primary melt compositions. The Hesperian basalt (hereafter OMB) is calculated considering a pressure of 13 kbars and a potential temperature of the mantle of 1400 °C and its composition is very similar to AdMB. The younger Amazonian basalt type (hereafter, YMB) is produced at 17 kbars and for a potential temperature of the mantle

of 1350 °C. YMB is thus poorer in Si and richer in Fe relatively to all other studied compositions.

4.3 Experimental methods

4.3.1 Melt preparation

The synthesized samples for this study are Cl, S and Cr-free to prevent volatility and early crystallization of Cr-rich oxides. The samples were prepared by mixing 100 g of dried (120 °C) reagent grade oxide and carbonate powders of SiO₂, Al₂O₃, MgO, CaCO₃, Fe₂O₃, TiO₂, MnO, Na₂CO₃, K₂CO₃ and NaH₂PO₄. The powder mixes were milled together in an large agate mortar in acetone for at least 30 min and then fused in a platinum crucible for two hours in air at 1500 °C. The melts were then poured on a copper plate, crushed and melted a second time. Those melts were then poured directly into a thick-walled cylindrical platinum crucible that was transferred to a furnace equipped with a rotational viscometer and stirred for five hours using a Pt₈₀Rh₂₀ spindle at 1500 °C. The crucibles and spindle had been previously doped with Fe to minimize the propensity of Fe loss into the crucible wall.

4.3.2 Superliquidus viscometry under controlled oxygen fugacity

The viscosity at superliquidus conditions was measured via the concentric cylinder method (Shaw, 1969; Dingwell, 1986) at 1 atm and under varying ambient oxygen fugacity (in air and down to two orders of magnitudes bellow the QFM buffer; QFM-2). The setting consists of a cylindrical crucible containing the molten material that is placed in the hot zone of a vertical furnace equipped with a gas-tight alumina muffle tube and a CO₂-CO gas-mixing line (Dingwell and Virgo, 1987). A cylindrical spindle is inserted into the melt and is driven at constant speed by a viscometer head (Brookfield® DVIII+) that records the torque (see detailed method in Annex 1). For each composition, the viscosity was first measured in air from 1500°C to 1375 °C by 25 °C increments of decreasing temperature. The effect of the melt redox-state on viscosity was then investigated at isothermal condition (1385 or 1395 °C) by decreasing the oxygen fugacity inside the muffle tube via changing the CO₂-CO ratio of the gas flow. At the lowest oxygen fugacity, usually corresponding to QFM-2, the temperature dependence of viscosity was also measured between 1500 °C and 1375 °C. The viscosity, temperature and oxygen fugacity were recorded every second, which allows precise tracking of the melt response. The viscosity values were taken after 1 hour of isothermal equilibrium for measurements performed at constant f_{O_2} and after a minimum of 24 h for each f_{O_2} change to ensure a melt fully

equilibrated with the new fO_2 . At the end of the experiment, the highest temperature data-point in air was reoccupied to check a possible instrumental drift or chemical changes of the melt. The melts were sampled at high temperature and at every fO_2 step (each sampling batch is labelled between -S0 to -S8). The quenching method, called the “dip-quench” method, consists in inserting and removing an alumina rod (with a diameter of 3 mm) into the liquid forming a melt droplet on the rod tip that is then fast quenched into a water bucket. The process lasts less than 15 s and the melt cooling rate is then estimated to be ~ 100 °C/s. This fast cooling causes the glass to fragment into powder and tens of small chips (< 10 mg) that were used for further analyses (chemical analyses, redox state titration, calorimetric measurements).

4.3.3 Chemical composition and redox state

One or two chips per sampling batch resulting from the “dip quench” were mounted as polished sections for petrographic and chemical analysis carried out with a CAMECA SX 100 Electron MicroProbe Analyser (EMPA) and Back Scattered Electron images (BSE) were obtained for each analyzed chip. About 30 mg of powder was used for redox state determination that was performed using potassium dichromate titration. This procedure is a destructive technique that digests the material and measures the amount of Fe^{2+} by a redox reaction (Giuli et al., 2011, see detailed method in Annex 1). In combination with EMPA analysis, the FeO/FeO_{tot} ratio was calculated for each glass.

4.3.4 Low temperature viscosity at the glass transition temperature

In order to avoid crystallization in these Fe-rich samples, the viscosity at sub-liquidus conditions was determined from quenched glassy samples, that were briefly heated into the metastable supercooled liquid state. The excursions into the metastable state required by the parallel plate or beam bending techniques cannot be used because of rapid crystallization of Fe-rich samples (Karamanov and Pelino, 2001; Karamanov et al., 2002; Bouhifd et al., 2004). An alternative method is to evaluate the viscous relaxation time that can be fixed to the glass transition at a known quenching/heating rate. The temperature of the glass transition is defined as the limiting fictive temperature (T_f') that is the temperature at which the structure of the liquid is frozen in during quenching; T_f' is therefore a function of the quench rate of the liquid: the faster the quench rate, the higher T_f' . The glass transition temperature range can be determined with calorimetric measurements because the sample releases some excess in heat capacity when it is heated from the glass field into the liquid field (endothermal peak of the heat capacity vs. temperature / time

curve; (e.g. Moynihan et al., 1974; Scherer, 1984). About 27 mg of glass (usually 4 to 5 chips) per sample batch were used for calorimetry measurements differential scanning calorimetry using the 404 Pegasus apparatus from NETZSCH® Gerätebau. All samples received the same treatment; they were initially heated at 20 K/min, and then cooled and subsequently re-heated at various cooling rates of 25, 20, 15 and 10 K/min. The curves were calibrated against a baseline and the heat capacity was calculated with a sapphire standard of 27.7 mg (see detailed method in Annex 1). For all samples, T_f' was obtained from the curves obtained on the re-heated sample having known quenching rates using the method described by Moynihan (1995). The corresponding viscosity is then calculated via the linear relationship between the applied cooling rate and the viscosity (Gottsmann et al., 2002) at T_f' :

$$\log\eta(atT_f') = K - \log|q| \quad (4.1)$$

where η is the viscosity(Pa·s), K is a constant that equals to 11.04 ± 0.37 as determined by (Chevrel et al., 2012) and q is the cooling rate in $K.s^{-1}$.

4.4 Results: compositions and redox state

4.4.1 Chemical compositions

The chemical composition of each sampling batch was analyzed in order to check the stability of the element concentration during the viscosity measurements. A minimum of 20 chemical analyses data across a single chip were performed to evaluate the chemical homogeneity of the glasses (Table 4.7 in supplementary material). For the samples equilibrated in air, the results indicate that the samples are chemically homogeneous within the error of the measurements. These compositions are slightly enriched in Fe and depleted in Si compared to the starting composition (dark red symbols in Figure 4.2). Only one sample, IAMB-S1, was recognized to contain some small crystals. Micro-oxide crystals with a length of $<10 \mu\text{m}$ are unequally distributed and represent less than 0.5 % vol. and therefore their effect is neglected for viscosity measurements (Lejeune and Richet, 1995). An attempt to measure their composition is given in Table 4.8 in the supplementary material. Smaller crystals are found around these oxides and have a dendritic morphology, typical of rapid growth during quenching process.

For the samples equilibrated under reduced conditions, no oxide crystal was found but the chemical compositions of the glasses are more variable (Figure 4.2; Table 4.7 in supplementary material). Although each individual sample is homogeneous, the AdMB samples having different redox states have different compositions. AdMB-S3, -S4 and -S8 are enriched in SiO_2 (48.3 - 49.1 wt.%) and depleted in FeO_{tot} (16.9 -18.6 wt.%)

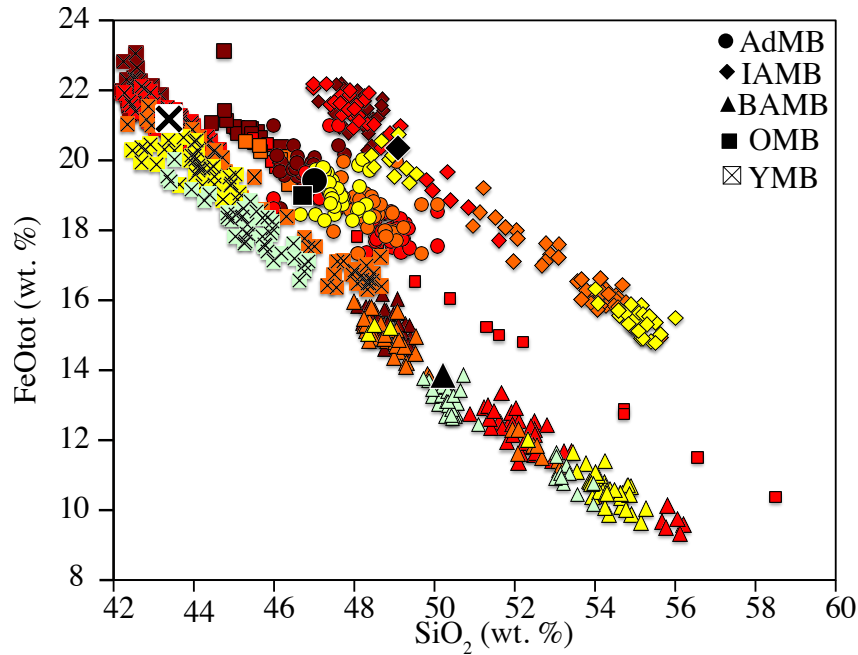


Figure 4.2: Microprobe chemical composition analyses of each investigated samples. The symbol shape differs for each composition as indicated in the legend. The black symbols are the starting chemical composition (according to the weighted reagent powders). The color code indicates the change in fO_2 conditions: the more oxidized (equilibrated in air) is in dark red, then in order toward more reduced: red, orange, yellow, and whitish.

compared to the others that have a composition close to the starting material and within the standard deviation of the analyses ($SiO_2 = 46 - 47.6$ wt.% and $FeO = 18.6 - 20.9$ wt.%). There is no clear trend correlating the variation of chemical composition and quenching conditions. The BAMB and IAMB samples show large variations between all the samples, and a single chip may exhibit a distinct internal heterogeneity. For most of these samples, two distinguishable compositions could be identified (they are given as LSi for liquid enriched in Si and LFe for liquid enriched in Fe in Table 4.7). Although for most of the samples, this compositional variation was not observed with BSE images, some filaments of distinct compositions were observed within IAMB-S4 (Figure 4.3). The OMB and YMB samples quenched under different conditions have also variable chemical compositions. In sample OMB-S2, two distinct compositions, LSi, and LFe, could be identified. The sample YMB-S3, have the larger internal heterogeneity, with SiO_2 varying from 42.3 to up to 49.4 wt.% and FeO_{tot} from 21.5 down to 15.9 wt.%. For most of the samples, although chemical heterogeneity could be detected, the use of BSE images does not permit the identification of sub-micron emulsion or a gradient of elemental diffusion. Transmission electron microscopy technique may be required to collect further evidence of any such micro or sub-micron scale features.

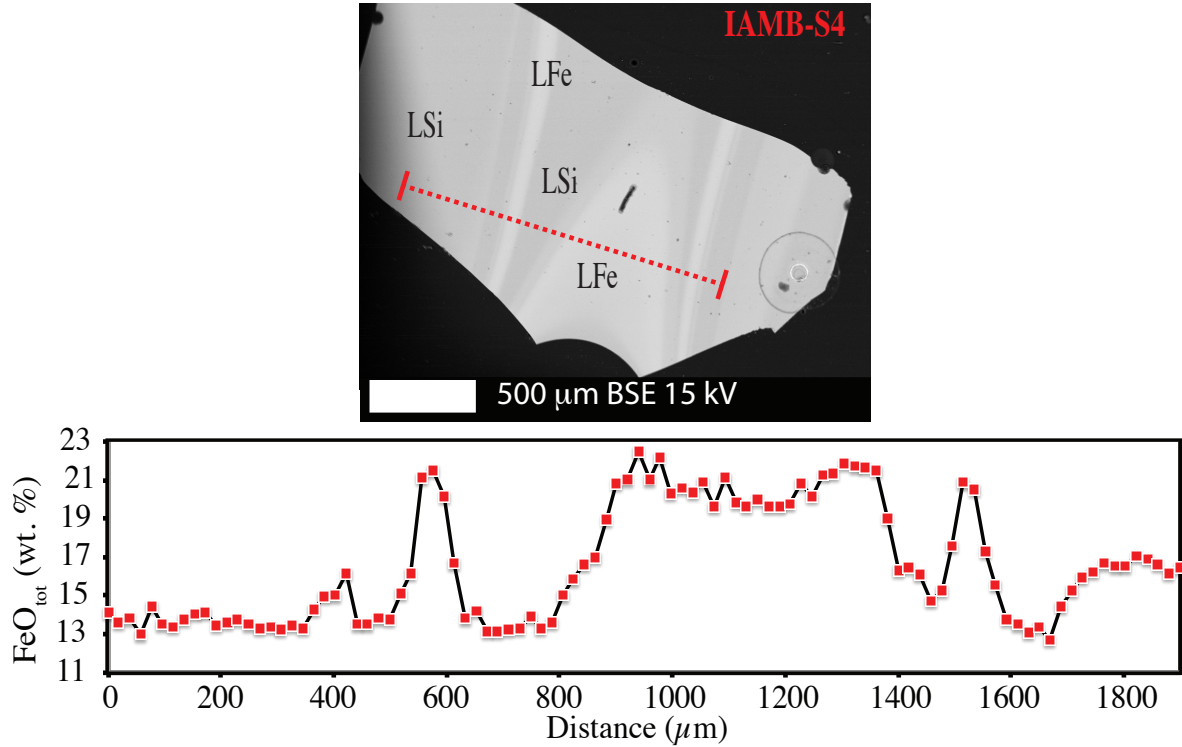


Figure 4.3: Back Scattered Electron images of IAMB-S4 glass chip obtained by 'dip quench' from 1395°C and low f_{O_2} showing the separation of the melt into two composition (LFe and LSi). The grey intensity is scaled on the presence of heavy elements, the brighter the higher FeO_{tot} and the lower SiO_2 .

4.4.2 Iron Redox-state

Two titrations were performed for each sample and the difference were less than 0.8 wt.% of FeO. The $\text{FeO}/\text{FeO}_{\text{tot}}$ was then calculated with the average FeO values of the two titrations and the average FeO_{tot} from EMPA measurement for each sample (Figure 4.4). Taking into account the variation of the titration and of EMPA measurements, the error on the redox state is calculated for each sample. The largest error is calculated for the reduced samples, where the compositional variation is greatest. The observed chemical heterogeneity within a single sample raises significant concerns over the quality of the redox-state calculations. These results suggest that the sampling technique must be improved further to reduce the error bars on the redox-state.

4.4.3 Evidence of immiscibility at high-temperature or phase separation during slow quenching?

Whether the chemical heterogeneity is due to liquid immiscibility at high-temperature or to the quenching process is a major issue (Veksler et al., 2007, 2008; Philpotts, 2008).

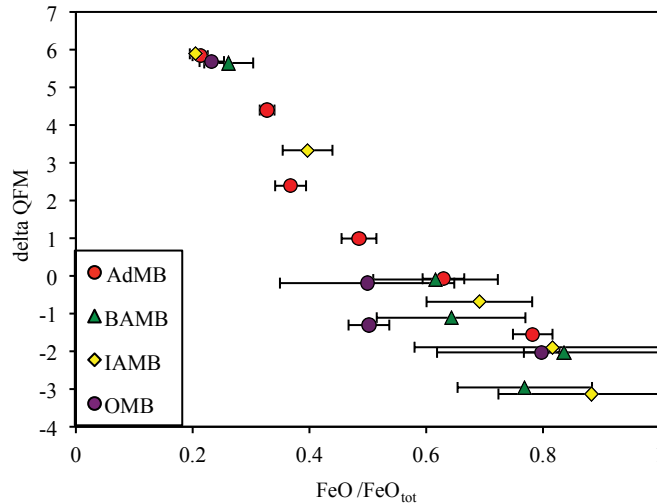


Figure 4.4: Redox state ($\text{FeO}/\text{FeO}_{\text{tot}}$) of the melts as a function of the ambient oxygen fugacity express as delta QFM.

Unlike in static experiments (melt droplet suspended to Pt-loop wire), liquid separation may happen in dynamic experiments (Veksler et al., 2007, 2008). The stirring of the melt during viscosity measurement by the spindle is fast, achieving a speed of 40 rotations per minute. Phase separation may then be enhanced by this stirring as in a centrifuge. As obtained in previous studies, the composition of the mafic conjugate liquid (LFe) is close to the bulk starting material, and the felsic member of the pair (LSi) is far way enriched in Si, that is consistent with immiscible melts. However, we did not conduct any experiment that could prove the presence of two liquids at high temperature, and according to previous studies, it seems unlikely that immiscible liquids were present during the viscosity measurement because immiscibility has never been reported at such high temperatures apart from pure FeO-SiO₂ binary systems (Roedder, 1978; Philpotts, 2008). Moreover, during the viscosity measurement, the presence of two immiscible liquids would cause a strain-rate dependant viscosity as in the case of suspended deformable bubbles, however this was not observed.

A phase separation during quenching is more likely to have happened. An attempt to quench these melts was first made by pouring the melt (equilibrated in air at 1500 °C) onto a copper plate and pressing it together with another copper plate. The resulting piece of glass was 3 mm thick and had near parallel surfaces. Chemical analyses were carried out along a vertical profile within the sample; this revealed a variation in chemical composition extending from outer quenched surfaces to the glass interior. The inner core was enriched in Fe while the surfaces were Si-rich. No other significant elemental variations were noted. Such variations were also observed in Wilson et al. (2012), and were attributed to a quenching rate, which was too slow to permit formation of a ho-

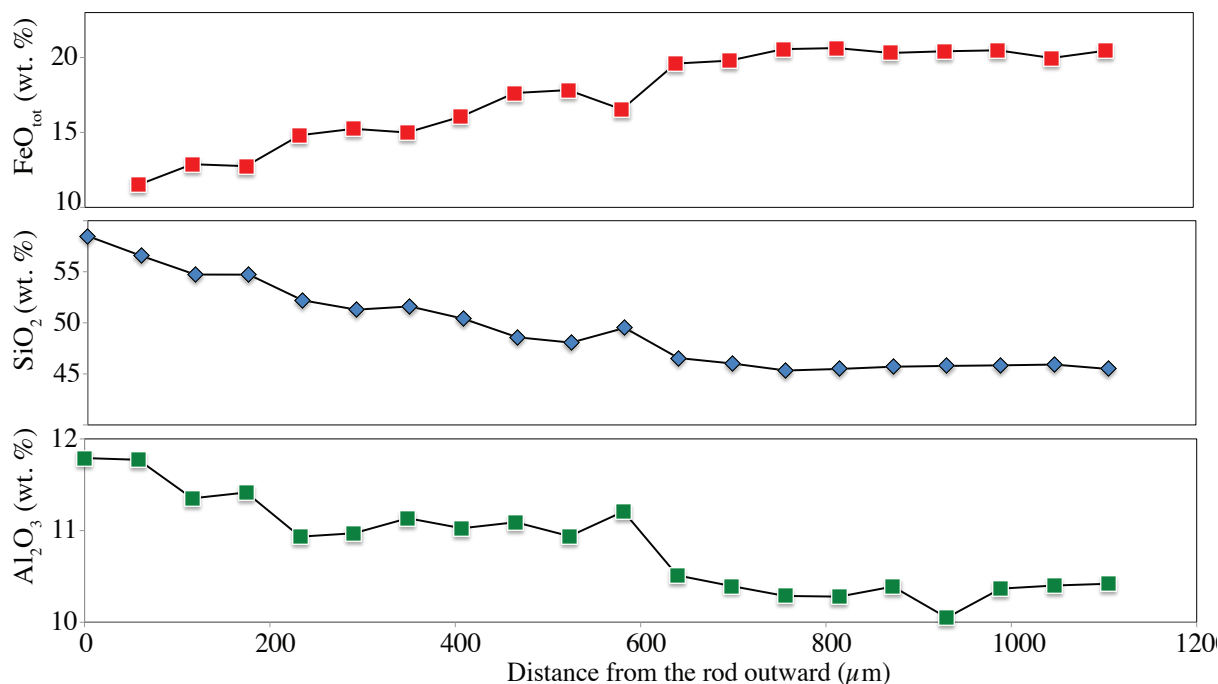


Figure 4.5: Chemical profile taken from the rod outward across the OMB-S2 glass obtained by 'dip quench'.

mogeneous glass. This chemical profile is a clear indicator of elemental migration, and eventually melts separation during quenching. In order to achieve a faster quench rate, avoiding such chemical variation, and also to be able to quench reduced samples, the "dip quench" technique was favored and always applied. However, even by using this technique, as noted before the produced glasses tend to be heterogeneous (internally or across the sample series). For the oxidized sample, dendritic crystals could grow during quenching but for the reduced samples, phase separation seems favored. Moreover, it was not possible to maintain a reduced environment during the quenching process; the reduced melts are quenched in oxidized environment (air). Even if this process is fast, estimated at $\sim 100 \text{ }^\circ\text{C/s}$ (from 1400 to $20 \text{ }^\circ\text{C}$ in ~ 15 sec), the small withdrawn droplet may have sufficient time to oxidize, favoring the migration and redistribution of the elements. An indicator that elements can migrate during the quenching was observed by the chemical analyses carried out on small chips that were preserved sticking to the sampling alumina rod, along a profile from the rod outward (Figure 4.5). On these transects the amount of Fe decreases and Si increases toward the spindle, accompanied by Al content slightly increasing by $1.5 \text{ wt.}\%$ (within the first $600 \text{ }\mu\text{m}$). The chemical profiles across the filaments observed by BSE reveal a gradient of diffusion in contrast to a clear limit between two immiscible melts. In conclusion, it seems likely that the chemical variations observed in the glasses are due to phase separation during quenching. It is well known that the basaltic compositions could be bad glass formers, and this impedes efforts to pro-

duce homogeneous amorphous materials. The high Fe content of the melts in this study enhances this behavior. It is obvious that the “dip quench” procedure is questionable as a method for synthesis of homogeneous Fe-rich glasses; in particular for reduced melts. More experiments should be carried out to confirm the melt immiscibility. Static experiment using Martian basaltic compositions should be first undertaken and then dynamic experiments using a centrifuge at high temperature and under reduced condition should be carried out. The sampling technique used here may be improved by permitting faster quenching and/or under sustained reducing conditions (Cukierman et al., 1973).

4.5 Results: melt viscosity and comparison with models

4.5.1 Viscosity in the superliquidus regime

The temperature dependence of viscosity measured in air and under low oxygen fugacity (near QFM-2) is presented in Table 4.2. In the investigated high temperature range, the melts have viscosities between -0.6 to 0.4 log Pa·s; the trachy-basalt, BAMB, is an exception to this, with a viscosity 0.5 log Pa·s higher than the others, attributed to higher Si and lower Fe content. Within the high temperature viscosity range, the temperature dependence of viscosity can be approximated by an Arrhenian relationship Shaw (1972):

$$\ln \eta = A_{Arr} + \frac{E^*}{RT} \quad (4.2)$$

where A_{Arr} and E^* (kJ/mol) are the pre-exponential term and the activation energy of viscous flow, respectively and R the gas constant. For all compositions, the activation energy is calculated to be between 121 and 209 kJ/mol (Table 4.3). The effect of redox-state on viscosity was investigated at a fixed temperature under successive reducing oxygen fugacity until a minimum value is reached at approximately $\text{FeO}/\text{FeO}_{\text{tot}} = 0.6$ (Table 4.4 and Figure 4.6). The maximum drop in viscosity is 0.18 log Pa·s for IAMB. Further reduction ($\text{FeO}/\text{FeO}_{\text{tot}} > 0.6$) induces a slight but systematic increase in viscosity of less than 0.05 log Pa·s that may be attributed to the loss of Fe into the crucible wall (forming an alloy with the platinum) or to the formation of metallic Fe nano-droplets. Therefore, the experiments were always stopped when the torque started increasing. Investigation of temperature dependence of viscosity at reduced condition reveals that the activation energy is similar for oxidized and reduced melts ($\pm 10 - 20$ kJ/mol). The viscosity under reduced conditions was not measured for YMB; but it can be confidently assumed not to exceed 0.2 log Pa·s under superliquidus conditions.

	Air			Reduced		
	T (°C)	log η (Pa s)	error	T (°C)	log η (Pa s)	error
AdMB	1483	-0.10	0.01	1385	0.17	0.01
	1458	-0.03	0.01	629	11.42	0.37
	1434	0.04	0.01	628	11.52	0.37
	1409	0.12	0.01	625	11.64	0.37
	1385	0.21	0.01	620	11.82	0.37
	1360	0.30	0.01			
	1336	0.39	0.01			
	647	11.42	0.37			
BAMB	1482	0.36	0.01	1395	0.56	0.01
	1457	0.44	0.01	1370	0.65	0.01
	1432	0.53	0.01	1346	0.75	0.01
	1407	0.62	0.01	1321	0.85	0.01
	1383	0.71	0.01	1296	0.95	0.01
	1358	0.82	0.01	1271	1.06	0.01
	1333	0.92	0.01	1247	1.18	0.01
	1308	1.03	0.01	1222	1.30	0.01
	1284	1.14	0.01	654	11.42	0.37
	674	11.42	0.37	657	11.52	0.37
				656	11.64	0.37
				653	11.82	0.37
	IAMB	1483	-0.07	0.01	1395	0.14
1458		0.00	0.01	1358	0.22	0.01
1434		0.08	0.01	1334	0.30	0.01
1409		0.16	0.01	632	11.42	0.37
1385		0.24	0.01	625	11.52	0.37
1360		0.33	0.01	623	11.64	0.37
1336		0.42	0.01	619	11.82	0.37
632		11.51	0.37			
OMB	1494	-0.31	0.01	1494	-0.34	0.01
	1469	-0.25	0.01	1469	-0.28	0.01
	1445	-0.19	0.01	1445	-0.22	0.01
	1420	-0.11	0.01	1420	-0.17	0.01
	1395	-0.04	0.01	1395	-0.11	0.01
	650	11.51	0.37	1370	-0.02	0.01
				638	11.42	0.37
				636	11.52	0.37
				631	11.64	0.37
				624	11.82	0.37
YMB	1492.96	-0.38	0.01	1395	-0.20	0.05
	1468.32	-0.32	0.01	1519	-0.41	0.13
	1443.69	-0.25	0.01	1494	-0.45	0.06
	1419.05	-0.17	0.01	1469	-0.32	0.09
	1394.42	-0.10	0.01	1445	-0.27	0.06
	1369.78	-0.02	0.01	1420	-0.23	0.06
	1492.96	-0.38	0.01	1395	-0.12	0.06
	624.85	11.51	0.37	1494	-0.32	0.07
				1445	-0.33	0.04
				1395	-0.16	0.04
				631	11.42	0.37
				626	11.52	0.37
				624	11.64	0.37
				620	11.82	0.37

Table 4.2: The viscosity of all investigated melts at 1 atm in air and at under reduced oxygen fugacity. The errors on the viscosity measurements at superliquidus conditions are estimated to be ± 0.01 log Pa·s, except for the YMB melt measurements that showed a noisy torque reading. The errors on the viscosity near the glass transition are estimated to be ± 0.37 log Pa·s.

	$A_{\text{Arr}}^{\text{HT}}$	E^{HT} (kJ/mol)	$A_{\text{Arr}}^{\text{LT}}$	E^{LT} (kJ/mol)
AdMB-S2	-12.68	182	-	-
AdMB-S6	-	-	-62.40	666
BAMB-S0	-13.55	209	-	-
BAMB-S1	-13.42	204	-82.11	820
IAMB-S1	-12.45	179	-	-
IAMB-S4	-11.62	164	-35.27	462
OMB-S1	-11.01	151	-	-
OMB-S4	-10.30	140	-32.53	446
YMB-S1	-11.93	162	-	-
YMB-S5	-9.11	121	-48.38	561

Table 4.3: Arrhenian fitting parameters for the viscosity data within the single super liquidus regime (at high temperature, HT) and near the glass transition (low temperature ranges, LT).

Sample	Temperature (°C)	$\log(fO_2)$	\log QFM	FeO/FeO _{tot}	$\log \eta$ (Pa s)	Duration (h)
AdMB-S2	1385	-0.63	5.84	0.21	0.21	39
AdMB-S3	1385	-2.08	4.40	0.33	0.15	120
AdMB-S4	1385	-4.08	2.39	0.37	0.14	70
AdMB-S5	1385	-5.48	0.99	0.48	0.12	96
AdMB-S6	1385	-6.55	-0.07	0.63	0.09	48
AdMB-S8	1385	-8.02	-1.55	0.78	0.17	96
BAMB-S0	1495	-0.74	5.65	0.26	0.67	-
BAMB-S1	1395	-6.48	-0.09	0.62	0.56	92
BAMB-S2	1395	-7.49	-1.11	0.64	0.56	38
BAMB-S3	1395	-8.41	-2.03	0.84	0.55	66
BAMB-S4	1395	-9.34	-2.96	0.77	0.58	51
IAMB-S1	1395	-0.61	5.89	0.21	0.32	24
IAMB-S2	1395	-3.16	3.33	0.40	0.22	46
IAMB-S3	1395	-7.18	-0.69	0.69	0.16	48
IAMB-S4	1395	-8.39	-1.89	0.82	0.14	46
IAMB-S5	1395	-9.63	-3.13	0.88	0.17	40
OMB-S1	1395	-0.70	5.68	0.23	-0.04	38
OMB-S2	1395	-6.58	-0.19	0.50	-0.09	41
OMB-S3	1395	-7.69	-1.30	0.50	-0.13	47
OMB-S4	1395	-8.41	-2.03	0.80	-0.09	39
YMB-S1	1395	-0.78	5.61	-	-0.23	24
YMB-S2	1395	-3.34	3.05	-	-0.16	44
YMB-S3	1395	-6.60	-0.21	-	-0.21	44
YMB-S4	1395	-7.63	-1.24	-	-0.16	45
YMB-S5	1395	-8.41	-2.03	-	-0.20	42

Table 4.4: The viscosity at super liquidus regime of the investigated melts at various ambient fO_2 . The fO_2 was measured by B-type sensors around the melt and it is different than the fO_2 inside the melt. The redox state of the melt is given by the FeO/FeO_{tot} ratio that is measured from oxido-reduction reaction done on the glass samples.

The comparison of our measurements with the empirical models of Shaw (1972); Hui and Zhang (2007); Giordano et al. (2008, here after GRD) is done to assess which of these models are most appropriate to model Martian compositions. The Arrhenian model of Shaw that, derived from basaltic compositions, yields results differing from experimental data with a root mean square error (RMSE) of 0.18 log unit for oxidized and 0.15 log unit for reduced melts. The GRD model, based on non-Arrhenian behavior and including a wider range of composition (from basaltic to rhyolite melts) differ from experimental data

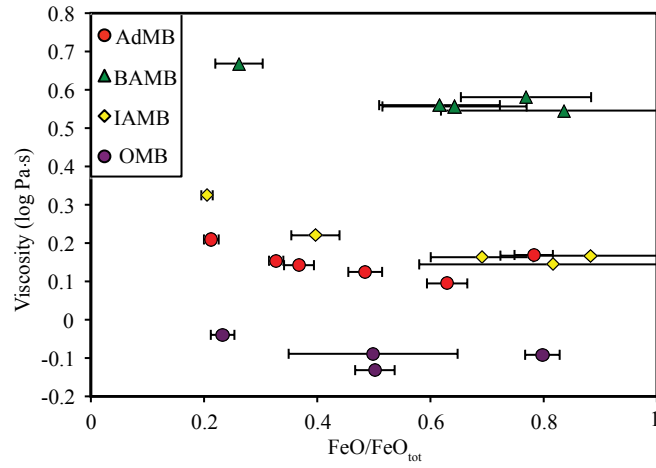


Figure 4.6: The viscosity at superliquidus regime of the investigated melts as a function of their redox state expressed as $\text{FeO}/\text{FeO}_{\text{tot}}$.

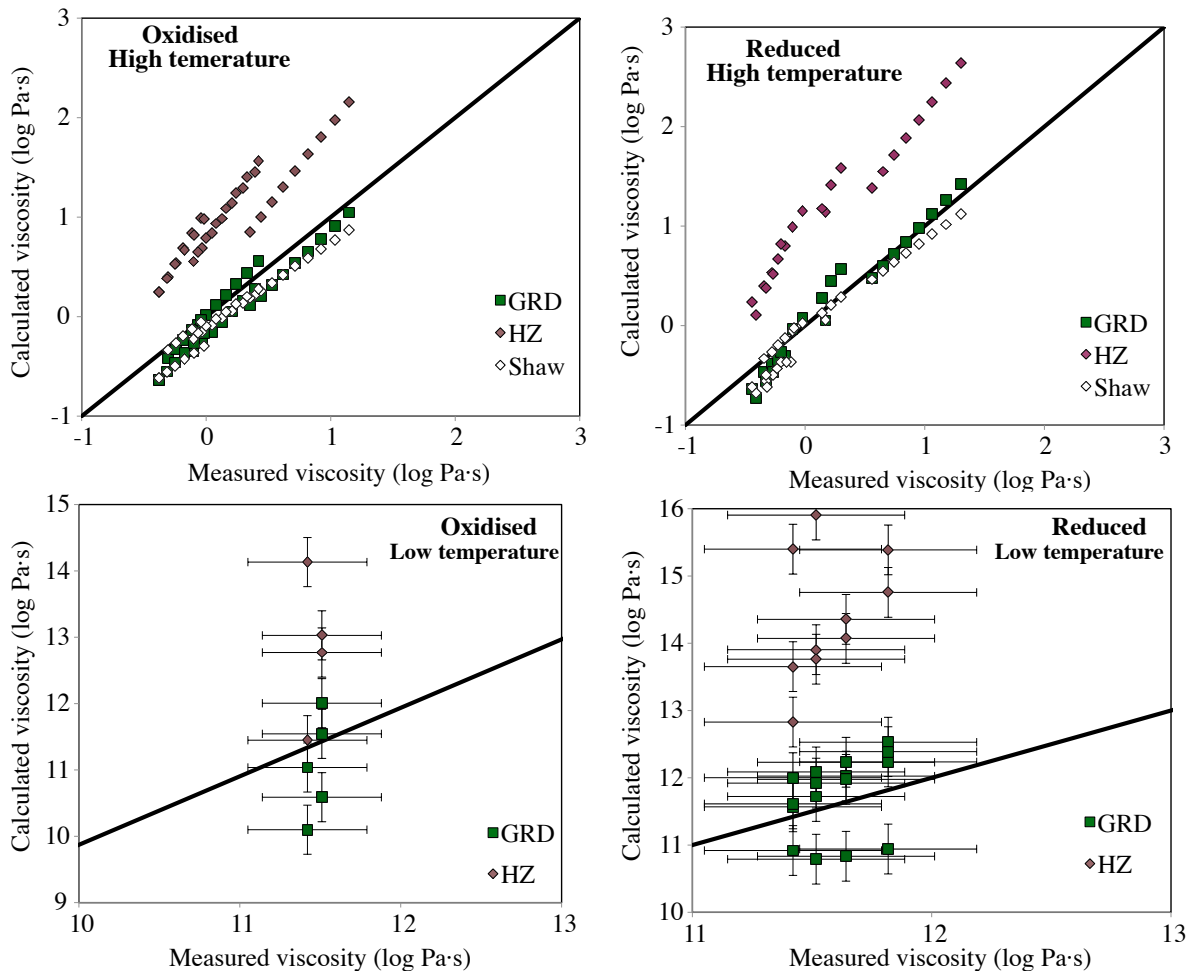


Figure 4.7: Comparison of the measured viscosity in air and under reduced oxygen fugacity (at 1 atm) with the calculated viscosity via empirical models: Shaw (1972); GRD, Giordano et al., (2006); HZ, Hui and Zhang, (2007).

with a RMSE of 0.16 log unit for oxidized and 0.15 log unit for reduced melts, respectively. The model of Hui and Zhang significantly deviates from the experimental data set with a RMSE of 0.85 log unit for oxidized and 0.99 log unit for reduced melts (Figure 4.7). The Shaw and GRD models reproduce these results best for high-temperature viscosity.

4.5.2 Calorimetric glass transition

The limiting fictive temperatures at the glass transition are given in Table 4.5 for all the samples. The quality and the reproducibility of the calorimetric curves ensure our ability to determine the glass transition temperature and depend strongly on the stability of the glass. The heat capacity curves of the oxidized samples shows a typical endothermic peak at the glass transition through heating, however as observed in Chevrel et al. (2012), the stable liquid field cannot be reached because of the onset of crystallization immediately above the glass transition (exothermal peak; Figure 4.8a). Even with a high cooling

cooling rate (°C/min)	T_f (°C)			
	25	20	15	10
AdMB-S2	670	-	-	-
AdMB-S4	635	659	666	664
AdMB-S5	630	636	636	638
AdMB-S6	629	628	625	620
AdMB-S8	637	635	631	628
BAMB1-S0	673	-	-	-
BAMB1-S1	654	657	656	653
BAMB1-S2	635	635	634	629
BAMB1-S3	646	643	640	628
BAMB1-S4	654	652	647	641
BAMB1-S5	647	646	643	638
IAMB-S1	-	632	-	-
IAMB-S2	-	-	-	-
IAMB-S3	634	630	627	627
IAMB-S4	632	625	623	619
IAMB-S5	628	625	618	615
OMB-S1	-	650	-	-
OMB-S2	638	637	632	629
OMB-S3	646	642	639	632
OMB-S4	638	636	631	624
YMB-S1	-	-	-	-
YMB-S2	-	-	-	-
YMB-S3	624	622	618	612
YMB-S4	623	620	617	611
YMB-S5	631	626	624	620

Table 4.5: Limiting fictive temperatures (T_f) for all samples measured for various cooling rate (25, 20, 15, 10 °C/min).

and subsequent heating rate of 25 K/min or when the heating is stopped just after the peak, subsequent glass transition measurements on the same sample are shifted to higher

temperatures. This shift toward high temperature may be attributed to the change of melt composition because of some crystallization or change in redox-state. For the most oxidized sample, a good reproducibility of the measurements was therefore not possible and the relationship between the glass transition temperature and the cooling history was biased (inverse relationship between cooling rate and T_f').

In contrast, the reduced samples measurements were reproducible (within 3 °C), and the relation between T_f' and the cooling rate is consistent with previous studies (Figure 4.8b). However, the shape of the heat capacity curve shows peculiar patterns. The heat capacity curves of the BAMB set of samples show very broad peaks forming a plateau of ~ 30 °C (Figure 4.8c).

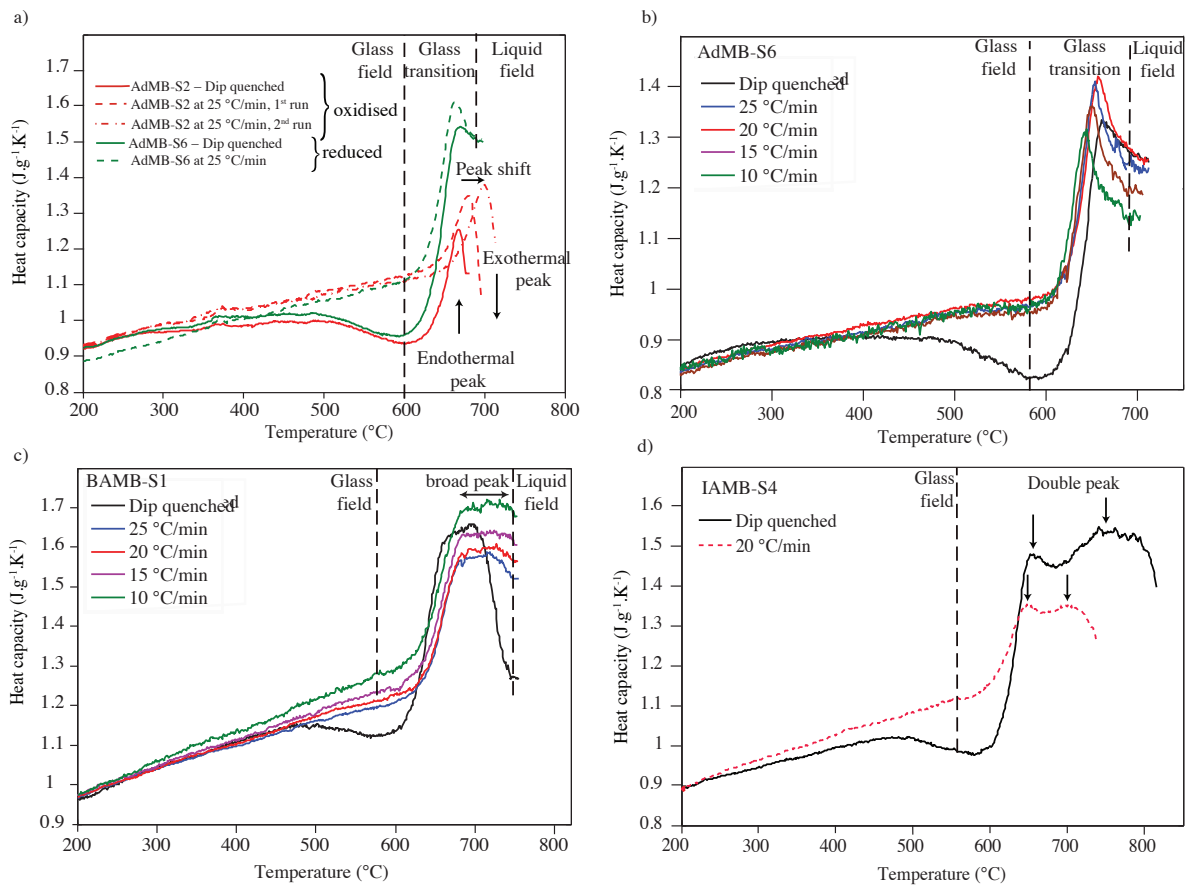


Figure 4.8: Example of the heat capacity curves. a) Example of sample AdMB-S2 equilibrated in air and AdMB-S6 equilibrated under reduced condition. The sample equilibrated in air shows crystallization (exothermal peak) after the glass transition is crossed and repeated measurements of the glass transition temperature are shifted to higher temperature. In contrast the sample equilibrated under low oxygen fugacity are reproducible and no crystallization occurs. b) Example of sample AdMB-S6 that shows a normal evolution of T_g vs cooling rate c) Example of sample BAMB-S1 that shows broad peak at the glass transition. d) Example of sample IAMB-S4 that shows the occurrence of double peaks

It was also noted that for IAMB samples, a second peak was reached after some 100 °C after the first peak (Figure 4.8d). In the literature there are unfortunately no studies about double or broad peaks. Only Kremers et al. (2012) observed a double peak that they interpreted to be the mingling of two glasses with the same composition but different redox state within a single sample. Here, no direct proof of variable redox state could be obtained, however in our study the chemical heterogeneity may be the reason for such features. The difference in glass transition temperature calculated with the GRD model at $\eta=10^{12}$ Pa·s between the two conjugate melts (LFe and LSi) in the BAMB-S1 samples is of 20 °C and seems to correlate with the broad peak dimension. However, for IAMB-S4-LFe and -LSi melts, the glass transition temperature difference calculated with the GRD model at $\eta=10^{12}$ Pa·s, is of about 11 °C; therefore the two peaks in Figure 4.8d are too far apart to be attributed to only variable compositions and redox changes might be additionally involved. Although it may not be the case as a general rule, the melt with less Si and more Fe (LFe) is expected to have a lower glass transition temperature than the conjugate Si-rich, Fe-poor melt (LSi). Hence, the first peak may correspond to the Fe-rich melt, the closer to the initial composition and the second peak to the Si-rich melt. In order to get the best estimate of the glass transition temperature for the samples, we therefore preferred to estimate the limiting glass transition temperature (T_f') only for the first peak, and at the onset of broad peak, that are the most likely to correspond to the composition which is both the most Fe-rich and closer to the starting melt composition.

4.5.3 Viscosity near the glass transition

Despite the challenges discussed above, total temperature errors (instrumental errors plus standard deviation from repeated measurements) are within ± 4 °C. The temperature dependence of viscosity near the glass transition is calculated and the error on the viscosity values is estimated at ± 0.37 log Pa·s. As mentioned above, the relationship between T_f' and the cooling rate was difficult to obtain for the oxidized samples. The best estimation was therefore obtained with the first heating segment after controlled cooling rate (20 or 25 K/min). The viscosity calculated at T_f' with the GRD and Hui and Zhang models are compared with the values estimated here (Figure 4.7). The GRD model is capable of estimating the viscosity within the errors induced by the calorimetric method with RMSE of 0.86 log unit for oxidized and 0.63 log unit for reduced samples, while the Hui and Zhang model yields results exceeding the measured values by several of orders of magnitude with a RMSE of 4.9 log unit for oxidized and 5.85 log unit for reduced samples. The parameters of the Arrhenian relationship (Eq.4.2) could not be obtained for the oxidized sample as only one viscosity data point was obtained. The fitting parameters for the reduced samples are given in Table 4.3.

4.5.4 Non-Arrhenian parameterization over the entire range of temperature

The entire viscosity data set for the oxidized and the reduced melts is fitted with a non-Arrhenian empirical relationship given as the Tammann-Vogel-Fulcher equation:

$$\log\eta = A_{TVF} + \frac{B_{TVF}}{T - C_{TVF}} \quad (4.3)$$

where T is melt temperature (K) and A_{TVF} represents a lower limit of silicate melt viscosity at infinite high temperature, and is approximately the same for all silicate melts (Myuller, 1955; Eyring et al., 1982; Angell, 1985; Russell et al., 2002, 2003). B_{TVF} and C_{TVF} are fitting parameters, which are dependent on the melt chemical composition. The optimal value for A_{TVF} is still debated but, here, the data were fitted using a preferred value for Fe-rich basaltic melts of -4.125 (Chevrel et al., 2012) that slightly improves the quality of the fit compared to the common value proposed by the GRD model ($= -4.55 \pm 0.21$). All parameters are given in Table 4.6. In Figure 4.9, the results are compared with the viscosity of some selected terrestrial and lunar Fe-rich basalts. At superliquidus conditions, the Martian basalts viscosities are as low as those of the Fe-Ti-rich lunar basalts and among the lowest viscosity recorded for the terrestrial ferro-basalts. As suggested in Chevrel et al. (2012), the viscosity of Martian basalts is between 0.5 and 1 order of magnitude lower than terrestrial tholeiitic basalts at all magmatic temperatures.

	A_{TVF} (log Pa s)	B_{TVF} (log Pa s / K)	C_{TVF} (K)	RMSE ^a	T_i 10/10
AdMB-S2	-4.125	4456	633.3	0.038	-
AdMB-S6	-4.125	4420	617.3	0.045	620
BAMB-S0	-4.125	4975	626.9	0.053	-
BAMB-S1	-4.125	4819	621.5	0.101	653
IAMB-S1	-4.125	4583	611.9	0.036	-
IAMB-S4	-4.125	4419	616.6	0.116	619
OMB-S1	-4.125	4185	655.3	0.038	-
OMB-S4	-4.125	4208	637.4	0.131	624
YMB-S1	-4.125	4216	628.0	0.034	-
YMB-S5	-4.125	4175	632.6	0.085	620

Table 4.6: Fitting parameters of the TVF equation for the oxidized and reduced melts using a common A_{TVF} value.

^a Root Mean Square Error

4.6 Discussion

The viscosity controls the ascent rate of magmas and emplacement of lava flows. Magmas are polyphase materials composed of a viscous melt and suspended particles (crystals and bubbles). Their apparent viscosity is therefore a combination of the melt

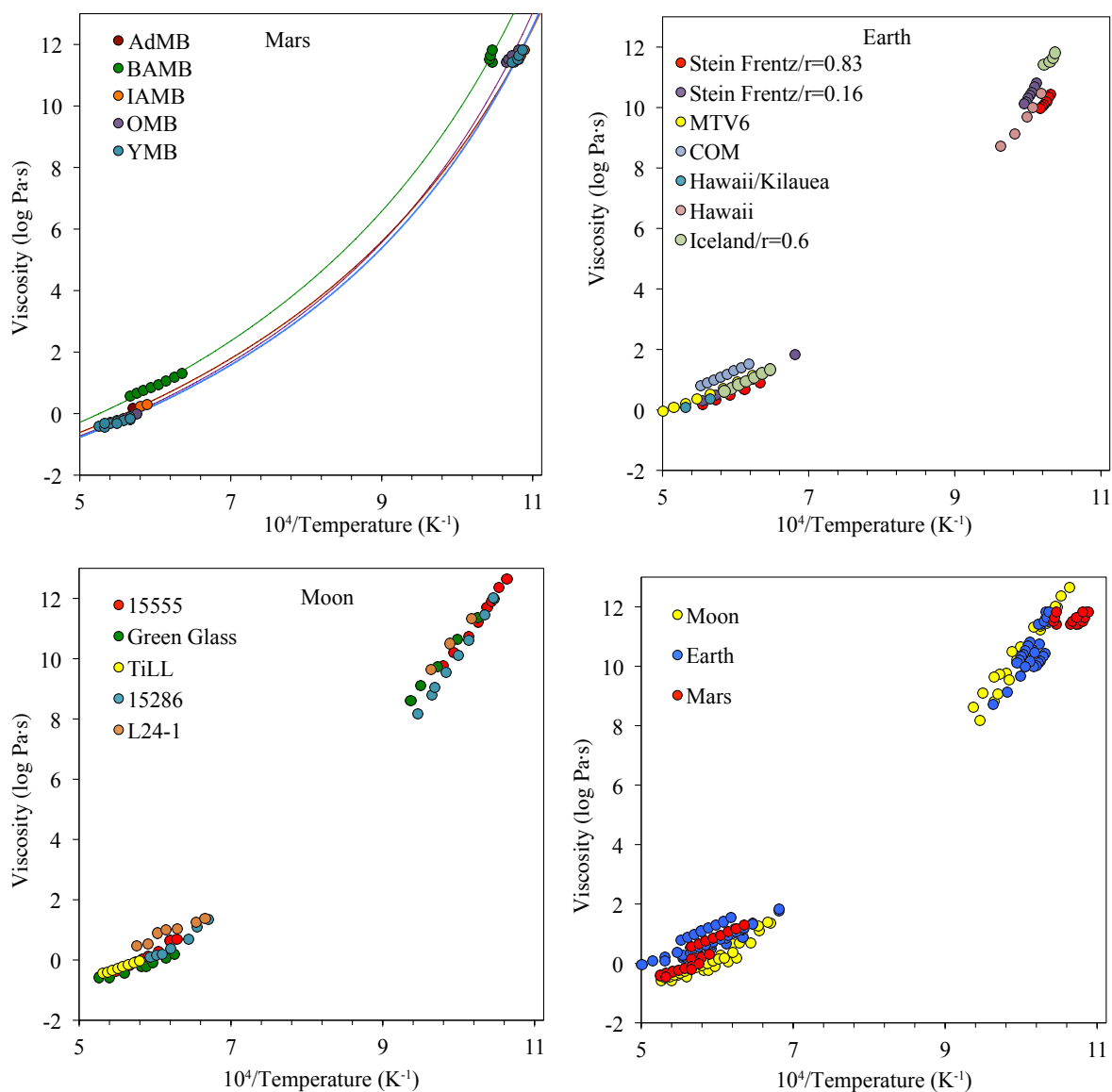


Figure 4.9: Viscosity data for Mars, Moon and Earth. a) Viscosity data points under low fO_2 and fitting TVF curves for the investigated Martian melts. b) Terrestrial Fe-rich basaltic melts including natural basalts from Western Volcanic Zone Iceland and from Craters of The Moon, USA (Iceland and COM, respectively; personal unpublished data); from Hawaii (Hawaii/Kilauea is from Kushiro et al., 1976 and Hawaii is R839-5.8 from Gottsmann et al., 2002) and basalt from Stein Frentz with two different redox state (Bouhifd et al., 2004); a synthetic ferro-basalt (MTV; Toplis et al., 1994). $r = FeO/Fe_{tot}$. c) Synthetic lunar basalts including the primitive basalt 15555 from Cukierman et al. (1973), the green glass from Apollo 15 (Uhlmann et al., 1974), the Ti-rich basalt from Apollo 11 (TiLL, Murase and McBirney, 1970), a basaltic glass (15286) Uhlmann and Klein (1976) and a mare basalt (L-24) from Handwerker et al. (1978). d) Comparison of all the compiled data

viscosity and the effect of the particles (e.g., Murase and McBirney, 1973; Shaw, 1969; Ryerson et al., 1988; Lejeune and Richet, 1995; Sato, 2005; Petford, 2009). If the particle concentration is low (below the critical volume fraction depending on the crystals shape and size distribution) the physical behavior of the magma is controlled by the viscosity of the melt phase that is Newtonian (Lejeune and Richet, 1995; Costa et al., 2009). When the crystal fraction becomes too high, the viscosity is no longer controlled by the melt but by the particles network and become non-Newtonian, strain-rate dependent (Caricchi et al., 2007; Lavallée et al., 2007; Costa et al., 2009; Petford, 2009; Cordonnier et al., 2012). The viscosity of a flowing basaltic lava increases during emplacement and cooling, in a way that depends on the crystallization sequence (e.g. Shaw, 1969; Marsh, 1981; Pinkerton and Stevenson, 1992; Crisp et al., 1994; Sato, 2005; Villeneuve et al., 2008). A basaltic cooling-limited lava flow ceases flowing when its viscosity reach a critical value associated with the interlocking of the crystals network (near the random maximum packing of crystals; (e.g. Murase and McBirney, 1973; Shaw, 1969; Marsh, 1981; Crisp et al., 1994). The following section offers a framework to interpret the diversity of volcanic landforms on Mars and explore in which cases variations in lava flow morphology may be comfortably related to variations in chemistry.

For this purpose, the viscosity of the magma (melt + crystals) is calculated during the crystallization sequence for the compositions YMB (Amazonian), AdMB (Hesperian), BAMB (trachy-basalt) and IAMB (mildly alkaline-basalts). The melt phase is calculated using the most appropriate model for Martian compositions, namely the GRD model as demonstrated previously. The effect of crystals is determined using the most sophisticated approach taking into account two populations of crystals with various shapes and the non-Newtonian behavior of crystal bearing magmas (Costa et al., 2009) using the fit from (Cimarelli et al., 2011). The first calculation, considers two populations of crystals: the mafic minerals approximated with spherical shape and the plagioclase approximated a needle-like shape. A second calculation estimates the viscosity increase attributed to crystallization of needle-like shape mafic crystals corresponding to the formation of spinifex textures, that is likely to happen in magma with high-normative olivine content (Bertka and Holloway, 1994; Bost et al., 2012). In both cases, the strain rate is held constant at 1 s^{-1} . that is reasonable value for natural basaltic lava flow (Crisp et al., 1994).

The crystallization sequence can be directly modeled using the low-pressure MELTS algorithm (Ghiorso and Sack, 1995). According to petrographic observation of the martian basalts and to experimental petrology, the surface conditions are estimated by Monders et al. (2007); Herd et al. (2002) to be 1 bar under an oxygen fugacity of one log-units below the Quartz-Fayalite-Magnetite buffer (QFM-1). The validation of using MELTS for Gusev basalts, was tested by Monders et al. (2007) and shows good agreement with

experimental trend, although they do not recommend the use of MELTS to calculate the liquid lines of descent after a certain amount of crystallization, when the residual liquid become too Fe-rich. Baratoux et al. (2013) showed that mineral assemblages crystallizing at these conditions from primary mantle melts correspond to the observed mineralogy at the Mars' surface consisting in general of olivine, plagioclase, and a two-pyroxene assemblage (Poulet et al., 2009). Moreover, the observed evolution of the ratio of the low-calcium pyroxene (LCP) to the high-calcium pyroxene (HCP) end-members from the Late Noachian to the Amazonian periods would appear as a consequence of the evolution of the conditions of melting (Baratoux et al., 2011) associated with planetary cooling (Baratoux et al., 2013). The crystallization of the subalkaline compositions exhibits, as in the case of komatiites, a very large temperature difference between the liquidus and solidus temperature, that is over 300°C for the Amazonian melt. The crystallization sequence of the trachy-basalt is distinguishable from the others with the lower proportion of pyroxene (15%) and a large proportion of feldspar (Figure 4.10).

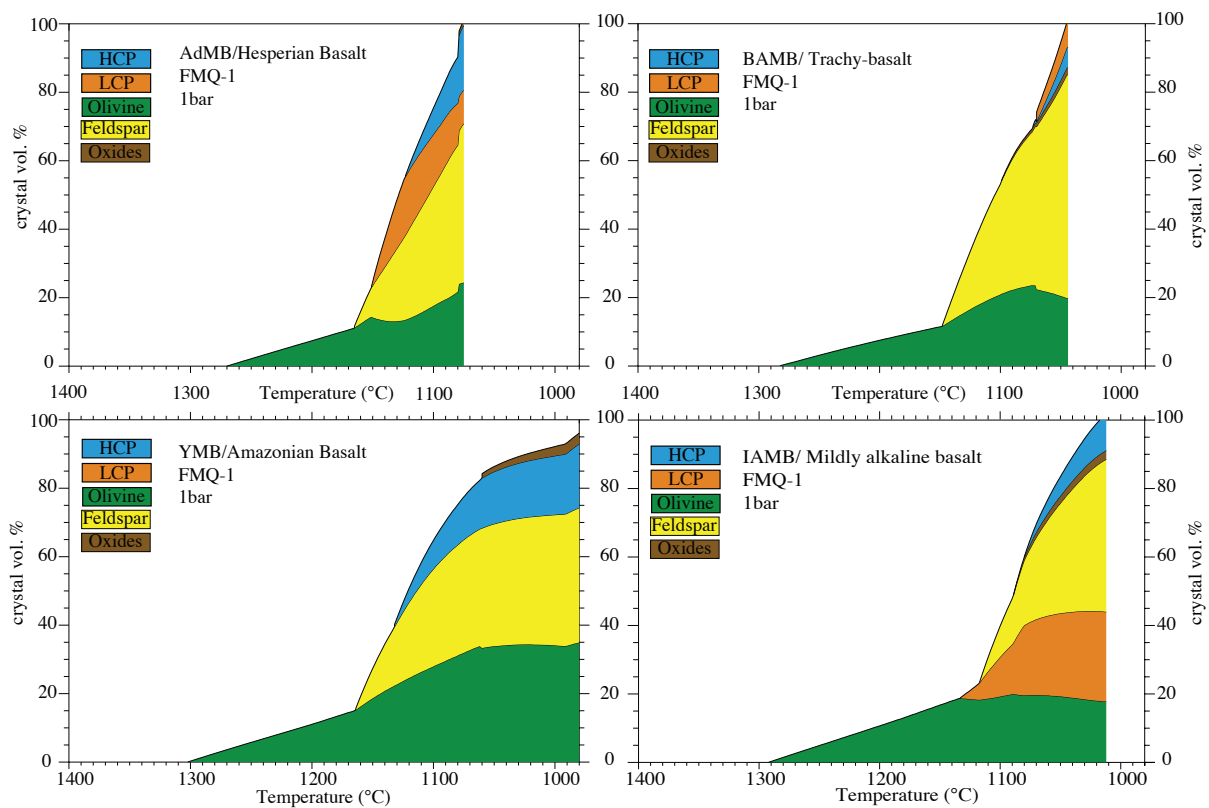


Figure 4.10: Crystallization sequence at 1bar and QFM-1 for all investigated compositions. The sample OMB is not showed as its crystallization sequence is identical to AdMB

Figure 4.11 shows the increase of viscosity for the four compositions as temperature decreases and crystallization takes place. A sharp increase of viscosity with temperature occurs when the crystal fraction approaches the maximum crystal packing. The rate of the

increase of apparent viscosity with temperature starts decreasing at a critical crystal fraction defining the rheological transition where the viscous behavior is no longer controlled by the melt but by the solid framework (Lejeune and Richet, 1995; Costa et al., 2009). This transition is the rheological limit of flow advance, which is likely to be recorded in the final morphology of the lava flow (Giordano et al., 2007, and see previous chapter).

Although the Amazonian melt has a lower viscosity than the Hesperian basalt; the viscous behavior during crystallization and the viscosity at the maximum packing is very similar (10^5 - $10^{5.2}$ Pa·s). This result indicates that it would be very difficult to distinguish Hesperian or Amazonian flow from their morphology. However, the viscosity at the maximum packing for a lava crystallizing needle-shape crystals, like spinifex, for which the maximum critical packing is lower, would be around 10^4 Pa·s. Possible differences in viscosity between Amazonian and Hesperian lavas would be likely attributed to the kinetic of crystallization and the ability to produce spinifex texture rather than differences in the viscosity of the liquid phase. In detail, a lava able to crystallise spinifex-needle-like crystals would be interpreted as having a low apparent viscosity using equations for the emplacement of an isothermal Newtonian fluid (as the maximum crystals packing is reduced in the presence of needles). We note that the range of viscosity obtained here is in agreement with typical viscosities of Martian lava flows obtained from morphometric analyses (Hauber et al., 2011; Pasckert et al., 2012; Grott et al., 2013, and references therein). However, the extremely low values of apparent viscosity obtained for some recent lava flows in the Central Elysium Planitia, on Mars (10^2 Pa·s; Vaucher et al., 2009b) are at the extreme lower limits of our range of predictions.

The viscosity of all studied compositions are less than 1 Pa·s. at liquidus temperatures. The magma rise speed may be calculated from equations given in Wilson et al. (2009). With such low values of viscosity, the Reynolds number is above 2000 and the flow within the magma conduit is turbulent. Considering equations for turbulent flows, a dyke width of 3 m, and a pressure gradient of $500 \text{ Pa}\cdot\text{m}^{-1}$ as in Wilson et al. (2009), the magma rise speed appears to be greater than $10 \text{ m}\cdot\text{s}^{-1}$ (or even higher if shear heating takes place). These values are significantly faster than estimates of Wilson et al. (2009) who considered a viscosity of 100 Pa·s. Cooling will be therefore negligible during magma ascent. Fractional crystallization should therefore remain limited as long as the magma remains buoyant. Crustal contamination and chemical interactions with the host rocks should be also limited for the same reasons. These low viscosities may be one of the key parameters to understand the abundance of primitive magmas at the surface of Mars (McSween et al., 2006b; Baratoux et al., 2011) and the abundance of olivine in comparison with our planets (Poulet et al., 2009).

A larger viscosity difference between the primitive basalts and the more alkaline-

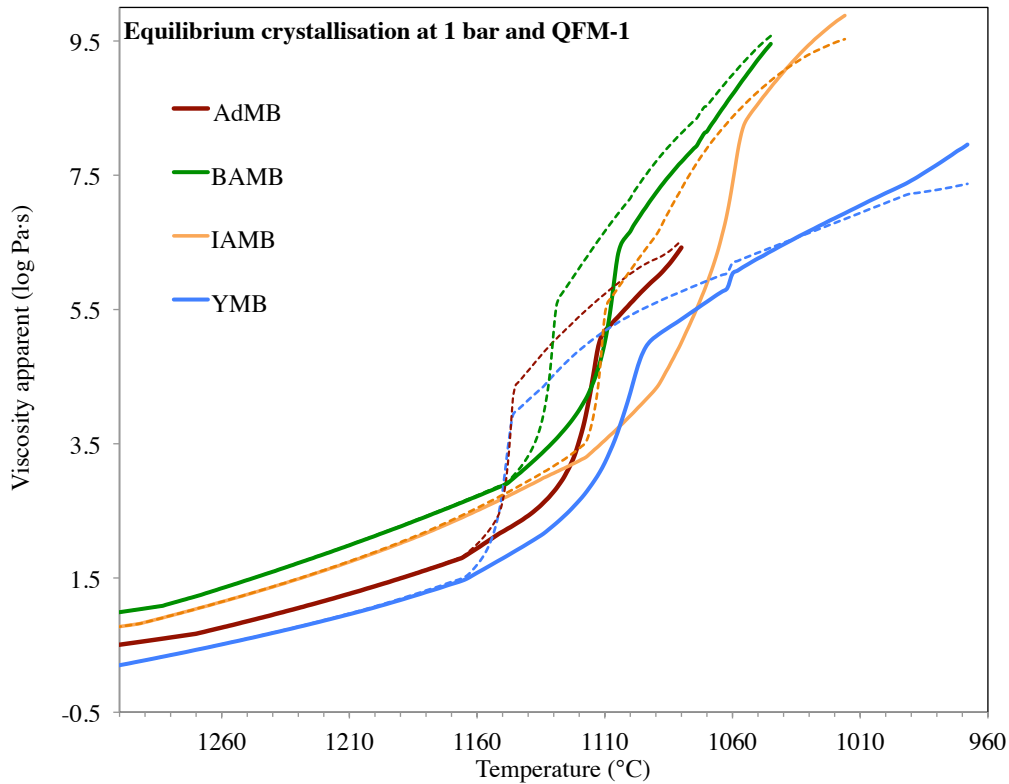


Figure 4.11: Apparent viscosity of Martian lavas as a function of temperature taking into account the crystallization sequence. The bold line are calculation for two population of crystals (magic minerals being considered as spheres and feldspar as needles) and dashed line are calculation for all crystals being considered as needles (to mimic spinifex textures).

rich -basalt is found with expected values of 0.5 log unit at superliquidus regime and 1 to 3 log units at the crystal maximum packing (10^6 - 10^8 Pa·s). A factor of two for the magma rise speed is expected from the slight differences at magmatic temperature between primitive basalts and the more alkaline-rich-basalts. The larger difference at maximum packing suggests that the morphology of alkaline-rich lavas may be distinguished from that of tholeiitic lava. A fraction or all of the upper range of lava flows for which inferred viscosities were found above 10^6 Pa·s may be proposed as candidates for the expression of effusive and alkaline-rich basaltic volcanism, revealed by a minority of volcanic rocks at Gusev craters. Therefore, one does not need to invoke the occurrence of basaltic andesite or andesite lavas to explain these relatively high viscosity values and Martian lava flow would be essentially dominated by low-silica content (basaltic) with variable degrees of alkalinity. This hypothesis is compatible with the study of Warner and Gregg who estimated the viscosity of an andesitic lava flow from Sabancaya volcano (Peru) to be 10^{10} - 10^{12} Pa·s and therefore reject the possibility that lava flow on Mars having viscosity of 10^6 Pa·s could be andesitic.

4.7 Conclusion

The viscosity measurements of synthetic melts, having the iron-rich composition of basaltic rocks found on Mars' surface and representing primary melts of the primitive mantle of Mars at different periods of time, reveal viscosities similar to some Fe-rich basaltic terrestrial and lunar lavas. Homogeneous glasses were difficult to produce as some crystallization occurred and chemical elements migrated into conjugate phases (LFe-LSi) in a few seconds during the quenching process. The viscosities at low temperature are therefore more challenging to interpret but could be estimated within reasonable error bars. Overcoming such difficulties in future will necessitate a faster quenching technique, or quenching under sustained reducing condition. A comparison with rheological empirical model available in the literature reveals that the GRD model (Giordano et al., 2008) is the best to reproduce experimental data at both super liquidus regime and near the glass transition while Shaw (1972) model is only suitable for high temperature and the model of (Hui and Zhang, 2007) shows very large discrepancies. Estimation of the apparent viscosity of crystallizing lavas is in agreement with most of the value calculated from lava flow morphology on Mars surface. The evolution of the chemical composition of primary melts through time does not lead to major viscosity variations and therefore observation of lava flow with different apparent viscosity cannot be characteristic of their age. Low apparent viscosity ($10^2 - 10^4$ Pa·s) inferred from the morphology would be rather attributed to komatiite-like lava flows and the higher values ($10^6 - 10^8$ Pa·s) may include alkaline-rich lavas rather than more Si-rich composition.

4.8 Supplementary material

Sample	FeO/FeO _{tot}	N		SiO ₂	TiO ₂	Al ₂ O ₃	FeO _{tot}	MnO	MgO	CaO	Na ₂ O	K ₂ O	P ₂ O ₅
AdMB				47.01	0.59	10.86	19.43	0.42	10.14	8.09	2.66	0.15	0.65
AdMB-S2	0.21	40	average	46.77	0.61	10.93	19.65	0.44	9.23	8.73	2.88	0.18	0.57
			stdev	0.38	0.10	0.23	0.44	0.07	0.28	0.20	0.08	0.02	0.05
			max	47.60	0.87	11.40	20.99	0.66	9.95	9.17	3.03	0.22	0.66
			min	45.98	0.38	10.55	18.63	0.30	8.68	8.28	2.69	0.13	0.45
			rstdev	0.83	26.83	2.13	2.38	24.12	3.20	2.37	3.12	16.92	11.88
			max-min	1.62	0.49	0.84	2.35	0.36	1.27	0.89	0.33	0.08	0.21
AdMB-S3	0.33	40	average	48.94	0.57	11.06	17.95	0.42	8.77	8.39	3.16	0.22	0.52
			stdev	0.40	0.12	0.23	0.37	0.06	0.32	0.23	0.11	0.03	0.04
			max	50.07	0.76	11.56	18.73	0.52	9.50	8.84	3.46	0.29	0.60
			min	48.09	0.33	10.59	17.35	0.31	8.12	7.82	2.99	0.17	0.43
			rstdev	0.84	35.65	2.20	2.12	18.69	3.99	3.00	3.65	15.16	10.56
			max-min	1.98	0.43	0.98	1.38	0.21	1.39	1.02	0.48	0.12	0.17
AdMB-S4	0.37	40	average	48.36	0.58	10.88	18.61	0.42	8.90	8.45	3.05	0.21	0.54
			stdev	0.47	0.12	0.23	0.48	0.08	0.30	0.20	0.08	0.02	0.03
			max	49.35	0.85	11.39	19.97	0.59	9.51	8.83	3.21	0.24	0.61
			min	47.48	0.38	10.39	17.71	0.28	8.27	7.99	2.84	0.17	0.47
			rstdev	0.98	32.65	2.18	2.72	27.66	3.59	2.52	2.93	11.14	7.08
			max-min	1.88	0.47	1.00	2.26	0.30	1.24	0.84	0.37	0.07	0.14
AdMB-S5	0.48	40	average	47.46	0.58	10.98	19.41	0.44	8.97	8.59	2.84	0.18	0.57
			stdev	0.37	0.10	0.19	0.38	0.08	0.26	0.14	0.11	0.03	0.04
			max	48.19	0.78	11.35	20.01	0.62	9.48	8.86	3.08	0.24	0.68
			min	46.66	0.34	10.40	18.45	0.33	8.41	8.19	2.55	0.12	0.50
			rstdev	0.79	29.27	1.87	2.06	23.13	3.03	1.68	4.39	22.19	8.34
			max-min	1.53	0.44	0.95	1.56	0.29	1.07	0.67	0.53	0.12	0.18
AdMB-S6	0.63	37	average	47.62	0.64	11.13	18.95	0.43	9.13	8.53	2.84	0.17	0.57
			stdev	0.35	0.11	0.24	0.44	0.11	0.26	0.17	0.06	0.02	0.05
			max	48.38	0.87	11.57	19.80	0.68	9.60	8.83	2.97	0.21	0.67
			min	47.04	0.44	10.57	18.00	0.23	8.69	8.06	2.71	0.13	0.46
			rstdev	0.75	25.03	2.30	2.46	46.45	2.97	2.15	2.37	16.24	11.02
			max-min	1.35	0.43	1.00	1.81	0.45	0.91	0.77	0.26	0.07	0.22
AdMB-S8	0.78	40	average	49.19	0.59	11.38	16.91	0.44	9.02	8.63	3.07	0.20	0.57
			stdev	0.41	0.13	0.26	0.33	0.06	0.30	0.19	0.13	0.02	0.05
			max	50.07	0.81	11.73	17.40	0.54	9.58	9.05	3.37	0.24	0.67
			min	48.26	0.31	10.79	15.96	0.30	8.18	8.18	2.76	0.15	0.47
			rstdev	0.85	43.40	2.38	2.05	20.40	3.71	2.36	4.54	14.71	10.95
			max-min	1.81	0.51	0.94	1.44	0.24	1.40	0.88	0.61	0.09	0.19

Table 4.7: Electron microprobe analyses in weight percent, normalize to 100 %. for each sample. N represents the number of chemical analyses per sample. If two composition are distinguishable, their compositions is also given as LSi for the silica-rich liquid and LFe for the iron-rich liquid. The accelerating voltage was 15 kV and a defocused beam of $5\mu\text{m}$ was used with a current of 5 nA. The counting time was 10 s for Si, Al, K, Na, P, Cl and 30 s for Ca, Fe, Mg, Mn, Ti and half this time for the background. The standards used were Wallastonite for Si and Ca, Albite for Al, Ilmenite for Ti, Hematite for Fe, Periclase for Mg, Ilmenite for Mn, Albite for Na, Orthoclase for K, Apatite for P and Vanadinit for Cl. The data were corrected according to the PAP procedure (Pouchou and Pichoir, 1985). Note that the amount of iron ($\text{Fe}_2\text{O}_3 + \text{FeO}$) is always expressed here as FeO_{tot} .

Sample	FeO/FeO _{tot}	N		SiO ₂	TiO ₂	Al ₂ O ₃	FeO _{tot}	MnO	MgO	CaO	Na ₂ O	K ₂ O	P ₂ O ₅
BAMB				50.22	0.94	13.46	13.87	0.24	8.43	6.12	4.21	1.09	1.41
BAMB-S0	0.26	40	average	48.84	0.97	13.22	15.32	0.26	8.11	6.56	4.52	1.04	1.17
			stdev	0.34	0.13	0.26	0.37	0.07	0.28	0.18	0.22	0.05	0.08
			max	49.49	1.31	14.00	16.16	0.46	8.71	6.99	4.83	1.13	1.41
			min	48.08	0.67	12.71	14.56	0.12	7.31	6.14	3.53	0.94	0.99
			rstdev	0.71	20.16	2.03	2.55	61.59	3.88	2.87	6.19	5.15	7.67
			max-min	1.41	0.64	1.29	1.60	0.33	1.40	0.85	1.30	0.19	0.41
BAMB-S1	0.62	40	average	52.71	0.95	13.98	11.85	0.23	7.16	5.92	4.80	1.23	1.16
			stdev	1.50	0.12	0.35	1.06	0.06	0.49	0.40	0.26	0.11	0.07
			max	56.21	1.25	14.84	13.35	0.35	7.72	6.57	5.28	1.58	1.29
			min	50.88	0.74	13.25	9.33	0.08	5.51	4.98	3.97	1.10	0.99
			rstdev	2.95	15.75	2.67	11.34	69.65	8.89	8.01	6.43	10.29	6.67
			max-min	5.33	0.52	1.59	4.02	0.27	2.21	1.59	1.32	0.48	0.30
LSi		6	average	55.94	0.91	14.61	9.67	0.18	6.16	5.14	4.81	1.47	1.08
			stdev	0.22	0.09	0.19	0.27	0.06	0.38	0.11	0.22	0.06	0.04
			max	56.21	1.00	14.84	10.13	0.24	6.63	5.27	5.09	1.58	1.14
			min	55.67	0.74	14.27	9.33	0.08	5.51	4.98	4.42	1.40	1.04
			rstdev	0.39	12.36	1.30	2.89	70.75	6.89	2.23	5.09	4.51	4.03
			max-min	0.54	0.26	0.57	0.80	0.15	1.12	0.29	0.67	0.18	0.11
LFe		8	average	51.63	0.91	13.72	12.68	0.25	7.43	6.21	4.90	1.15	1.15
			stdev	0.55	0.10	0.28	0.38	0.07	0.18	0.20	0.40	0.04	0.03
			max	52.50	1.10	14.20	13.35	0.34	7.62	6.57	5.28	1.24	1.21
			min	50.88	0.79	13.25	12.16	0.14	7.11	5.98	3.97	1.11	1.11
			rstdev	1.09	12.48	2.14	3.15	52.97	2.48	3.38	10.19	3.69	3.11
			max-min	1.62	0.31	0.96	1.19	0.20	0.51	0.60	1.32	0.13	0.10
BAMB-S2	0.64	40	average	49.79	1.00	13.44	14.11	0.26	8.05	6.50	4.62	1.05	1.18
			stdev	1.74	0.12	0.46	1.54	0.06	0.59	0.40	0.23	0.12	0.05
			max	53.98	1.27	14.57	15.96	0.37	8.80	7.10	5.12	1.34	1.30
			min	47.99	0.75	12.68	10.41	0.12	6.82	5.44	3.74	0.91	1.08
			rstdev	3.63	15.74	3.61	14.75	51.53	8.64	7.42	6.26	13.34	4.74
			max-min	5.99	0.52	1.89	5.55	0.26	1.98	1.67	1.37	0.44	0.22
LSi		10	average	52.63	1.04	14.09	11.64	0.23	7.14	5.91	4.89	1.25	1.18
			stdev	0.62	0.12	0.28	0.37	0.08	0.20	0.24	0.11	0.05	0.05
			max	53.98	1.27	14.57	12.31	0.37	7.38	6.16	5.12	1.34	1.25
			min	51.95	0.87	13.71	10.41	0.12	6.82	5.44	4.74	1.17	1.08
			rstdev	1.19	13.70	2.05	5.49	67.89	2.90	4.50	2.23	4.55	4.88
			max-min	2.04	0.40	0.87	1.90	0.25	0.56	0.72	0.38	0.17	0.17
LFe		20	average	48.77	0.99	13.18	14.97	0.29	8.41	6.72	4.50	0.99	1.19
			stdev	0.47	0.11	0.26	0.48	0.05	0.30	0.22	0.21	0.04	0.05
			max	49.54	1.20	13.87	15.96	0.37	8.80	7.10	4.83	1.07	1.30
			min	47.99	0.81	12.68	14.11	0.22	7.84	6.21	3.74	0.91	1.11
			rstdev	0.97	14.07	2.08	3.40	21.16	3.78	3.48	5.70	4.56	4.58
			max-min	1.54	0.39	1.19	1.85	0.15	0.97	0.89	1.08	0.16	0.19
BAMB-S3	0.84	40	average	53.94	0.93	14.19	10.93	0.20	6.96	5.75	4.76	1.30	1.05
			stdev	1.60	0.12	0.38	1.30	0.07	0.50	0.34	0.22	0.11	0.07
			max	55.27	1.12	14.89	15.29	0.35	8.88	6.99	5.08	1.43	1.21
			min	48.36	0.57	12.89	9.64	0.03	6.28	5.38	4.35	0.94	0.89
			rstdev	3.30	21.27	2.96	13.43	268.11	7.93	6.23	5.15	12.10	7.45
			max-min	6.91	0.56	2.00	5.65	0.32	2.60	1.60	0.74	0.49	0.32
LSi		37	average	54.37	0.93	14.26	10.58	0.20	6.84	5.67	4.78	1.33	1.05
			stdev	0.43	0.12	0.26	0.42	0.07	0.25	0.17	0.22	0.06	0.06
			max	55.27	1.12	14.89	11.64	0.35	7.28	6.05	5.08	1.43	1.19
			min	53.45	0.57	13.65	9.64	0.03	6.28	5.38	4.35	1.20	0.89
			rstdev	0.81	21.55	1.88	4.40	277.64	3.93	3.07	5.08	4.85	6.65
			max-min	1.82	0.56	1.24	2.00	0.32	1.00	0.66	0.74	0.23	0.30
LFe		3	average	48.59	0.95	13.26	15.19	0.19	8.43	6.76	4.54	0.96	1.17
			stdev	0.28	0.12	0.49	0.12	0.03	0.47	0.20	0.14	0.02	0.03
			max	48.90	1.09	13.82	15.29	0.23	8.88	6.99	4.70	0.98	1.21
			min	48.36	0.86	12.89	15.06	0.17	7.95	6.62	4.44	0.94	1.15
			rstdev	0.57	13.76	3.82	0.79	16.96	5.88	2.98	3.18	1.89	2.77
			max-min	0.54	0.23	0.93	0.23	0.06	0.93	0.37	0.26	0.04	0.06
BAMB-S4	0.77	40	average	51.15	1.02	13.75	12.56	0.25	8.09	6.49	4.55	1.07	1.06
			stdev	1.40	0.14	0.30	1.07	0.07	0.48	0.33	0.28	0.10	0.11
			max	53.96	1.26	14.53	13.86	0.44	8.80	7.01	5.00	1.31	1.20
			min	49.73	0.71	12.96	10.15	0.11	6.99	5.75	3.40	0.96	0.78
			rstdev	2.81	19.90	2.34	10.57	69.81	6.88	5.74	8.21	10.07	13.78
			max-min	4.23	0.56	1.58	3.71	0.33	1.80	1.26	1.60	0.35	0.42
LSi		10	average	53.34	1.05	14.00	10.96	0.24	7.44	6.02	4.79	1.21	0.92
			stdev	0.34	0.14	0.29	0.44	0.06	0.30	0.14	0.15	0.06	0.07
			max	53.96	1.25	14.53	11.65	0.36	7.83	6.17	5.00	1.31	1.06
			min	53.02	0.85	13.65	10.15	0.15	6.99	5.75	4.49	1.10	0.78
			rstdev	0.65	16.48	2.13	4.32	40.55	4.26	2.45	3.28	5.28	8.89
			max-min	0.94	0.40	0.88	1.50	0.20	0.84	0.43	0.51	0.21	0.28
LFe		30	average	50.32	1.00	13.66	13.16	0.25	8.34	6.66	4.46	1.02	1.12
			stdev	0.28	0.14	0.25	0.39	0.08	0.25	0.17	0.26	0.04	0.05
			max	51.09	1.26	14.08	13.86	0.44	8.80	7.01	4.75	1.09	1.20
			min	49.73	0.71	12.96	12.45	0.11	7.76	6.37	3.40	0.96	0.98
			rstdev	0.57	20.04	1.96	3.12	74.18	3.17	2.65	7.74	3.81	5.47
			max-min	1.36	0.56	1.12	1.41	0.33	1.04	0.64	1.35	0.13	0.22

Table 4.7: Continuation

Sample	FeO/FeO _{tot}	N		SiO ₂	TiO ₂	Al ₂ O ₃	FeO _{ox}	MnO	MgO	CaO	Na ₂ O	K ₂ O	P ₂ O ₅
IAMB				49.09	1.10	8.58	20.36	0.38	9.82	5.99	3.10	0.62	0.97
IAMB.S1	0.21	39	average	48.14	1.09	8.52	21.31	0.41	9.33	6.45	3.32	0.57	0.86
			stdev	0.39	0.14	0.22	0.48	0.09	0.36	0.15	0.09	0.04	0.06
			max	48.90	1.39	9.14	22.18	0.59	10.13	6.93	3.52	0.67	0.97
			min	47.11	0.82	8.12	20.28	0.26	8.47	6.18	3.13	0.48	0.74
			rstdev	0.83	16.88	2.70	2.34	33.43	4.31	2.42	2.96	9.09	7.73
			max-min	1.79	0.57	1.02	1.90	0.33	1.66	0.75	0.39	0.19	0.23
IAMB.S2	0.40	40	average	48.49	1.07	8.54	20.96	0.40	9.38	6.37	3.36	0.56	0.88
			stdev	1.18	0.14	0.28	1.15	0.08	0.37	0.24	0.15	0.06	0.06
			max	51.77	1.47	9.23	22.18	0.56	10.10	6.87	3.75	0.74	1.01
			min	46.98	0.67	8.03	17.70	0.26	8.45	5.91	3.13	0.49	0.74
			rstdev	2.51	21.43	3.51	6.52	30.98	4.39	4.08	4.72	11.25	8.61
			max-min	4.79	0.80	1.20	4.47	0.30	1.65	0.96	0.63	0.25	0.27
IAMB.S3	0.69	40	average	53.59	1.03	9.18	16.62	0.34	8.05	5.73	3.85	0.77	0.86
			stdev	1.22	0.13	0.23	0.99	0.07	0.40	0.27	0.16	0.08	0.06
			max	55.63	1.26	9.66	19.21	0.51	9.12	6.29	4.11	0.93	0.97
			min	50.96	0.78	8.57	14.94	0.23	7.24	5.35	3.33	0.55	0.74
			rstdev	2.40	16.80	2.65	6.65	28.60	5.55	4.98	4.89	15.21	7.74
			max-min	4.67	0.48	1.10	4.27	0.28	1.88	0.95	0.78	0.38	0.23
IAMB.S4	0.82	149	average	53.49	1.03	9.25	16.83	0.35	8.09	5.69	3.70	0.77	0.79
			stdev	4.09	0.15	0.58	3.26	0.09	1.12	0.70	0.36	0.20	0.07
			max	58.60	1.48	10.58	22.46	0.55	10.19	7.00	4.23	1.09	1.01
			min	46.95	0.71	8.07	12.72	0.14	6.47	4.70	2.95	0.46	0.61
			rstdev	8.71	20.76	7.14	25.61	64.44	17.32	14.83	12.24	42.68	10.95
			max-min	11.64	0.77	2.51	9.74	0.41	3.72	2.30	1.27	0.62	0.40
LSi		30	average	57.69	0.97	9.81	13.63	0.29	6.95	4.95	3.99	0.98	0.75
			stdev	0.39	0.13	0.21	0.36	0.06	0.28	0.15	0.12	0.05	0.05
			max	58.60	1.32	10.13	14.46	0.40	7.56	5.30	4.23	1.09	0.87
			min	57.03	0.71	9.31	13.03	0.14	6.47	4.70	3.65	0.86	0.66
			rstdev	0.68	18.70	2.27	2.76	42.85	4.36	3.27	3.40	5.51	8.02
			max-min	1.57	0.61	0.83	1.44	0.27	1.09	0.59	0.57	0.22	0.22
LFe		27	average	48.53	1.09	8.65	20.72	0.42	9.43	6.50	3.28	0.53	0.84
			stdev	0.85	0.14	0.23	0.88	0.07	0.33	0.16	0.17	0.05	0.05
			max	49.93	1.48	9.23	22.46	0.55	10.08	6.81	3.64	0.65	0.92
			min	47.19	0.87	8.10	19.01	0.27	8.87	6.19	3.04	0.46	0.73
			rstdev	1.80	16.48	2.87	4.62	26.07	3.77	2.55	5.62	11.00	6.94
			max-min	2.73	0.61	1.13	3.45	0.28	1.21	0.62	0.60	0.19	0.19
IAMB.S5	0.88	40	average	53.53	1.04	9.26	16.56	0.34	8.20	5.81	3.77	0.78	0.71
			stdev	2.69	0.16	0.34	2.03	0.08	0.72	0.48	0.30	0.14	0.07
			max	56.01	1.38	9.81	20.74	0.49	9.73	6.89	4.14	0.94	0.85
			min	48.43	0.79	8.47	14.78	0.19	7.40	5.26	2.84	0.47	0.58
			rstdev	5.56	19.69	4.07	13.70	40.89	9.75	9.18	10.59	29.78	11.77
			max-min	7.59	0.60	1.34	5.96	0.31	2.33	1.63	1.30	0.48	0.28
LSi		30	average	55.05	0.99	9.41	15.43	0.32	7.81	5.54	3.89	0.86	0.69
			stdev	0.41	0.13	0.22	0.36	0.07	0.25	0.13	0.24	0.03	0.05
			max	56.01	1.28	9.81	16.32	0.44	8.25	5.77	4.14	0.94	0.77
			min	54.01	0.79	8.78	14.78	0.19	7.40	5.26	2.84	0.80	0.58
			rstdev	0.76	16.54	2.50	2.43	36.71	3.35	2.47	8.28	4.17	8.03
			max-min	2.00	0.49	1.02	1.54	0.26	0.85	0.51	1.30	0.15	0.20
LFe		10	average	48.98	1.18	8.81	19.97	0.38	9.35	6.60	3.39	0.55	0.80
			stdev	0.37	0.14	0.23	0.44	0.09	0.33	0.14	0.07	0.04	0.03
			max	49.56	1.38	9.25	20.74	0.49	9.73	6.89	3.48	0.58	0.85
			min	48.43	0.99	8.47	19.35	0.23	8.83	6.35	3.28	0.47	0.73
			rstdev	0.77	13.92	2.66	2.28	37.45	3.69	2.24	2.18	7.51	4.59
			max-min	1.13	0.40	0.78	1.39	0.26	0.89	0.54	0.20	0.11	0.12

Table 4.7: Continuation

Sample	FeO/FeO _{tot}	N		SiO ₂	TiO ₂	Al ₂ O ₃	FeO _{tot}	MnO	MgO	CaO	Na ₂ O	K ₂ O	P ₂ O ₅
OMB				46.72	0.56	10.61	18.99	0.11	11.39	8.41	2.25	0.17	0.79
OMB-S1	0.23	16	average	45.23	0.56	10.34	21.04	0.12	11.04	8.27	0.20	2.61	0.60
			stdev	0.44	0.04	0.17	0.61	0.04	0.24	0.27	0.04	0.13	0.06
			max	46.17	0.60	10.68	23.12	0.20	11.56	8.52	0.29	2.82	0.71
			min	44.45	0.49	10.13	20.40	0.05	10.42	7.36	0.15	2.33	0.50
			rstdev	1.00	7.25	1.69	2.97	88.86	2.26	3.70	23.63	5.72	12.01
			max-min	1.72	0.11	0.55	2.72	0.15	1.14	1.16	0.14	0.50	0.20
OMB-S2	0.50	19	average	49.41	0.55	10.84	17.14	0.10	10.18	7.87	0.25	3.10	0.56
			stdev	4.16	0.05	0.52	3.39	0.05	1.17	0.67	0.09	0.57	0.07
			max	58.50	0.64	11.79	20.63	0.20	11.32	8.59	0.45	4.34	0.67
			min	45.33	0.46	10.05	10.37	0.02	7.35	6.25	0.14	2.45	0.43
			rstdev	9.18	11.98	5.14	32.71	230.82	15.95	10.73	65.15	23.43	16.86
			max-min	13.17	0.18	1.74	10.26	0.18	3.97	2.34	0.32	1.89	0.24
OMB-S3	0.50	15	average	46.38	0.57	10.49	19.73	0.11	10.99	8.27	0.20	2.67	0.60
			stdev	0.56	0.04	0.16	0.51	0.04	0.15	0.15	0.03	0.14	0.06
			max	47.35	0.62	10.75	20.55	0.18	11.28	8.49	0.25	3.01	0.72
			min	45.29	0.50	10.28	18.81	0.05	10.72	7.97	0.14	2.46	0.48
			rstdev	1.23	7.30	1.59	2.73	88.21	1.39	1.86	24.30	5.54	12.78
			max-min	2.06	0.12	0.47	1.73	0.13	0.57	0.51	0.11	0.55	0.23
OMB-S4	0.80	18	average	47.35	0.55	10.75	18.46	0.11	11.04	8.21	0.19	2.73	0.60
			stdev	0.65	0.04	0.14	0.46	0.04	0.16	0.12	0.05	0.11	0.06
			max	48.85	0.63	11.06	18.92	0.17	11.31	8.45	0.26	2.94	0.68
			min	46.62	0.45	10.56	17.52	0.06	10.71	8.01	0.09	2.43	0.47
			rstdev	1.40	8.57	1.36	2.62	61.23	1.52	1.54	50.39	4.53	11.71
			max-min	2.23	0.18	0.50	1.40	0.11	0.60	0.44	0.17	0.51	0.20
Sample		N		SiO ₂	TiO ₂	Al ₂ O ₃	FeO _{tot}	MnO	MgO	CaO	Na ₂ O	K ₂ O	P ₂ O ₅
YMB				43.38	0.68	10.28	21.19	0.14	11.73	8.20	3.03	0.25	1.13
YMB-S1	-	40	average	42.69	0.68	10.11	21.77	0.15	10.98	8.72	3.60	0.27	1.03
			stdev	0.38	0.13	0.29	0.50	0.06	0.34	0.23	0.14	0.04	0.09
			max	43.34	0.89	10.91	23.07	0.26	11.79	9.25	3.93	0.35	1.26
			min	41.62	0.37	9.43	20.85	0.05	10.44	8.17	3.32	0.18	0.84
			rstdev	0.92	34.52	3.12	2.38	119.88	3.22	2.80	4.34	24.71	10.58
			max-min	1.72	0.52	1.47	2.22	0.21	1.35	1.08	0.62	0.17	0.42
YMB-S2	-	31	average	43.33	0.69	10.11	21.21	0.14	10.86	8.64	3.74	0.28	1.01
			stdev	0.68	0.12	0.34	0.54	0.06	0.37	0.21	0.12	0.03	0.10
			max	44.63	0.96	10.96	22.41	0.28	11.67	9.26	3.98	0.35	1.25
			min	41.85	0.46	9.41	20.31	0.01	10.01	8.28	3.52	0.22	0.82
			rstdev	1.62	25.23	3.60	2.65	519.89	3.70	2.59	3.35	14.79	12.08
			max-min	2.78	0.50	1.56	2.09	0.26	1.66	0.98	0.47	0.13	0.42
YMB-S3	-	41	average	46.07	0.64	10.42	18.47	0.14	10.36	8.40	4.17	0.33	1.01
			stdev	2.03	0.12	0.38	1.78	0.06	0.60	0.41	0.42	0.07	0.08
			max	49.39	0.93	11.21	21.53	0.26	11.48	9.10	4.74	0.46	1.20
			min	42.35	0.43	9.68	15.92	0.00	9.25	7.49	3.40	0.20	0.84
			rstdev	4.80	27.00	3.91	11.19	#DIV/0!	6.50	5.44	12.34	33.57	9.40
			max-min	7.05	0.50	1.53	5.62	0.26	2.23	1.60	1.34	0.26	0.36
YMB-S4	-	27	average	43.99	0.70	10.30	19.85	0.15	11.08	8.93	3.66	0.28	1.04
			stdev	0.73	0.12	0.28	0.50	0.06	0.36	0.26	0.09	0.03	0.09
			max	45.13	0.94	10.92	20.66	0.31	11.94	9.35	3.90	0.33	1.23
			min	42.46	0.43	9.67	18.87	0.02	10.45	8.44	3.46	0.19	0.81
			rstdev	1.73	27.30	2.85	2.63	349.11	3.46	3.09	2.70	17.72	11.09
			max-min	2.67	0.50	1.25	1.79	0.29	1.49	0.91	0.44	0.14	0.42
YMB-S5	-	36	average	45.17	0.71	10.47	18.09	0.14	11.28	8.96	3.91	0.29	0.98
			stdev	0.87	0.12	0.34	0.77	0.07	0.37	0.22	0.09	0.04	0.10
			max	46.67	0.99	11.15	20.02	0.28	12.23	9.38	4.40	0.40	1.14
			min	43.18	0.49	9.87	16.57	0.02	10.70	8.59	3.37	0.21	0.80
			rstdev	2.01	23.47	3.44	4.66	332.73	3.46	2.51	6.60	20.44	12.61
			max-min	3.49	0.49	1.28	3.45	0.26	1.53	0.79	1.02	0.19	0.34

Table 4.7: Continuation

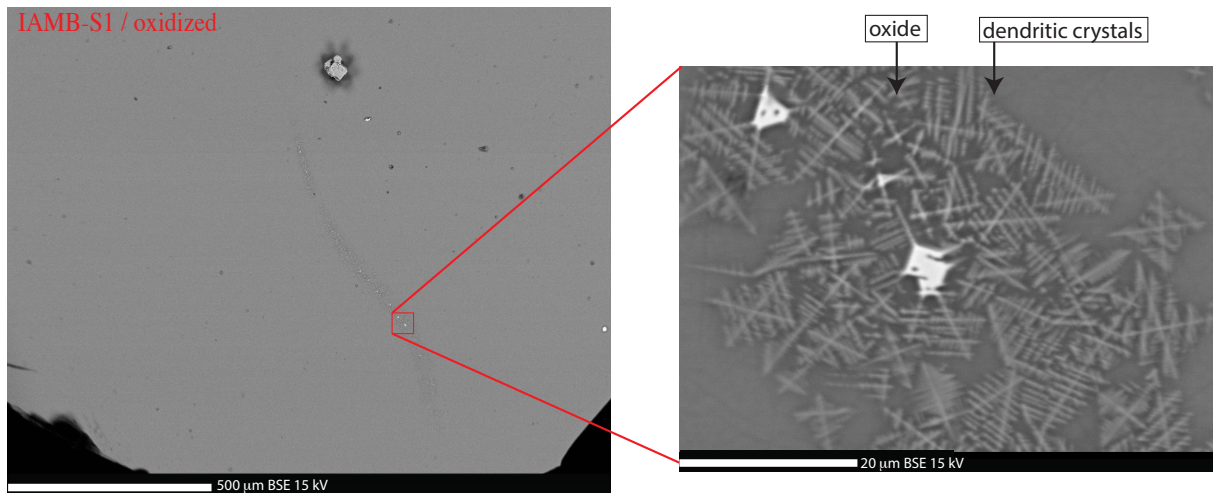


Figure 4.12: BSE images of IAMB-S1

SiO ₂	Al ₂ O ₃	TiO ₂	FeO	MnO	MgO	CaO	Na ₂ O	K ₂ O	P ₂ O ₅	Cr ₂ O ₃	Total
19.07	5.93	0.71	56.39	0.45	10.00	1.72	1.88	0.31	0.24	0.35	97.04
21.67	6.02	0.68	53.25	0.50	9.50	1.99	1.70	0.39	0.24	0.29	96.20

Table 4.8: Electron microprobe analyses of the crystals from Figure 4.12 (using same condition as previously stated in Table 4.7).

CHAPTER 5

Conclusion

The chemical compositions of Martian volcanic rocks so far analyzed are essentially basaltic and enriched in iron with respect to terrestrial basalts. In this work, the rheological properties of Martian lavas have been investigated from an experimental approach both above and below the liquidus temperatures. First, to better understand the effect of iron, and its redox state on rheology we experimentally studied the viscosity of the basaltic analogue anorthite-diopside composition with variable amount of iron. We showed that iron dramatically lowers silicate melt viscosity and glass transition temperatures by increasing depolymerisation and enhancing the non-Arrhenian behavior of the melt. The effect of its redox state indicates that ferrous iron acts as a network modifier by slightly decreasing the viscosity at superliquidus conditions (maximum of 0.2 log Pa·s). At a certain extend of iron reduction, the ferric and ferrous species structurally stabilize each other (around $\text{FeO} / \text{FeO}_{\text{tot}}=0.5$) and the viscosity remains constant under more reduced conditions. The difference in viscosity at magmatic temperatures between ‘common’ terrestrial basalts and iron-bearing composition is estimated to be 1 order of magnitude.

The viscosities of five synthetic silicate liquids having compositions representative of the diversity of Martian volcanic rocks were then experimentally measured under controlled oxygen fugacity. The results confirm the low viscosities of such Fe-rich compositions and although their viscosities at superliquidus temperature are lower than common terrestrial basalts, they are very similar to Fe-rich basaltic terrestrial and lunar lavas. Near the glass transition, the melt viscosity is more challenging to measure, however, estimates were obtained within reasonable error bars and a non-Arrhenian parameterisation of the Martian melts flow behavior is provided. Comparison with rheological empirical models reveals that the Giordano et al. (2008) model may be used to estimate the viscosity-temperature relationship of these compositions, at both super liquidus regime and near the glass transition. The Shaw (1972) model is suitable for only high temperature range, while the model of Hui and Zhang (2007) is not recommended as it shows large discrepancies with the experimental data.

In order to use the experimental data to draw quantitative conclusion on the rheological characteristic derived from the morphology of Martian lava flows, a terrestrial lava flow was used to describe the viscous behavior of lava as emplacement, cooling, and crystallization occur. The rheological analyses of samples taken along the flow reveal that the viscous behavior of lava flow is inevitably transient and flow viscosity increases by more than 6 orders of magnitude during emplacement. It is shown that the rheological properties obtained from morphological analyses of flow are only a late snapshot of the eruptive process corresponding to a rheological limit occurring when the crystals network jammed near flow cessation. This rheological limit is highly dependent on the details of

the crystallization sequence and crystal shapes, and as such, is not uniquely and simply related to the bulk chemical composition of the erupted material.

Finally, these steps offer a framework to interpret the range of inferred viscosities from lava flow morphology observed on Mars regarding to the diversity of chemical compositions observed from the orbit or in-situ measurement. The estimation of the apparent viscosity of crystallizing Martian lavas reveal that the range of viscosity inferred from the morphology appears to be entirely consistent with the range of known compositions. Low apparent viscosity range (10^2 - 10^4 Pa·s) inferred from lava flow morphology may be attributed to komatiite-like lava flows of primary mantle melt composition (Hesperian or Amazonian type) possibly forming spinifex texture. High viscosity values (10^6 - 10^8 Pa·s) are compatible with mildly alkaline or trachy basalts (that have been documented at landing sites and are consistent with dry fractionation of theoleiitic basalts) and do not necessarily imply the occurrence of silica-rich lavas (e.g., andesitic). The evolution of the chemical composition of primary melts through time does not lead to major viscosity variations and therefore observation of lava flow with different apparent viscosity cannot be characteristic of their age. The low viscosity of iron-rich basaltic melts would facilitate the transport of magma through the crust and appear to be the key parameter to understand the abundance of primitive magmas at the surface.

CHAPTER 6

Outlook

⇒ Extension of model for silicate melts viscosity: A direct application of our experimental viscosity measurements is to achieve an update of the Giordano et al. (2008) model to improve its ability to predict the viscosity of extra-terrestrial magmas. Although this model is able to predict the viscosity-temperature relationship of Martian basalts, large discrepancies remain for Fe-Ti-rich lunar basalts (see Annex 2). Such a work has already been initiated and consists in an optimization of the fitting parameters and coefficient for calculation of the TVF parameters from a database both including our experimental results and a compilation of lunar lava viscosity data (see Annex 2).

⇒ Structural configuration of iron in silicate melts: The decrease of viscosity with reduction of iron correlates with an increase of depolymerisation. This suggests that ferric iron acts as network former while ferrous iron acts as network modifier. In contrast, the invariant viscosity after further reduction than $\text{Fe}^{2+}/\text{Fe}_{\text{tot}} = 0.5$ hints that iron may develop different coordination state under reducing conditions. The investigation of the structural configuration of iron on the Martian melts has already started via Mössbauer spectroscopy and further Raman spectroscopy or X-ray absorption Near Edge Structure could also be considered.

⇒ Viscosity of crystallizing lavas: The viscous behavior of crystallizing lava has been described here by a combination of rheological and thermodynamic models. The rheological models provide a static view on the individual contributions of chemical composition of the interstitial liquid and the physical effects of the suspended phases, without consideration of the feedback involved in the thermodynamic process; while the thermodynamic calculators provide a steady state perspective of mineral assemblage, disregarding kinetic information of the physical evolution of the system during crystallization. To strengthen the adequacy of combining such rheological and thermodynamic models in a transient system such as lava flow dynamics, in-situ rheological experiments must be conducted on crystal-bearing lavas. Viscosity measurements may be achieved to describe the viscous path of lava as cooling and crystallization occurs. Such method has been recently optimized with the master thesis of Lea deBiasi and viscosity measurements on crystal-bearing Icelandic sample have already show successful results. The next step would be to measure the viscosity of crystallizing Martian basalt under various undercooling temperature and cooling rate.

⇒ Farther experimental investigation of Martian lavas: To improve our predictions of magma behavior during ascent, emplacement as intrusive bodies or lava flows emplacement, more experiments can be conducted on the synthetic Martian samples. The melt density at superliquidus temperature could be measured with the Archimedean method for an accurate determination of the buoyancy forces. Knowledge of thermal properties is also critical to estimate the thermal history of magma during their ascent. For

this purpose, the temperature-dependence of thermal diffusivity could be measured using laser-flash analysis (on going discussion with Allan Whittington, University of Missouri).

⇒ Effect of volatiles: The effect of volatiles on the viscosity of Martian melts has not been discussed here but must be integrated in future studies. Changes in rheology due to gas loss, and associated quenching and crystallization of the lava strongly influence magma ascent as well as the type of eruption and lava flow morphology. Evidences obtained from in-situ rock analysis suggest the presence of volatile rich rock (H_2O , CO_2 , Cl, S) and the presence of volcanoclastic deposits involves the presence of explosive volcanism. The explosivity of Martian magmas requires to be investigated. Moreover, knowing that Mars' mantle may have experienced a global devolatilisation, the influence of such event on volcanism might be observed on the history of Martian volcanism.

⇒ Volcanology in-situ on Mars: The previous and current missions to Mars have always focused on the research of water. The landing site and exploration area of the rovers were always selected because of geological evidence for past aqueous activity (ancient flood plain, fluvial lacustrine deposits, stratified materials, phyllosilicates or sulfates, lake bed, river channels, depositional fans, etc...). During these missions, the rovers have chemically analyzed floating rocks found randomly on the surface of the planet near their landing site. Although most of these rocks were recognized to be of volcanic origin (effusive and explosive deposit) or from dyke, no mission has focused principally on the volcanic activity. Future mission to Mars could envisage to land in a volcanic province where lava flows and volcanoes were formerly observed and described. Complete chemical and petrographic description of collected sample in-situ on a lava flow or on a volcanic edifice would enhance our understanding of eruption and magma emplacement on Mars.

⇒ Multidisciplinary approach: The method of combining morphological, rheological and petrological observation as described in Chapter 3 is essential to fully describe the flow behavior of magma during ascent and surface emplacement. We recommend that such comparative approach should be used for a wider range of compositions (extended toward more evolved lavas) and largely applied to terrestrial flow to better understand the complex behavior of extra-terrestrial lava flows. In particular, in the case of more silicic lava flows and domes (andesitic or rhyolitic) where the rheological evolution is not so intensely dependent on crystallization occurring after eruption but rather on strain-rate, cooling rate and glass transition temperatures. The non-unique rheological/petrological path evolution of such magma may be investigated to improve our ability at better recognizing the type of lavas. In this regard, such approach may now be used for example on Venus where the composition and origin of the observed domes at the surface is still under debate.

CHAPTER

7

**Annex 1: Detailed experimental
methods**

This extra chapter is to describe in detailed the experimental methods that I used during the PhD.

Sample preparation

Samples comprise both natural and synthetic material. Natural samples were collected on the field directly on the lava flow and were chosen with minimum alteration. Back in the lab, they were dried and cut to make thin sections and about 100 g was crushed into powder.

Synthetic samples are made by mixing the desired amount of pure oxide and carbonate powders (SiO_2 , TiO_2 , Al_2O_3 , Fe_2O_3 , MgO , MnO , P_2O_5 , CaCO_3 , Na_2CO_3 , K_2CO_3 and NaH_2PO_4). The powders are always kept dried prior weighing. To ensure a good mixing, the batches are homogenized using an agate mortar in acetone for at least 30 min.

The powders (either the crushed natural rock or the mixed powders) are fused in air at 200 °C above the liquidus within in a $\text{Pt}_{80}\text{Rh}_{20}$ crucible for 2 hours in a MoSi_2 -heated, ZrO_2 -lined, box furnace (Nabertherm®). The resulting melts are poured onto a copper plate for quenching and are re-melted a second time. The samples are then transferred into a vertical furnace equipped with a rotational viscometer and stirred for at least two hours using a $\text{Pt}_{80}\text{Rh}_{20}$ spindle to insure perfect homogenization and absence of bubble before any viscosity measurement. The platinum crucibles and spindle are previously doped with iron to minimize the propensity of iron into the crucible wall. After homogenization, the melt are sampled and the composition of the resulting glass is analyzed with wavelength dispersive Electron MicroProbe Analyser (see section Analytical analysis).

High temperature viscometry

Concentric cylinder: principle

The concentric cylinder device, based on the Couette method, is used to measure the viscosity of a molten rock (Shaw, 1969; Dingwell, 1986). The molten material is contained in a cylindrical crucible (outer cylinder) and undergo a constant strain-rate that is applied by a rotating cylindrical spindle inserted in the melt (inner cylinder). The shear stress sustained in the melt is record as a torque exerted by the liquid on the spindle. The Newtonian viscosity of the liquid is define by:

$$\eta = \frac{\sigma}{\dot{\gamma}} \quad (7.1)$$

where η is the viscosity of the melt, σ is the stress sustained by the melt, $\dot{\gamma}$ is the strain rate applied by the rotating spindle. Stress and strain rate can can be calculated using

the following relationships:

$$\sigma = \frac{M}{(2\pi R_i^2 h)} \quad (7.2)$$

$$\dot{\gamma} = \frac{2\Omega}{n \left(1 - \left(\frac{R_i}{R_o} \right)^{\frac{2}{n}} \right)} \quad (7.3)$$

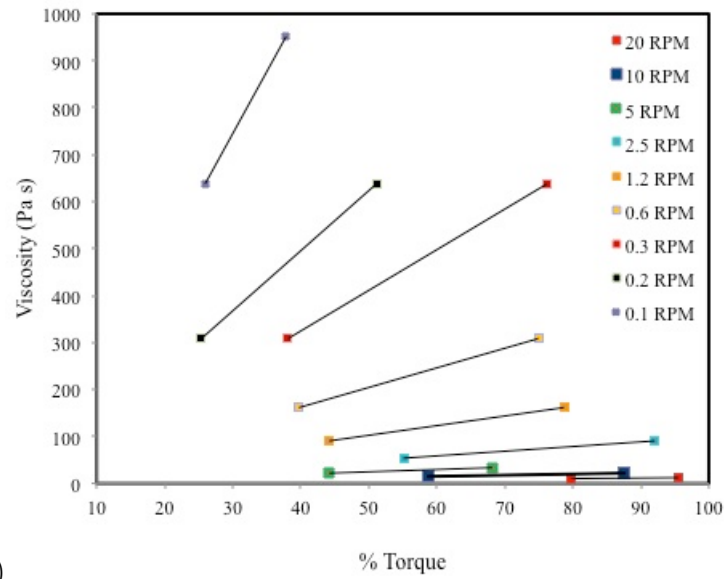
where M is the measured torque; R_i and R_o are the radius of the inner and outer cylinders, respectively; h is the effective immersed length of the spindle; Ω is the angular velocity (rad/s) and n the flow index that is equal to 1 for Newtonian liquid. The outer crucible used for the measurements is 5 cm high and has a diameter of 2.5 cm (inner wall). Depending on the melt viscosity, one of two types of Pt₈₀Rh₂₀ spindles may be used: for low-viscosity, the spindle has a diameter of 1.44 cm, a length of 3.32 cm and conical ends 45°(to reduced end effect) and for high-viscosity, the spindle has a smaller diameter of 0.24 cm and a length of 4.63 cm. For convenience, and in case of imperfection of the assembly geometry, the spindle/crucible pair is calibrated using the standard glass from the Deutschen Glasindustrie, DGG1, for which the viscosity-temperature relationship is accurately known. The torque may be converted directly to viscosity for a given speed (Figure 7.1a). The absolute viscosity obtained by calculation using Eq. 7.1, 7.2 and 7.3, and by calibration shows very good agreement (Figure 7.1b).

Furnaces

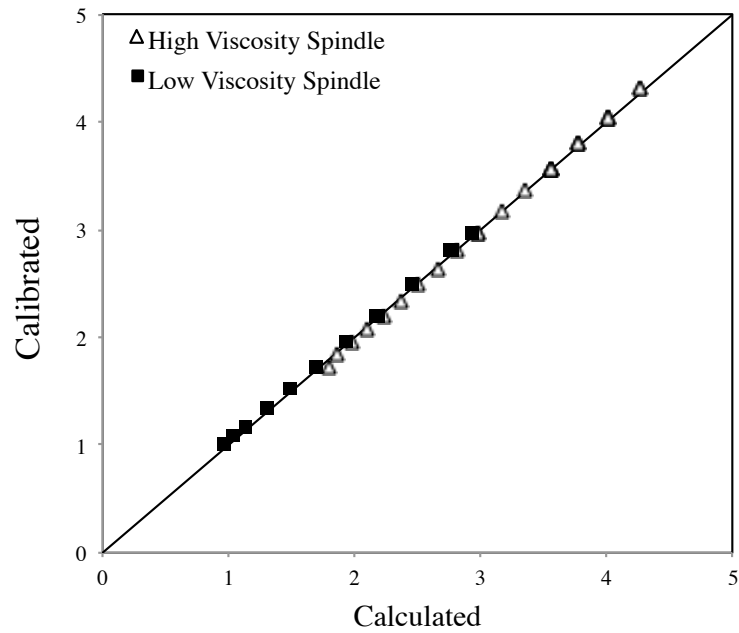
A classic box furnace (MoSi₂-heated, ZrO₂-lined) which is open at the top is used for experiments performed in air. The experiments under reduced oxygen fugacity were performed using a vertical tube furnace heated by MoSi₂ elements equipped with a gas-tight alumina muffle tube and a CO-CO₂ gas-mixing line (flow rate of 20 cm³.min⁻¹). The ambient oxygen fugacity in the furnace was fixed by controlling the furnace atmosphere at air, pure CO₂ and several CO:CO₂ mixing ratio (Dingwell and Virgo, 1987). The top of the furnace is fitted with an iris diaphragm to allow the spindle to pass through and the crucible was supported in the “hot zone” of the furnace by an alumina pedestal. The oxygen fugacity was monitored with a differential voltmeter linked to a yttria-stabilized zirconia oxygen sensor placed just below the crucible (Figure 7.2). The differential voltage is converted into oxygen fugacity via a the Nernst equation:

$$E = \frac{2.303RT}{4F} \log \left(\frac{fO_2}{fO_{ref}} \right) \quad (7.4)$$

where E is the differential potential (volts), R is the universal gas constant (J.K⁻¹.mol⁻¹), T is the temperature (K), F is the faraday constant (C.mol⁻¹), fO_2 is the fugacity in the



a)



b)

Figure 7.1: a) Calibration of the viscosity a function of the % torque for a given speed b) viscosity calculated using Eqs. 7.1, 7.2 and 7.3 versus viscosity obtained by calibration

system and $f_{O_{ref}}$ is the fugacity of the ambient air (= 0.205437).

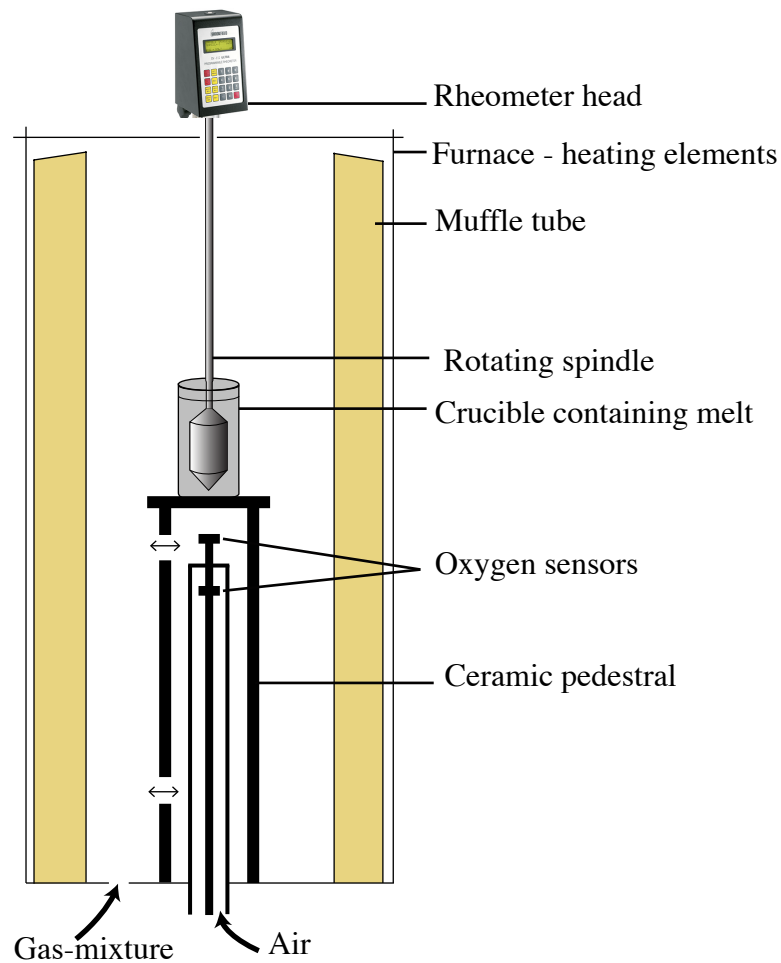


Figure 7.2: Scheme of the gas-tight vertical tube furnace

Temperature calibration

The sample temperature is determined by the immersion into the melt of a Pt/Rh₃₀-Rh₆: B-type thermocouple (shielded by a platinum sheath). The temperature gradient within the crucible was checked vertically and does not exceed 2 °C. The relationship between the temperature given by the furnace and the temperature of the immersed thermocouple is established for an immersion of 2.5 cm over a large temperature range (Figure 7.3).

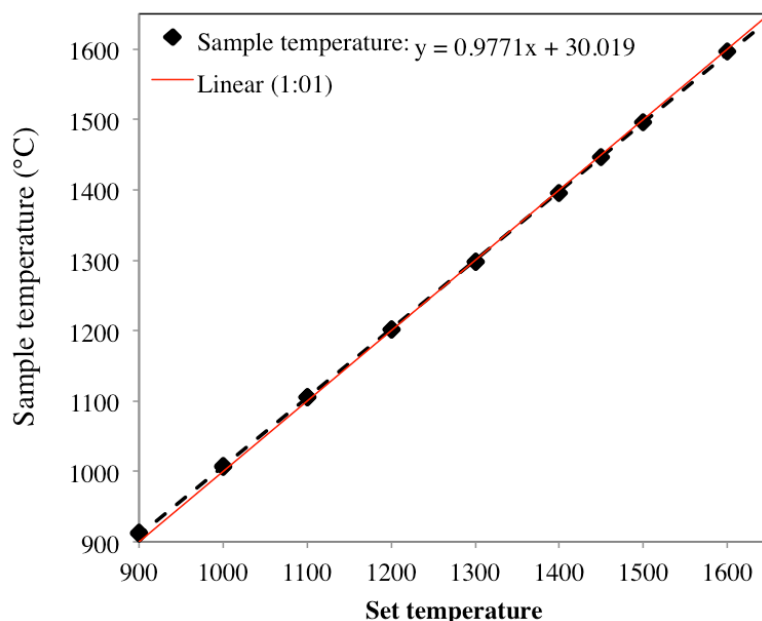


Figure 7.3: Example of temperature calibration for the box furnace at a thermocouple immersion of 2.5 cm.

Data measurement and acquisition

The rheometer head is a Brookfield® DV-III Ultra RVTD (Rotary Variable Transducer Displacement) with a full range torque of 7.2×10^{-4} N.m that drives the spindle, at constant angular velocities between 0 to 40 rotations per minute (rpm). The viscosity is recorded at every 25 °C decreasing temperature increments from 200 K above the liquidus until crystallization occurs. Possible instrumental drift was checked by reoccupation of the highest temperature data-point at the end. Several oxidation states were achieved by changing the CO₂:CO ratio and for each new oxygen fugacity at least 24 hours was required to permit melt equilibration (i.e., time invariant viscosity record).

The raw data (% torque, rpm, temperature, voltage) are continuously acquired and record at every second using a new home-made software (ViscosityLaumann; Figure 7.4). The extracted viscosity values correspond to an average of minimum 10 minutes of stable torque (variation of 0.1 % torque) after one hour at isothermal equilibrium.

Sampling Technique

Sampling is performed at isoviscous condition by a “dip quenching technique”. This techniques consists in inserting and removing an alumina rod (with a diameter of 3 mm) into the liquid forming a melt droplet on the rod tip that is then fast quenched into a water bucket. The process lasts less than 15 s and the melt cooling rate is then estimated to be ~ 100 °C/s. This fast cooling causes the glass to fragment into powder and tens of

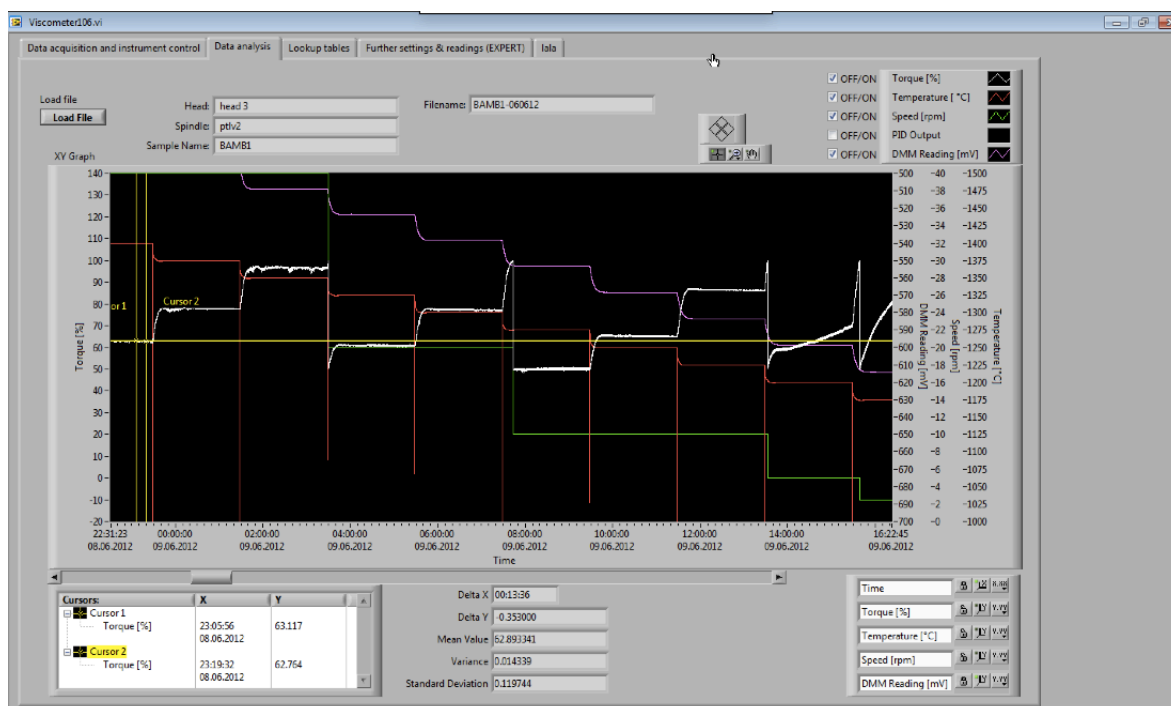


Figure 7.4: Screen caption of the interface of the ViscosityLauman software

small chips (< 10 mg) that were used for further analyses (chemical analyses, redox state titration, calorimetric measurements). Due to the very iron-rich compositions, although the action is performed as quickly as possible, some melts may have undergone some oxidation, crystallization or phase separation during the process.

Low temperature viscometry

Micro-penetration

Some low-temperature viscosities were measured using the micropenetration technique. This involves determining the rate at which an hemispherical Ir indenter under a fixed load moves into the melt surface. The measurements were accomplished near the glass transition temperature using a vertical pushrod Bähr 802 V dilatometer (Hess et al., 1995 and reference within). The sample (with polished parallel surfaces) is placed in a silica rod holder under an Ar gas flow and the indenter is attached above it to a calibrated linear voltage displacement transducer. The movement as the indenter is pushed into the melt yields a displacement during a certain time that is then converted into viscosity.

Only few samples that could be quenched into stable glass sufficiently large were measured using this technique (sample with less than 10 wt. % FeO_{tot}). Because working with iron is difficult to quench big peace of glasses needed to performed this technic, we used instead calorimetry to evaluate the viscosity a low temperature (see next section).

Calorimetry

The calorimetric measurements are performed using a Differential Scanning Calorimeter (DSC 404 Pegasus from NETZSCH® Gerätebau). The samples used here were small glass chips (of maximum 50 mg) that resulted from the dip quench technique after viscosity measurements. After initial heating into the liquid field (i.e., approximately 50 K above the glass transition temperature), the sample sustained cycles of cooling and subsequent heating at fixed rate of 25, 20, 15, 10 and 5 K/min. For each sample and each rate, individual heat capacity (CT_p) curves were measured against a sapphire of the same weight. The time spent above the glass transition was kept to the minimum to reduce the occurrence of crystallization or oxidation. The reproducibility of the run and instrument deviation lead to a temperature deviation of ± 3 °C. The temperature associated to the

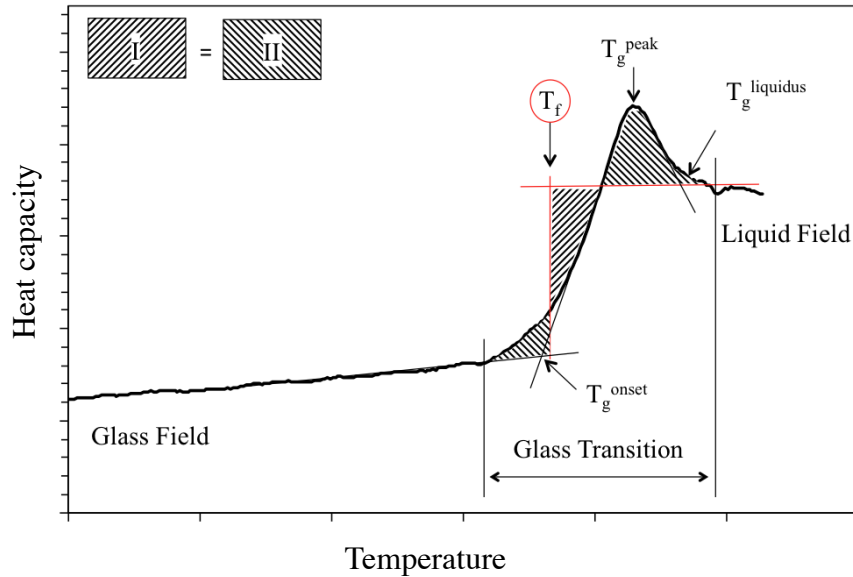


Figure 7.5: Method to collect T_g values at the onset, peak, liquid position and T_f' according to (Moynihan, 1995).

relaxation time at which the structure of the liquid is frozen in is define as limiting fictive temperature (T_f'). It is defined as the extrapolated intersection of the liquid and glass properties with'in the glass transition interval. A Matlab code was develop to smooth possible little wiggling of the curves and to collected temperature at the onset of the peak (T_g^{onset}), at the maximum value of the peak (T_g^{peak}) and at the onset of the stable liquid heat capacity (T_g^{liquidus}); and to estimate the limiting fictive temperature (T_f') according to the method developed by Moynihan, 1995 (Figure 7.5).

Analytical analysis

Chemical composition analysis

Glass chips resulting from the experiments were mounted as polished sections for petrographic and chemical analysis carried out with a CAMECA SX 100 Electron MicroProbe Analyser (EMPA) at the University of Munich.

The accelerating voltage was 15 kV and a defocused beam of $5\mu\text{m}$ was used with a current of 5 nA. The counting time was 10 s for Si, Al, K, Na, P, Cl and 30 s for Ca, Fe, Mg, Mn, Ti and half this time for the background (according to the protocol established by M. Scherer, Master Thesis). The standards used were Wallastonite for Si and Ca, Albite for Al, Ilmenite for Ti, Hematite for Fe, Periclase for Mg, Ilmenite for Mn, Albite for Na, Orthoclase for K, Apatite for P and Vanadinit for Cl. The data were corrected according to the PAP procedure (Pouchou and Pichoir, 1985).

Iron redox state: potassium dichromate titration

The potassium dichromate titration is an analytical technique to determinate the amount of Fe^{2+} in a sample. In combination with microprobe analysis, $\text{Fe}^{2+}/\text{Fe}_{\text{tot}}$ ratio can be estimate for each investigated glasses. This method is based on a simple potentiometric titration and necessitates only a very small amount of finely grounded powder (ca. 30 mg). The powder is dissolved into a large Teflon beaker with a known amount of sulphuric acid (H_2SO_4) and hydrofluoric acid (HF). The beaker is covered with a Teflon lid having two holes to permit inflow of CO_2 as a protection gas and outlet of evaporated acid and excessive protect gas. In order to accelerate the reaction the solution is positioned on a heating plate during 30 minutes. Once the dissolution is completed the solution is left cool down for about 10 minutes in a water bath. The beaker walls are then washed with deionized H_2O to collect any solution rests. Then 10 ml of boric acid (H_3BO_3) are added. The beaker is moved to the potentiometric device to be titrated with the potassium dichromate ($\text{K}_2\text{Cr}_2\text{O}_7$) oxidant (concentrated at $0.01\text{ mol}\cdot\text{dm}^{-3}$) at a rate of $1.00\text{ ml}\cdot\text{min}^{-1}$. All titration were performed at $20\text{ }^\circ\text{C}$ and the potential values were recorded automatically when the potential changes were within $\pm 2\text{ mV}\cdot\text{min}^{-1}$ for each additional. All potentiometric titrations were performed using a Dosimat® 665, Metrohm swiss automatic titrator. Finally values during titration were directly converted to Fe^{2+} concentration. The $\text{Fe}^{2+}/\text{Fe}_{\text{tot}}$ ratio is calculated from the total iron content obtained from EMPA measurements. As described in Bézou and Humler (2005) care has to be taken during the wet-chemistry procedure to avoid irreversible oxidation of ferrous iron. The standard deviation of the measurements was determined on ten titration measurements of the certified standard. (See Potuzac, PhD and Giuli et al al;, 2011 for further detailed)

CHAPTER 8

**Annex 2: Review of synthetic
lunar lava viscosity**

Data compilation

The first viscosity measurement of lunar material was performed by Murase and Mc Birney in 1970. They synthesised a typical Ti-Fe-rich lunar basalt collected on Apollo 11 site (SLSa) and measure the viscosity above the liquidus. They recorded the lowest viscosity values than any previously studied volcanic rock on Earth.

With the following Apollo missions, a NASA grant allowed to produce a substantial number of viscosity measurements on various lunar compositions (Table 8.1) including Fe-rich basalts, glass beads, Anorthosite, breccias and soil (Cukierman et al., 1972, 1973; Cukierman and Uhlmann, 1974; Uhlmann et al., 1974; Uhlmann and Klein, 1976; Klein et al., 1975; Uhlmann and Klein, 1976, 1977; Handwerker et al., 1977, 1978). All measurements were done using a rotating-cylinder viscometer for the superliquidus temperature range and bending-beam viscometer for high viscosity near the glass transition temperature range. Most of the sample were tested under low oxygen fugacity (5% H₂-forming gas) to simulate the Moon condition. We present here a compilation of all the data that could be found in the literature (Figure 8.3). In their articles the authors did not published the data in table but directly plotted in graphs. Owing to an adapted ruler (Software GraphClick) we could extract by hand point after point all the data and present them in Table 8.2. Note that we estimate the error due to printing quality and point picking involves on temperature to be maximum 10 ° C and of 0.5 log Pa s for the viscosity.

Samples		Ref	SiO ₂	TiO ₂	Al ₂ O ₃	FeO _{tot}	MnO	MgO	CaO	Na ₂ O	K ₂ O	Total
SLSa	Ti-rich basalt	1	43.0	11.0	7.7	21.0	0.3	6.5	9.0	0.4	0.2	99.1
14310	KREEP basalt	2	50.0	1.3	20.0	7.7	0.0	8.0	11.0	0.6	0.5	99.1
14259	KREEP soil	2	48.0	1.8	18.0	10.0	0.0	9.2	11.0	0.5	0.5	99.0
15555	Primitive basalt	3	44.2	2.3	8.5	22.5	0.3	11.2	9.5	0.0	0.0	98.5
68502	Highland soil	3	45.8	0.4	27.3	5.0	0.3	5.3	15.3	0.0	0.0	99.4
65016	Al-rich glass vitrophyres	4	44.2	0.6	26.5	5.5	0.0	7.3	15.3	0.4	0.1	99.9
60095	Large Al-rich glassy object	4	46.4	0.0	23.5	6.9	0.0	10.5	12.1	0.0	0.8	100.2
Green Glass	Green Glass	4	45.2	0.5	7.4	20.3	0.0	18.1	8.1	0.2	0.2	100.0
Anorthite liquide	Anorthosite	5	43.1	0.0	36.7	0.0	0.0	0.0	20.2	0.0	0.0	99.9
L24-1	Mare basalt	6	46.26	0.98	12.98	20	0	6.47	12.73	0.29	0.04	99.8
L24-2	Highland basalt	6	44.9	0.3	26.74	4.89	0.0	6.86	15.64	0.23	0.05	99.6
15286	Glass intrusion in breccia	7	46.1	1.6	14.3	14.2	0.0	12.5	10.4	0.8	0.0	99.9
15498	Glass in matrix of breccia	7	48.2	2.0	19.8	8.4	0.0	7.5	13.0	0.9	0.0	99.8

Figure 8.1: Composition of Lunar sample.(1) Murase and McBirney (1970); (2) Cukierman et al. (1972); (3) Cukierman et al. (1973) ; (4) Uhlmann et al. (1974); (5) Cukierman and Uhlmann, 1973c ; (6)Handwerker et al. (1978); (7) Uhlmann and Klein (1976)

Sample	Temperature (K)	Log viscosity (Pa s)	Ref	Sample	Temperature (K)	Log viscosity (Pa s)	Ref	
SLSa	1665	0.00	1	60095	1816	-0.09	4	
	1670	0.01	1		1794	-0.02	4	
	1719	-0.23	1		1766	0.05	4	
	1729	-0.27	1		1746	0.12	4	
1769	-0.33	1	1706		0.26	4		
14310	1677	0.75	2		1675	0.40	4	
	1637	0.96	2		1627	0.61	4	
	1614	1.06	2		1544	1.11	4	
	1590	1.21	2		1093	7.84	4	
	1564	1.40	2		1078	8.40	4	
	1544	1.53	2		1062	8.82	4	
	1097	8.07	2		1036	9.74	4	
	1076	8.49	2		1017	10.23	4	
	1059	8.96	2		999	11.00	4	
	1041	9.56	2	984	11.42	4		
	1041	9.35	2	959	12.47	4		
	1023	10.05	2	65016	1838	0.19	4	
	998	10.90	2		1809	0.26	4	
	974	11.69	2		1787	0.33	4	
14259	1658	0.70	2		1753	0.40	4	
	1615	0.89	2		1700	0.61	4	
	1569	1.16	2		1633	0.89	4	
	1524	1.48	2		1604	1.11	4	
	1482	1.92	2		1109	8.40	4	
	1429	2.43	2		1070	9.46	4	
	1421	2.53	2		1043	10.16	4	
	1090	8.17	2		1017	11.21	4	
	1081	8.55	2		995	11.77	4	
	1077	8.64	2		986	12.19	4	
	1067	8.94	2		971	12.75	4	
	1047	9.31	2	Anorthite liquide	1884	0.38	5	
	1045	9.18	2		1851	0.48	5	
	1037	9.41	2		1833	0.48	5	
1027	9.82	2	1807		0.64	5		
999	10.98	2	1785		0.75	5		
975	11.97	2	1760		0.96	5		
15555	1740	-0.42	3		1731	1.07	5	
	1719	-0.38	3		1214	8.33	5	
	1699	-0.29	3		1195	8.76	5	
	1669	-0.20	3		1165	9.87	5	
	1645	-0.07	3		1138	10.88	5	
	1622	0.02	3		1119	11.57	5	
	1604	0.11	3		1101	12.52	5	
	1569	0.29	3		L24-1	1642	0.461	6
	1531	0.64	3	1603		0.521	6	
	1511	0.69	3	1572		0.893	6	
	987	9.76	3	1543		0.993	6	
	974	10.20	3	1511		1.026	6	
	956	10.73	3	1456		1.259	6	
	945	11.22	3	1431		1.392	6	
934	11.71	3	1003	9.636		6		
930	11.89	3	979	10.5		6		
921	12.38	3	952	11.331		6		
912	12.64	3	L24-2	1805		0.468	6	
68502	1843	0.52		3		1764	0.538	6
	1775	0.69		3		1733	0.642	6
	1720	0.90		3		1695	0.816	6
	1694	1.03		3	1675	0.955	6	
	1654	1.20		3	1645	1.059	6	
	1626	1.41		3	1059	10.377	6	
	1606	1.49		3	1026	11.002	6	
	1586	1.79		3	994	11.663	6	
	1142	8.50		3	984	12.463	6	
	1132	8.75		3	15286	1595	0.093	7
	1111	9.34		3		1575	0.155	7
	1095	9.85		3		1558	0.187	7
	1080	10.40		3		1529	0.375	7
	1067	10.82	3	1477		0.686	7	
1052	11.45	3	1453	1.092		7		
1037	12.09	3	1422	1.342		7		
1022	12.59	3	1021	8.179		7		
GG	1787	-0.58	4	1002		8.803	7	
	1746	-0.58	4	998		9.053	7	
	1687	-0.44	4	983		9.553	7	
	1627	-0.23	4	968		10.115	7	
	1609	-0.23	4	956		10.614	7	
	1587	-0.09	4	937		11.457	7	
	1544	0.05	4	928	12.019	7		
	1518	0.19	4	15498	1639	0.655	7	
	1031	8.61	4		1590	0.905	7	
	1017	9.11	4		1570	1.061	7	
	995	9.74	4		1543	1.186	7	
	969	10.65	4		1520	1.279	7	
	945	11.35	4		1481	1.592	7	
	926	11.98	4		1445	1.748	7	
			1049		8.679	7		
			1044		8.929	7		
			1035		9.053	7		
			1021		9.49	7		
			1002		10.208	7		
			978		11.332	7		
			960		12.145	7		
			954	12.332	7			

Figure 8.2: Viscosity measurements collected from the literature.

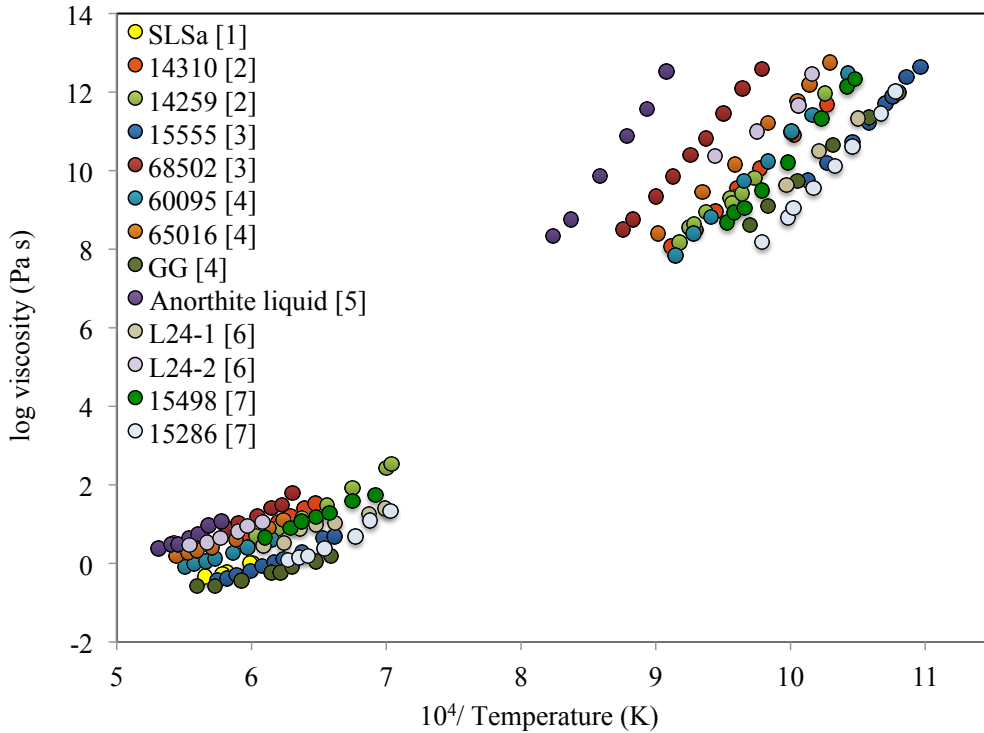


Figure 8.3: Viscosity measurements collected from the literature

Comparison with empirical model

The estimation of the viscosity-temperature relationship using the GRD model (Giordano et al., 2008), shows a relative good agreement for the Fe-rich basalts but very large discrepancies with the Al-rich or Ti-rich composition at both low and high temperature ranges.

The large discrepancy with the Fe-Ti-rich Apollo sample were so large that we have re-synthesized this sample and measure the temperature dependence of viscosity in our lab. Because we are interested in this study by the Fe-rich basalt, the green glass composition as well as the olivine basalt 15555 were also re-synthesized and measured. The methods for synthesis and viscosity measurement are exactly the same as describes for the Martian samples.

Figure 8.5 shows that our measurements are in good agreement with the previous studies, supporting the fact that the current GRD model is not suited for such Ti-rich composition and could be improved for Fe-rich compositions.

The combination of the literature data on the Lunar basalts and data on the Martian basalts provided by this study offers the possibility to use a larger set of samples to improve the empirical model of GRD (as suggested in the outlook).

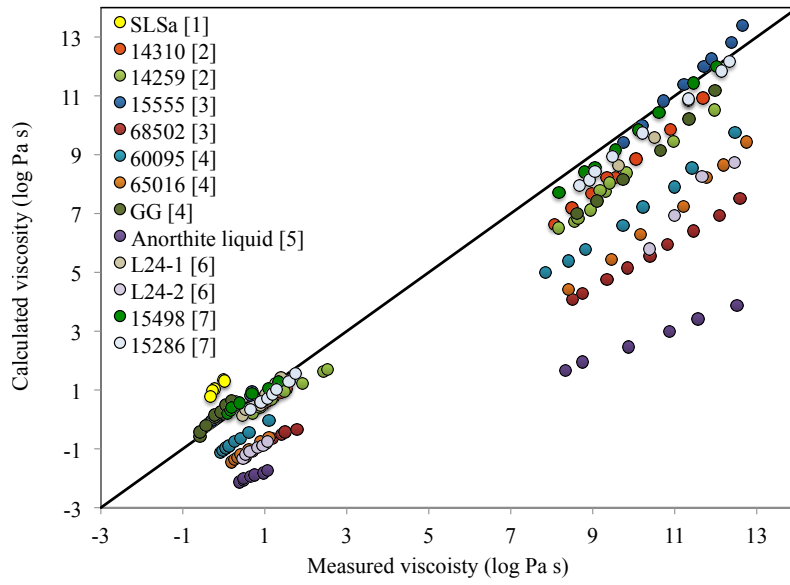


Figure 8.4: Comparison of the experimental data from the literature and estimation.

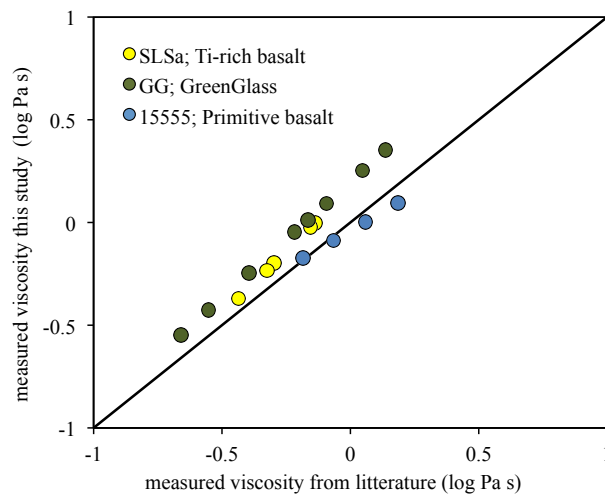


Figure 8.5: Comparison of literature data with synthesized and measured by this study.

Bibliography

- Adam, G., Gibbs, J., 1965. On the temperature dependence of cooperative relaxation properties in glass-forming liquid. *J. Chem. Phys.* 43, 139.
- Anderson, D.L., 1972. Internal constitution of Mars. *Journal of Geophysical Research* 77, 789–795.
- Angell, C., 1985. Strong and fragile liquids. *Relaxations in Complex Systems*. U.S. Department of Commerce National Technical Information Service, Springfield, VA , 3–11.
- Arndt, N., Naldrett, A., Pyke, D., 1977. Komatiitic and iron-rich tholeiitic lavas of Munro Township, Northeast Ontario. *Journal of Petrology* 18 part 2, 319–369.
- Bagdassarov, N., Dingwell, D.B., 1992. A rheological investigation of vesicular rhyolite. *Journal of Volcanology and Geothermal Research* 50, 307–322.
- Bagdassarov, N.S., Dingwell, D.B., Webb, S.L., 1994. Viscoelasticity of crystal-bearing and bubble-bearing rhyolite melts. *Phys. Earth Planet. Inter.* 83, 83,99.
- Baloga, S.M., Mouginis-Mark, P.J., Glaze, L.S., 2003. Rheology of a long lava flow at Pavonis Mons, Mars. *J. Geophys. Res.* 108, 5066.
- Bandfield, J.L., Hamilton, V.E., Christensen, P.R., 2000. A global view of martian surface compositions from mgs-tes. *Science* 287, 1626–1630.

- Baptista, A.R., Mangold, N., Ansan, V., Baratoux, D., Lognonné, P., Alves, E.I., Williams, D.A., Bleacher, J.E., Masson, P., Neukum, G., 2008. A swarm of small shield volcanoes on Syria Planum, Mars. *J. Geophys. Res.* 113, E09010.
- Baratoux, D., Pinet, P., Toplis, M.J., Mangold, N., Greeley, R., Baptista, A.R., 2009. Shape, rheology and emplacement times of small Martian shield volcanoes. *Journal of Volcanology and Geothermal Research* 185, 47–68.
- Baratoux, D., Toplis, M.J., Monnereau, M., Gasnault, O., 2011. Thermal history of Mars inferred from orbital geochemistry of volcanic provinces. *Nature* 472, 338–341.
- Baratoux, D., Toplis, M.J., Monnereau, M., Gasnault, O., 2013. The petrological expression of early Mars volcanism. *J. Geophys. Res.* doi:10.1029/2012JE004234.
- Barnes, H.A., 1999. The yield stress—a review or ‘panta roi’—everything flows? *J. Non-Newtonian Fluid Mech.* 81, 133–178.
- Bertka, C., Holloway, J., 1994. Anhydrous partial melting of an iron-rich mantle ii: primary melt compositions at 15 kbar. *Contrib. Mineral. Petrol.* 115, 323–338.
- Bézos, A., Humler, E., 2005. The Fe^{3+}/Fe ratios of MORB glasses and their implications for mantle melting. *Geochimica et Cosmochimica Acta* 69, 711–725.
- Binder, A., 1976. On the compositions and characteristics of the mare basalt and their source regions. *The Moon* 16, 115–150.
- Bost, N., Westall, F., Gaillard, F., Ramboz, C., Foucher, F., 2012. Synthesis of a spinifex-textured basalt as an analog to Gusev crater basalts, Mars. *Meteoritics and Planetary Science* , 1–12.
- Bottinga, Y., Weill, D., 1970. Density of liquid silicate systems calculated from partial molar volumes of oxide components. *American Journal of Science* 269(2), 169.
- Bottinga, Y., Weill, D.F., 1972. The viscosity of magmatic silicate liquids: A model for calculation. *Am. J. Sci.* 272, 438–475.
- Bouhifd, A., Richet, P., Besson, P., Roskosz, M., Ingrin, J., 2004. Redox state, microstructure and viscosity of a partially crystallized basalt melt. *Earth and Planetary Science Letters* 218, 31–44.
- Boynton, W.V., Taylor, G.J., Evans, L.G., Reedy, R.C., Starr, R., Janes, D.M., Kerry, K.E., Drake, D.M., Kim, K.J., Williams, R.M.S., Crombie, M.K., Dohm, J.M., Baker,

- V., Metzger, A.E., Karunatilake, S., Keller, J.M., Newsom, H.E., Arnold, J.R., Brückner, J., Englert, P.A.J., Gasnault, O., Sprague, A.L., Mitrofanov, I., Squyres, S.W., Trombka, J.I., d'Uston, L., Wänke, H., Hamara, D.K., 2007. Concentration of H, Si, Cl, K, Fe, and Th in the low- and mid-latitude regions of Mars. *Journal of Geophysical Research* 112.
- Brooks, C.K., Larsen, L.M., Nielson, T.F.D., 1991. Importance of iron-rich tholeiitic magmas at divergent plate margins: A reappraisal. *Geology* 19, 269–272.
- Byrne, P.K., van Wyk de Vries, B., Murray, J.B., Troll, V.R., 2009. The geometry of volcano flank terraces on Mars. *Earth and Planetary Science Letters* 281, 1–13.
- Caricchi, L., Burlini, L., Ulmer, P., Gerya, T., Vassalli, M., Papale, P., 2007. Non-Newtonian rheology of crystal-bearing magmas and implications for magma ascent dynamics. *Earth and Planetary Science Letters* 264, 402–419.
- Carignan, J., Hild, P., Mevelle, G., Morel, J., Yeghicheyan, D., 2001. Routine analyses of trace element in geological samples using flow injection and low pressure on-line liquid chromatography coupled to ICP-MS: a study of geochemical reference materials BR, DR-N, UB-N, AN-G and GH. *Geos. Newslett.* 25, 187–198.
- Carmichael, I.S.E., 1991. The redox states of basic and silicic magmas: a reflection of their source regions? *Contribution to Mineralogy and Petrology* 106, 129–141.
- Carr, M., James, W., 2010. Geologic history of Mars. *Earth and Planetary Science Letters* 294, 185–203.
- Cas, R., Self, S., Beresford, S., 1999. The behaviour of the fronts of komatiite lavas in medial to distal settings. *Earth and Planetary Science Letters* 172, 127–139.
- Castruccio, A., Rust, A.C., Sparks, R., 2010. Rheology and flow of crystal-bearing lavas: Insights from analogue gravity currents. *Earth and Planetary Science Letters* 297, 471–480.
- Chevrel, M., Giordano, D., Potuzak, M., Courtial, P., Dingwell, D., 2012. Physical properties of $\text{CaAl}_2\text{Si}_2\text{O}_8$ - $\text{CaMgSi}_2\text{O}_6$ - FeO - Fe_2O_3 melts: Analogues for extra-terrestrial basalt. *Chemical Geology in Press*, –.
- Christie, D., Carmichael, I., Langmuir, C., 1986. Oxidation states of mid-ocean ridge basalt glasses. *Earth and Planetary Science Letters* 79, 397–411.

- Cimarelli, C., Costa, A., Mueller, S., Mader, H.M., 2011. Rheology of magmas with bimodal crystal size and shape distributions: Insights from analog experiments. *Geochem. Geophys. Geosyst.* 12, Q07024.
- Cordonnier, B., Caricchi, L., Pistone, M., Castro, J., Hess, K.U., Gottschaller, S., Manga, M., Dingwell, D.B., Burlini, L., 2012. The viscous-brittle transition of crystal-bearing silicic melt: Direct observation of magma rupture and healing. *Geology* 40, 611–614.
- Costa, A., 2005. Viscosity of high crystal content melts: Dependence on solid fraction. *Geophys. Res. Lett.* 32, L22308.
- Costa, A., Blake, S., Self, S., 2006. Segregation processes in vesiculating crystallizing magmas. *Journal of Volcanology and Geothermal Research* 153, 287–300.
- Costa, A., Caricchi, L., Bagdassarov, N., 2009. A model for the rheology of particle-bearing suspensions and partially molten rocks. *Geochemistry Geophysics Geosystems* 10.
- Crisp, J., Cashman, K.v., Bonini, J.A., Hougén, S., Pieri, D., 1994. Crystallization history of the 1984 Mauna Loa lava flow. *Journal of Geophysical Research* 99, 7177–7198.
- Cukierman, M., Klein, L., Scherer, G., Hopper, R.W., Uhlmann, D.R., 1973. Viscous flow and crystallization behavior of selected lunar composition. *Geochimica et Cosmochimica Acta* 37, 2285–2696.
- Cukierman, M., Tutts, P.M., Uhlmann, D.R., 1972. Viscous flow behavior of lunar composition 14259 and 14310. *Geochimica et Cosmochimica Acta* 3, 2619–2625.
- Cukierman, M., Uhlmann, D.R., 1974. Effects of iron oxidation state on viscosity, lunar composition 15555. *Journal of Geophysical Research* 79, 1594–1598.
- Dingwell, D.B., 1986. Viscosity-temperature relationships in the system $\text{Na}_2\text{Si}_2\text{O}_5$ - $\text{Na}_4\text{Al}_2\text{O}_5$. *Geochimica et Cosmochimica Acta* 50, 1261–1265.
- Dingwell, D.B., 1991. Redox viscometry of some Fe-bearing silicate melts. *American Mineralogist* 76, 1560–1562.
- Dingwell, D.B., 1996. Volcanic dilemma flow or blow. *Science* 273, 1054–1055.
- Dingwell, D.B., 2006. Transport properties of magmas diffusion and rheology. *Elements* 2, 281–286.

- Dingwell, D.B., Brearley, M., 1988. Melt densities in the CaO-FeO-F₂O₃-SiO₂ system and the compositional dependence of the partial molar volume of ferric iron in silicate melts. *Geochimica et Cosmochimica Acta* 52, 2815–2825.
- Dingwell, D.B., Virgo, D., 1987. The effect of oxidation state on the viscosity of melts in the system Na₂O-FeO-Fe₂O₃-SiO₂. *Geochimica et Cosmochimica Acta* 51, 195–205.
- Dingwell, D.B., Virgo, D., 1988. Viscosities of melts in the Na₂O-FeO-Fe₂O₃-SiO₂ system and factors controlling relative viscosities of fully polymerized silicate melts. *Geochimica et Cosmochimica Acta* 52, 395–403.
- Dingwell, D.B., Webb, S., 1990. Relaxation in silicate melts. *Eur. J. Mineralogy* 2, 427–449.
- Dragoni, M., 1989. A dynamical model of lava flows cooling by radiation. *Bull. Volcanol.* 51, 88–95.
- Dreibus, G., Wänke, H., 1984. Accretion of the earth and the inner planets. *Geochemistry and Cosmochemistry*, 1–20.
- Dreibus, G., Wänke, H., 1985. Mars, a volatile-rich planet. *Meteoritics* 2, 367–381.
- Eason, D.E., Sinton, J.M., 2009. Lava shields and fissure eruptions of the Western Volcanic Zone, Iceland: Evidence for magma chambers and crustal interaction. *Journal of Volcanology and Geothermal Research* 186, 331–348.
- El Maarry, M., Gasnault, O., Toplis, M., Baratoux, D., Dohm, J., Newsom, H., Boynton, W., Karunatillake, S., 2009. Gamma-ray constraints on the chemical composition of the martian surface in the Tharsis region: A signature of partial melting of the mantle? *Journal of Volcanology and Geothermal Research* 189, 116–122.
- Elkins-Tanton, L.T., Hess, P.C., Parmentier, E.M., 2005. Possible formation of ancient crust on Mars through magma ocean processes. *Journal of Geophysical Research (Planets)* 110(E9), E12S01.
- Eyring, H., Henderson, D., Stover, B., Eyring, E., 1982. *Statistical mechanics and dynamics*. John Wiley eds, Second edition, NY., 785.
- Fairen, A., Dohm, J., 2004. Age and origin of the lowlands of Mars. *Icarus* 168, 277–287.
- Farris, R.J., 1968. Prediction of the viscosity of multimodal suspensions from unimodal viscosity data. *Trans. Soc. Rheol.* 12, 281–301.
- Fink, J.H., Griffiths, R.W., 1992. A laboratory analog study of the morphology of lava flows extruded from point and line sources. *J. Volcanol. Geotherm. Res.* 54, 19–32.

- Fisk, M., Bence, A., J.-G, S., 1982. Major element chemistry of Galapagos rift zone magmas and their phenocrysts. *Earth and Planetary Science Letters* 61.
- Francis, D., Ludden, J., Johnstone, R., Davis, W., 1999. Picrite evidence for more Fe in Archean mantle reservoirs. *Earth and Planetary Science Letters* 167.
- Fulcher, G., 1925. Analysis of recent measurements of the viscosity of glasses. *J. Am. Ceram. Soc.* 8, 339–355.
- Garry, W.B., Zimbelman, J.R., Gregg, T.K.P., 2007. Morphology and emplacement of a long channeled lava flow near Ascræus Mons Volcano, Mars. *Journal of Geophysical Research* 112.
- Gay, E., Nelson, P., Armstrong, W., 1969. Flow properties of suspensions with high solid concentrations. *AIChE Journal* 15, 815–822.
- Gellert, R., Rieder, R., Anderson, R.C., Brückner, J., Clark, B.C., Dreibus, G., Economou, T., Klingelhöfer, G., Lugmair, G., Ming, D.W., Squyres, S.W., d'Huston, C., Wänke, H., Yen, A., Zipfel, J., 2004. Chemistry of rocks and soils in Gusev Crater from the Alpha Particle X-ray Spectrometer. *Science* 305, 829–832.
- Gellert, R., Rieder, R., Brückner, J., Clark, B.C., Dreibus, G., Klingelhöfer, G., Lugmair, G., Ming, D.W., Wänke, H., Yen, A., Zipfel, J., Squyres, S.W., 2006. Alpha Particle X-Ray Spectrometer (APXS): Results from Gusev crater and calibration report. *Journal of Geophysical Research* 111, E02S05.
- Ghiorso, M.S., Sack, O., 1995. Chemical mass transfer in magmatic processes IV. A revised and internally consistent thermodynamic model for the interpolation and extrapolation of liquid-solid equilibria in magmatic systems at elevated temperatures and pressures. *Contrib. Mineral. Petrol.* 119, 197–212.
- Gibson, S., Thompson, R., Dickin, A., 2000. Ferropicrites: geochemical evidence for Fe-rich streaks in upwelling mantle plumes. *Earth and Planetary Science Letters* 174, 355–374.
- Gill, R., 2010. *Igneous rocks and processes: A practical guide*. Blackwell Publishing .
- Giordano, D., Ardia, P., Romano, C., Dingwell, D., Di Muro, A., Schmidt, M., Mangiacapra, A., Hess, K.U., 2009. The rheological evolution of alkaline vesuvius magmas and comparison with alkaline series from the Phlegrean Fields, Etna, Stromboli and Teide. *Geochim. Cosmochim. Acta* 73, 6613–6630.

- Giordano, D., Dingwell, D.B., 2003. Non-Arrhenian multicomponent melt viscosity: a model. *Earth and Planetary Science Letters* 6556, 1–13.
- Giordano, D., Polacci, M., Longo, A., Papale, P., Dingwell, D.B., Boschi, E., Kasereka, M., 2007. Thermo-rheological magma control on the impact of highly fluid lava flows at Mt. Nyiragongo. *Geophysical Research Letters* 34.
- Giordano, D., Russell, J., 2007. A rheological model for glass forming silicate melts in the systems CAS, MAS, MCAS. *J. Phys. Condens. Matter* 19, 205148.
- Giordano, D., Russell, J.K., Dingwell, D., 2008. Viscosity of magmatic liquids: A model. *Earth and Planetary Science Letters* 271, 123–134.
- Giuli, G., Paris, E., Pratesi, G., Hess, K.U., Dingwell, D., Cicconi, M., Eeckhout, S., Fehr, K., Valenti, P., 2011. XAS determination of the Fe local environment and oxidation state in phonolite glasses. *American Mineralogist* 96, 631–636.
- Giuli, G., Paris, E., Pratesi, G., Koeberl, C., Cipriani, C., 2003. Iron oxidation state in the Fe-rich layer and silica matrix of Libyan desert glass: a high-resolution XANES study. *Meteoritics and Planetary Science* 38, 1181–1186.
- Glaze, L.S., Baloga, S.M., 2007. Topographic variability on Mars: Implications for lava flow modeling. *Journal of Geophysical Research* 112.
- Glaze, L.S., Baloga, S.M., Stofan, E.R., 2003. A methodology for constraining lava flow rheologies with MOLA. *Icarus* 165, 26–33.
- Gottsmann, J., Giordano, D., Dingwell, D., 2002. Predicting shear viscosity during volcanic processes at the glass transition a calorimetric calibration. *Earth and Planetary Science Letters* 198, 417–427.
- Greeley, R., 2005. Fluid lava flows in Gusev crater, Mars. *Journal of Geophysical Research* 110.
- Greeley, R., Crown, D.A., 1990. Volcanic geology of Tyrrhena Patera, Mars. *J. Geophys. Res.* 95, 7133–7149.
- Greeley, R., Spudis, P., 1981. Volcanism on Mars. reviews of geophysics and space physics 18, 13–41.
- Gregg, T.K.P., Fink, J.H., 1996. Quantification of extraterrestrial lava flow effusion rates through laboratory simulations. *J. Geophys. Res.* 101, 16891–16900.

- Gregg, T.K.P., Fink, J.H., 2000. A laboratory investigation into the effects of slope on lava flow morphology. *J. Volcanol.Geochem.Res.* 96, 145–159.
- Grott, M., Baratoux, D., Hauber, E., Sautter, V., Mustard, J., Gasnault, O., Ruff, S.W., Karato, S.I., Debaille, V., Knapmeyer, M., Sohl, F., Van Hoolst, T., Breuer, D., Morschhauser, A., Toplis, M.J., 2013. Long-term evolution of the martian crust-mantle system. *Space Science Reviews* 174, 49–111.
- Grott, M., Wicczorek, M., 2012. Density and lithospheric structure at Tyrrhena Patera, Mars, from gravity and topography data. *Icarus* 221, 43–52.
- Gwinner, K., Scholten, F., Preusker, F., Elgner, S., Roatsch, T., Spiegel, M., Schmidt, R., Oberst, J., Jaumann, R., Heipke, C., 2010. Topography of Mars from global mapping by HRSC high-resolution digital terrain models and orthoimages: characteristics and performance. *Earth Planet. Sci. Lett.* 294, 506–519.
- Handwerker, C.A., Onorato, P.I.K., Uhlmann, D., 1977. Matrix glass vs. intruded glass in lunar breccia 15286. *Proceedings of the Eighth Lunar Science Conference* 2, 2581–25972.
- Handwerker, C.A., Onorato, P.I.K., Uhlmann, D., 1978. Viscous flow, crystal growth, and glass formation of highland and mare basalts from Luna 24. *Mare Crisium: The view from Luna 24 in Pergamon Press (NY)* , 483–493.
- Harris, A.J.L., Allen, J.S., 2008. One-, two- and three-phase viscosity treatments for basaltic lava flows. *Journal of Geophysical Research* 113.
- Hartmann, W.K., Malin, M., McEwen, A., Carr, M., Soderblom, L., Thomas, P., Danielson, E., James, P., Veverka, J., 1999. Evidence for recent volcanism on Mars from crater counts. *Nature* 397, 586–589.
- Hauber, A., Bleacher, J., Gwinner, K., Williams, D., Greeley, R., 2009. Topography and morphology of low shields and associated landforms of plains volcanism in the Tharsis region of Mars. *Journal of Volcanology and Geothermal Research* 185, 69–95.
- Hauber, E., Broz, P., Jagert, F., Jodlowski, P., Platz, T., 2011. Very recent and wide spread basaltic volcanism on Mars. *Geophysical Research Letters* 38, L10201.
- Henderson, G.S., 2005. The structure of silicate melts: a glass perspective. *Canadian Mineralogist* 43, 1921–1958.
- Herd, C.D.K., 2008. Basalts as probes of planetary interior redox state. *Reviews in Mineralogy and Geochemistry* 68, 527–553.

- Herd, C.D.K., Borg, L., Jones, J.H., Papike, J.J., 2002. Oxygen fugacity and geochemical variations in the martian basalts: Implications for martian basalt petrogenesis and the oxidation state of the upper mantle of Mars. *Geochimica et Cosmochimica Acta*, 66, 2025–2036.
- Hess, K.U., Dingwell, D., 1996. Viscosities of hydrous leucogranitic melts: A non-Arrhenian model. *American Mineralogist* 81, 1297–1300.
- Hess, K.U., Dingwell, D.B., Rössler, E., 1995. Parametrization of viscosity-temperature relations of aluminosilicate melts. *Chemical Geology* 128, 155–163.
- Hess, K.U., Lavallée, Y., Castro, J., Noll, K., Mueller, S., Dingwell, D.B., Cameron, B., Spieler, O., Fink, J.H., 2005. Rheology of obsidian flow: Emplacement controlled by final water degassing? EOS Transaction, American Geophysical Union 85, Fall Meeting Suppl. Abstract V53C–1584.
- Hiesinger, H., Head, J.W., Neukum, G., 2007. Young lava flows on the eastern flank of Ascraeus Mons: Rheological properties derived from High Resolution Stereo Camera (HRSC) images and Mars Orbiter Laser Altimeter (MOLA) data. *Journal of Geophysical Research* 112.
- Hoover, S., Cashman, K.V., Manga, M., 2001. The yield strength of subliquidus basalts — experimental results. *Journal of Volcanology and Geothermal Research* 107, 1–18.
- Hovius, N., Leacox, A., Turowski, J., 2008. Recent volcano—ice interaction and outburst flooding in a Mars polar cap re-entrant. *Icarus* 197, 24–38.
- Hui, H., Zhang, Y., 2007. Toward a general viscosity equation for natural anhydrous and hydrous silicate melts. *Geochimica et Cosmochimica Acta* 71, 403–416.
- Hulme, G., 1974. The interpretation of lava flow morphology. *Geophys. J. R. Astron. Soc.* 39, 361–383.
- Huppert, E., Sparks, R.S.J., 1985. Komatiites I : Eruption and Flow. *Journal of Petrology* 26, 694–725.
- Hurowitz, J.A., McLennan, S.C., Lindsley, D.H., Schoonen, M.A., 2005. Experimental epithermal alteration of synthetic Los Angeles meteorite: Implication for the origin of Martian soils and identification of hydrothermal sites on Mars. *Journal of Geophysical Research* 110, E07002.

- Hynek, B.M., Phillips, R.J., Arvidson, R.E., 2003. Explosive volcanism in the Tharsis region: Global evidence in the Martian geologic record. *Journal of Geophysical research* 108, 51111.
- Ishibashi, H., 2009. Non-Newtonian behavior of plagioclase-bearing basaltic magma: subliquidus viscosity measurement of the 1707 basalt of Fuji volcano, Japan. *J. Volcanol. Geoth. Res.* 181, 78–88.
- Ishibashi, H., Sato, H., 2007. Viscosity measurements of subliquidus magmas: Alkali olivine basalt from the Higashi-Matsuura district, Southwest Japan. *Journal of Volcanology and Geothermal Research* 160, 223–238.
- Jaeger, W.L., Keszthelyi, L.P., McEwen, A.S., Dundas, C.W., Russell, P.S., 2007. Athabasca valles, Mars: A lava-draped channel system. *Science* 317, 1709–1711.
- Jaeger, W.L., Keszthelyi, L.P., Skinner Jr, J.A., Milazzo, M.P., McEwen, A.S., Titus, T.N., Rosiek, M.R., Galuszka, D.M., Howington-Kraus, E., Kirk, R.L., 2010. Emplacement of the youngest flood lava on Mars: A short, turbulent story. *Icarus* 205, 230–243.
- Jeffreys, H., 1925. The flow of water in an inclined channel of rectangular section. *Phil. Mag. serie 6*, 49, 293, 793–807.
- Karamanov, A., Di Gioacchino, R., Piscicella, P., Pelino, M., Hreglich, A., 2002. Crystallization phenomena in iron-rich glasses. *Glass Technol* 43, 34–38.
- Karamanov, A., Pelino, M., 2001. Crystallization phenomena in iron-rich glasses. *Journal of Non-Crystalline Solids* 281, 139–151.
- Kinzler, R.J., Grove, T., 1985. Crystallization and differentiation of Archean komatiite lavas from northeast Ontario: phase equilibrium and kinetic studies. *American Mineralogist* 70, 40–51.
- Klein, I., Onorato, D., Uhlmann, H., 1975. Viscous flow, crystallization behavior and thermal history of lunar breccias 70059 and 79155. In *Proceedings of the Sixth Lunar Science Conference*. 1, 579–593.
- Knudson, J.G., Katz, D.L., 1958. *Fluid dynamics, heat transfer*. McGraw-Hill, 81–82.
- Kondratiev, A., Hayes, P.C., Jak, E., 2008. Development of a quasi-chemical viscosity model for fully liquid slags $\text{Al}_2\text{O}_3\text{-CaO-}'\text{FeO}'\text{-MgO-SiO}_2$ system. the experimental data for the $\text{'FeO}'\text{-MgO-SiO}_2\text{CaO-FeO-MgO-SiO}_2$ and $\text{Al}_2\text{O}_3\text{-CaO-FeO-MgO-SiO}_2$ systems at iron saturation. *Isij International* 48, 7–16.

- Kremers, S., Lavallée, Y., Hanson, J., Hess, K.U., Chevrel, M.O., Wassermann, J., Dingwell, D.B., 2012. Shallow magma-mingling-driven Strombolian eruptions at Mt. Yasur volcano, Vanuatu. *Geophysical Research Letters* 39, L21304.
- Kress, V., Carmichael, I.S.E., 1991. The compressibility of silicate liquids containing Fe_2O_3 and the effect of composition, temperature, oxygen fugacity and pressure on their redox states. *Contrib. Mineral Petrol.* 108, 82–92.
- Krieger, I.M., Dougherty, T., 1959. A mechanism for non-Newtonian flow in suspensions of rigid spheres. *Journal of Rheology* 3, 137.
- Kuno, H., 1965. Fractionation trends of basaltic magmas in lava flows. *Journal of Petrology* 6, 302–321.
- Kushiro, I., Yoder Jr., H., Mysen, B., 1976. Viscosities of basalt and andesite melts at high pressures. *J. Geophys. Res.* 81, 6351–6356.
- Lang, N.P., McSween, H.Y., Tornabene, L.L., Hardgrove, C.J., Christensen, P.R., 2010. Reexamining the relationship between Apollinaris Patera and the basalts of the Gusev crater plains, Mars. *Journal of Geophysical Research* 115.
- Lange, R.A., Carmichael, I.S.E., 1987. Densities of Na_2O - K_2O - CaO - MgO - FeO - Fe_2O_3 - Al_2O_3 - TiO_2 - SiO_2 liquids: New measurements and derived partial molar properties. *Geochimica et Cosmochimica Acta* 51, 2931–2946.
- Lattard, D., Partzsch, G.M., 2001. Magmatic crystallization experiments at 1 bar in systems closed to oxygen: a new/old experimental approach. *Eur. J. Mineral* 13, 467–478.
- Lavallée, Y., Hess, K.U., Cordonnier, B., Dingwell, D.B., 2007. Non-Newtonian rheological law for highly crystalline dome lavas. *Geology* 35, 843–846.
- Lavallée, Y., Varley, N.R., Alatorre-Ibargüengoitia, M.A., Hess, K.U., Kueppers, U., Mueller, S., Richard, D., Scheu, B., Spieler, O., Dingwell, D.B., 2012. Magmatic architecture of dome-building eruptions at Volcán de Colima, Mexico. *Bull. Volcanol.* 74, 249–260.
- Lejeune, A.M., Bottinga, Y., Trull, T.W., P., R., 1999. Rheology of bubble-bearing magmas. *Earth Planet. Sci. Lett.* 166, 71–84.
- Lejeune, A.M., Richet, P., 1995. Rheology of crystal-bearing silicate melts: an experimental study at high viscosities. *J. Geophys. Res.* 100, 4215–4230.

- Leverington, D.W., 2011. A volcanic origin for the outflow channels of Mars: Key evidence and major implications. *Geomorphology* 132, 51–75.
- Lewis, J.S., 1972. Metal/Silicate fractionation in the Solar system. *Science Letters* 15, 286–290.
- Liebske, C., Behrens, H., Holtz, F., Lange, R., 2003. The influence of pressure and composition on the viscosity of andesitic melts. *Geochimica et Cosmochimica Acta* 67, 473–485.
- Lipman, P.W., Banks, N.G., Rhodes, J.M., 1985. Degassing-induced crystallization of basaltic magma and effects on lava rheology. *Nature* 317, 604–607.
- Lodders, K., Fegley, B., 1997. An oxygen isotope model for the composition of Mars. *Icarus* 126, 373–394.
- Lyman, A., Koenig, E., Fink, J.H., 2004. Predicting yield strengths and effusion rates of lava domes from morphology and underlying topography. *Journal of Volcanology and Geothermal Research* 129, 125–138.
- Magnien, V., Neuville, D.R., Cormier, L., Mysen, B., Briois, V., Belin, S., Pinet, O., Richet, P., 2004. Kinetics of iron oxidation in silicate melts: a preliminary XANES study. *Chemical Geology* 213, 253–263.
- Manga, M., Castro, J., Cashman, K.V., M., L., 1998. Rheology of bubble-bearing magmas. *Journal of Volcanology and Geothermal Research* 87, 15–28.
- Manson, V., 1967. Geochemistry of basaltic rocks: Major elements. in basalts. Hess and Poldervaart. eds. Intersciences publishers, New York 1, 215–269.
- Marsh, B., 1981. On the crystallinity, probability of occurrence, and rheology of lava and magma. *Contrib. Mineral. Petrol.* 78, 85–98.
- McSween, H., Taylor, G.J., Wyatt, M.B., 2009. Elemental composition of the martian crust. *Science* 324.
- McSween, H.Y., 2004. Basaltic rocks analyzed by the Spirit Rover in Gusev crater. *Science* 305, 842–845.
- McSween, H.Y., Ruff, S.W., Morris, R.V., Bell, J.F., Herkenhoff, K., Gellert, R., Stockstill, K.R., Tornabene, L.L., Squyres, S.W., Crisp, J.A., Christensen, P.R., McCoy, T.J., Mittlefehldt, D.W., Schmidt, M., 2006a. Alkaline volcanic rocks from the Columbia Hills, Gusev crater, Mars. *Journal of Geophysical Research* 111.

- McSween, H.Y., Wyatt, M.B., Gellert, R., Bell, J.F., Morris, R.V., Herkenhoff, K.E., Crumpler, L.S., Milam, K.A., Stockstill, K.R., Tornabene, L.L., Arvidson, R.E., Bartlett, P., Blaney, D., Cabrol, N.A., Christensen, P.R., Clark, B.C., Crisp, J.A., Des Marais, D.J., Economou, T., Farmer, J.D., Farrand, W., Ghosh, A., Golombek, M., Gorevan, S., Greeley, R., Hamilton, V.E., Johnson, J.R., Joliff, B.L., Klingelhöfer, G., Knudson, A.T., McLennan, S., Ming, D., Moersch, J.E., Rieder, R., Ruff, S.W., Schröder, C., de Souza, P.A., Squyres, S.W., Wänke, H., Wang, A., Yen, A., Zipfel, J., 2006b. Characterization and petrologic interpretation of olivine-rich basalts at Gusev crater, Mars. *Journal of Geophysical Research* 111, E02S10.
- Michaut, C., 2011. Dynamics of magmatic intrusions in the upper crust: Theory and applications to laccoliths on Earth and the Moon. *Journal of Geophysical Research (Planets)*, 305, 116, B05.
- Michaut, C., Baratoux, D., 2013, submitted. Evidence for magmatic intrusions and significant deglaciation at mid-latitude in the northern plains of Mars. *Journal of Geophysical Research (Planets)* .
- Ming, D.W., Gellert, R., Morris, R.V., Arvidson, R.E., Brückner, J., Clark, B.C., Cohen, B.A., d'Uston, C., Economou, T., Fleischer, I., Klingelhöfer, G., McCoy, T.J., Mittlefehldt, D.W., Schmidt, M.E., Schröder, C., Squyres, S.W., Tréguier, E., Yen, A.S., Zipfel, J., 2008. Geochemical properties of rocks and soils in Gusev Crater, Mars: Results of the Alpha Particle X-Ray Spectrometer from Cumberland Ridge to Home Plate. *Journal of Geophysical Research* 113.
- Monders, A.G., Médard, E., Groove, T.L., 2007. Phase equilibrium investigations of the Adirondack class basalts from the Gusev plains , Gusev crater, Mars. *Meteoritics and Planetary Science* 42, 131–148.
- Moore, H.J., G., A.D.W., G., S.G., 1978. Yield strengths of flows on the earth, Mars, and Moon. *Proc. Lunar Planet. Sci. Conf. 9th* , 3351–3378.
- Moore, H.J., Schaber, G.G., 1975. An estimate of the yield strength of the Imbrium flows. *Proc. Lunar Sci. Conf. 6th* , 101–118.
- Moretti, R., 2005. Polymerisation, basicity, oxidation state and their role in ionic modelling of silicate melts. *Annals of Geophysics* 48.
- Moretti, R., Papale, P., 2004. On the oxidation state and volatile behaviour in multicomponent gas-melt equilibria. *Chemical Geology* 213.

- Moynihan, C., 1995. Structural relaxation and the glass transition. In Stebbins, J.F. , McMillan, P.F., and Dingwell, D.B., Eds., Structure, dynamics and properties of silicate melts, Reviews in Mineralogy, Mineralogical Society of America, Chantilly, Virginia , 1–19.
- Moynihan, C.T., Easteal, A.J., Wilder, J., Tucker, J., 1974. Dependence of glass transition temperature on heating and cooling rate. *Journal of Physical Chemistry* 78, 2673–2677.
- Mueller, S., Llewellyn, E.W., Mader, H.M., 2010. The rheology of suspensions of solid particles. *Philos. Trans. R. Soc. Lond. A* 466, 1201–1228.
- Murase, T., McBirney, A., 1970. Viscosity of lunar lavas. *Science* 167, 1491–1493.
- Murase, T., McBirney, A., 1973. Properties of some common igneous rocks and their melts at high temperatures. *Geological Society of America Bulletin* 84, 3563–3592.
- Mustard, J.F., Poulet, F., Gendrin, A., Bibring, J.P., Langevin, Y., Gondet, B., Mangold, N., Belluci, G., Altieri, F., 2005. Olivine and pyroxene diversity in the crust of mars. *Science* 307, 1595–1597.
- Mysen, B.O., 1988. Structure and properties of silicate melts. *Developments in Geochemistry* No. 4. Elsevier. .
- Mysen, B.O., 1991. Relation between structure, redox equilibria of iron, and properties of magmatic liquids. *Adv. Phys. Chem.* 9, 41–98.
- Mysen, B.O., Richet, P., 2005. Silicate glasses and melts: Properties and structure. Elsevier Science .
- Mysen, B.O., Virgo, D., 1989. Redox equilibria, structure, and properties of fe-bearing aluminosilicate melts: Relationship among temperature, composition, and oxygen fugacity in the system $\text{Na}_2\text{O}-\text{Al}_2\text{O}_3-\text{Si}_2\text{O}-\text{Fe}-\text{O}$. *American Mineralogist* 74, 58–76.
- Mysen, B.O., Virgo, D., Seifert, F., 1984. Redox equilibria of iron in alkaline earth silicate melts: relationships between melt structure, oxygen fugacity, temperature and properties of iron-bearing silicate liquids. *American Mineralogist* 69, 834–847.
- Myuller, R., 1955. A valence theory of viscosity and fluidity for high-melting glass forming materials in the critical temperature range. *Zh. Prikl. Khim.* 28, 1077–1087.
- Neukum, G., Jaumann, R., Hoffmann, H., Hauber, E., Head, J.W., Basilevsky, A.T., Ivanov, B.A., Werner, S.C., van Gasselt, S., Murray, J.B., McCord, T., TeamThe, H.C.I., 2004. Recent and episodic volcanic and glacial activity on Mars revealed by the High Resolution Stereo Camera. *Nature* 432, 971–979.

- Neuville, D.R., Richet, P., 1991. Viscosity and mixing in molten (Ca, Mg) pyroxenes and garnets. *Geochemica et Cosmochimica Acta.* 55, 1011–1019.
- Nichols, R., 1939. Viscosity of lava. *The Journal of Geology* 47, 290–302.
- Norman, M., Garcia, M., 1999. Primitive magmas and source characteristics of the Hawaiian plume: petrology and geochemistry of shield picrites. *Earth and Planetary Science Letters* 168, 27–44.
- Page, D., 2008. Comments on Athabasca Valles, Mars: A lava-draped channel system. *Science* 320, 1588b.
- Page, D., 2010. Resolving the Elysium controversy: An open invitation to explain the evidence. *Planetary and Space science* 58, 1406–1413.
- Papale, P., 1999. Strain-induced magma fragmentation in explosive eruptions. *Nature* 397, 425–428.
- Pasckert, J.H., Hiesinger, H., Reiss, D., 2012. Rheologies and ages of lava flows on Elysium Mons, Mars. *Icarus* 219, 443–457.
- Perchuk, L., Kushiro, I., 1991. *Physical chemistry of magmas.* Springer .
- Petford, N., 2009. Which effective viscosity? *Mineralogical Magazine* 73, 167–191.
- Philpotts, A.R., 1979. Silicate liquid immiscibility in tholeiitic basalts. *Journal of Petrology* 20, 99–118.
- Philpotts, A.R., 2008. Comments on: Liquid immiscibility and the evolution of basaltic magma. *Silicate Liquid Immiscibility in Tholeiitic Basalts* 49, 2171–2175.
- Pinkerton, H., 1987. Factor affecting the morphology of lava flows. *Endeavour* 11, 73–79.
- Pinkerton, H., Norton, G., 1995. Rheological properties of basaltic lavas at sub-liquidus temperatures: laboratory and field measurements on lavas from Mount Etna. *J. Volcanol. Geotherm. Res.* 68, 307–323.
- Pinkerton, H., Sparks, R., 1976. The 1975 sub-terminal lavas, mount etna: a case history of the formation of a compound lava field. *Journal of Volcanology and Geothermal Research* 1, 167–182.
- Pinkerton, H., Sparks, R.S.J., 1978. Field measurements of the rheology of lava. *Nature* 276, 383–385.

- Pinkerton, H., Stevenson, R.J., 1992. Methods of determining the rheological properties of magmas at sub-liquidus temperatures. *J. Volcanol. Geotherm. Res.* 53, 47–66.
- Pinkerton, H., Wilson, L., 1994. Factor controlling the lengths of channel-fed lava flows. *Bull. Volcanol.* 6, 108–120.
- Pistone, M., Caricchi, L., Ulmer, P., Burlini, L., Ardia, P., Reusser, E., Marone, F., L., A., 2012. Deformation experiments of bubble- and crystal-bearing magmas: Rheological and microstructural analysis. *J. Geophys. Res.* 117, B05208.
- Platz, T., Michael, G., 2011. Eruption history of the Elysium Volcanic Province, Mars. *Earth and Planetary Science Letters* 312, 140–151.
- Platz, T., Münn, S., Walter, T., McGuire, P., Dumke, A., Neukum, G., 2011. Vertical and lateral collapse of Tharsis Tholus, Mars. *Earth and Planetary Science Letters* 305, 445–455.
- Plazek, D., Ngai, K., 1991. Correlation of polymer segmental chain dynamics with temperature-dependent time-scale shifts. *Macromolecules* 24, 1222–1224.
- Pouchou, J.L., Pichoir, F., 1985. ‘PAP’ procedure for improved quantitative microanalysis. *Microbeam analysis*. San Francisco Press, San Francisco , 104–160.
- Poulet, F., Mangold, N., Platevoet, B., Bardintzeff, J.M., Sautter, V., Mustard, J., Bibring, J., Pinet, P., Langevin, Y., Gondet, B., Aléon-Toppani, A., 2009. Quantitative compositional analysis of martian mafic regions using the MEx/OMEGA reflectance data 2. Petrological implications. *Icarus* 201, 84–101.
- Putirka, K., 2008. Thermometers and barometers for volcanic systems. Putirka, K., Tepley, F. (Eds.), *Minerals, Inclusions and Volcanic Processes*, *Reviews in Mineralogy and Geochemistry*, Mineralogical Soc. Am. 69, 61–120.
- Richet, P., 1987a. Heat capacity of silicate glasses. *Chemical Geology* 62, 111–124.
- Richet, P., 1987b. Viscosity and configurational entropy of silicate melts. *Geochemica at Cosmochimica Acta* 48, 471– 483.
- Richet, P., 2009. Residual and configurational entropy: Quantitative checks through application of Adam-Gibbs theory to the viscosity of silicate melts. *Journal of Non-Crystalline Solids* 355, 628–635.
- Richet, P., Bottinga, Y., 1995. Rheology and configurational entropy of silicate melts. In Stebbins, J.F. , McMillan, P.F., and Dingwell, D.B., Eds., *Structure, dynamics and*

- properties of silicate melts, *Reviews in Mineralogy*, Mineralogical Society of America, Chantilly, Virginia. *Reviews in Mineralogy*, Mineralogical Society of America, Chantilly, Virginia. 32, 67–93.
- Richet, P., R., N.D., 1992. Thermodynamics of silicate melts: configurational properties. *Adv. Phys. Geochem.* 10, 132–160.
- Rieder, R., Gellert, R., Anderson, R.C., Brückner, J., Clark, B.C., Dreibus, G., Economou, T., Klingelhöfer, G., Lugmair, G.W., Ming, D.W., Squyres, S.W., d’Uston, C., Wänke, H., Yen, A., Zipfel, J., 2004. Chemistry of rocks and soils at Meridiani Planum from the Alpha Particles X-Ray Spectrometer. *Science* 306, 1746–1749.
- Roedder, E., 1978. Silicate liquid immiscibility in magmas and in the system K_2O - FeO - Al_2O_3 - SiO_2 : an example of serendipity. *Geochemica et Cosmochimica Acta* 42, 1597–1617.
- Romano, C., Giordano, D., Papale, P., Mincione, V., D.B., D., Rosi, M., 2003. The dry and hydrous viscosities of alkaline melts from vesuvius and phlegrean fields. *Chemical and Geology* 202, 23–38.
- Russell, J., Giordano, D., 2005. A model for silicate melt viscosity in the system $CaMgSi_2O_6$ - $CaAl_2Si_2O_8$ - $NaAlSi_3O_8$. *Geochim. Cosmochim. Acta* 69, 5333–5349.
- Russell, J., Giordano, D., Dingwell, D., 2003. High-temperature limits on viscosity of non-Arrhenian silicate melts. *Am. Min.* 88.
- Russell, J., Giordano, D., Dingwell, D., Hess, K.U., 2002. Modelling the non-Arrhenian rheology of silicate melts: Numerical considerations. *European Journal of Mineralogy* 14, 417–427.
- Ryerson, F.J., Weed, H.C., Piwinski, A.J., 1988. Rheology of subliquidus magmas: I Picritic compositions. *J. Geophys. Res.* 93, 3421–3436.
- Saar, M.O., Manga, M., 1999. Permeability-porosity relationship in vesicular basalts. *Geophys. Res. Lett.* 26, 111–114.
- Saar, M.O., Manga, M., Cashman, K.V., Fremouw, S., 2001. Numerical models of the onset of yield strength in crystal-melt suspensions. *Earth and Planetary Science Letters* 187, 367–379.
- Sanloup, C., Jambon, A., Gillet, P., 1999. A simple chondritic model of Mars. *Physics of the Earth and Planetary Interiors* 112, 43–54.

- Sato, H., 2005. Viscosity measurement of subliquidus magmas: 1707 basalt of Fuji volcano. *Journal of Mineralogical and Petrological Sciences* 100, 133–142.
- Scarfe, C.M., Cronin, D.J., Wenzel, J.T., Kauffman, D.A., 1983. Viscosity-temperature relationship at 1 atm in the system Diopside-Anorthite. *American Mineralogist* 68, 1083–1088.
- Scherer, G., 1984. Use of the Adam-Gibbs equation in the analysis of structural relaxation. *Journal of American Ceramic Society* 67, 504–511.
- Scholten, F., Gwinner, K., Roatsch, T., Matz, K.D., Wählich, M., Giese, B., Oberst, J., Jaumann, R., Neukum, G., 2005. Mars Express HRSC data processing — methods and operational aspects. *Photogram. Eng. Remote Sensing*. 71, 1143–1152.
- Shaw, H.R., 1969. Rheology of basalt in the melting range. *J. Petrol.* 10, 510–535.
- Shaw, H.R., 1972. Viscosities of magmatic silicate liquids: An empirical method of prediction. *Am. J. Sci.* 272, 870–893.
- Sinton, J., Grönvold, K., Sæmundsson, K., 2005. Postglacial eruptive history of the Western Volcanic Zone, Iceland. *Geochemistry Geophysics Geosystems* 6.
- Sipp, A., Neuville, D.R., Richet, P., 1997. Viscosity, configurational entropy and relaxation kinetics of borosilicate melts. *Journal of Non-Crystalline Solids* 211, 281–293.
- Sipp, A., Richet, P., 2002. Equivalence of volume, enthalpy and viscosity relaxation kinetics in glass-forming silicate liquids. *Journal of Non-Crystalline Solids* 298, 202–212.
- Solvang, M., Yue, Y., Jensen, S.L., 2004. The effects of Mg–Ca and Fe–Mg substitution on rheological and thermodynamic properties of aluminosilicate melts. *Journal of Non-Crystalline Solids* 345-346, 782–786.
- Sparks, R., 2003. Dynamics of magma degassing. *Volcanic Degassing*, Eds, Oppenheimer, C. and Pyle, D. M. and Barclay, J., Geological Soc Publishing House 213, 5–22.
- Stebbins, J., McMillan, P., Dingwell, D., 1995. Structure, dynamics and properties of silicate melts. *Reviews in Mineralogy*, Mineralogical Society of America .
- Stebbins, J.F., 2008. Temperature effects on the network structure of oxide melts and their consequences for configurational heat capacity. *Chem. Geol.* 256, 80–91.
- Stein, D.J., Spera, F.J., 1992. Rheology and microstructure of magmatic emulsions: Theory and experiments. *J. Volcanol. Geotherm. Res.* 49, 157–174.

- Stein, D.J., Spera, F.J., 2002. Shear viscosity of rhyolite-vapor emulsions at magmatic temperatures by concentric cylinder rheometry. *J. Volcanol. Geotherm. Res.* 113, 243–258.
- Stockstill-Cahill, K.R., Anderson, F.S., Hamilton, V.E., 2008. A study of low-albedo deposits within Amazonis Planitia craters: Evidence for locally derived ultramafic to mafic materials. *J. Geophys. Res.* 113.
- Stout, M.Z., Nicholls, J., Kuntz, M.A., 1994. Petrological and mineralogical variations in 2500-2000 yr B.P. Lava Flows, Crater of the Moon, Idaho. *Journal of Petrology* 35, 1681–1715.
- Tammann, G., Hesse, W., 1926. Die Abhängigkeit der Viskosität von der Temperatur bei unterkühlten Flüssigkeiten. *Z. Anorg. Allg. Chem.* 156, 245–257.
- Toplis, M., 1998. Energy barriers to viscous flow and the prediction of glass transition temperatures of molten silicates. *Am. Mineral.* 83, 480–490.
- Toplis, M., Dingwell, D., Hess, K.U., Lenci, T., 1997. Viscosity, fragility, and configurational entropy of melts along the join $\text{SiO}_2\text{-NaAlSiO}_4$. *Am. Mineral.* 82, 979–990.
- Toplis, M., Dingwell, D., Libourel, G., 1994. The effect of phosphorus on the iron redox ratio, viscosity, and density of an evolved ferro-basalt. *Contrib. Mineral Petrol.* 117, 293–304.
- Toplis, M., Gottsmann, J., Knoche, R., Dingwell, D.B., 2001. Heat capacities of haplogranitic glasses and liquids. *Geochemica et Cosmochimica Acta* 65, 1985–1994.
- Toplis, M.J., Carroll, M.R., 1995. An experimental study of the influence of oxygen fugacity on Fe-Ti oxide stability, phase relations, and mineral-melt equilibria in ferro-basaltic systems. *Journal of Petrology* 36, 1137–1170.
- Tosca, N.J., McLennan, S.M., Lindsley, D.H., Schoonen, M.A.A., 2004. Acid-sulfate weathering of synthetic Martian basalt: The acid fog model revisited. *Journal of Geophysical Research* 109, E05003.
- Uhlmann, D.R., Klein, L., 1976. Crystallization kinetics, viscous flow, and thermal histories of lunar breccias 15286 and 15498. *Proc. Lunar Sci. Conf*, 7th, 2529–2541.
- Uhlmann, D.R., Klein, L., 1977. Crystallisation kinetics, viscous flows and thermal histories of lunar breccias 67975. *Geochim. Cosmochim. Acta* 2, 2067–2078.

- Uhlmann, D.R., Klein, L., Kritchevsky, G., Hopper, R.W., 1974. The formation of lunar glasses. *Geochim. Cosmochim. Acta Suppl.* 3, 2317–2331.
- Vaucher, J., Baratoux, D., Mangold, N., Pinet, P., Kurita, K., Grégoire, M., 2009a. The volcanic history of central Elysium Planitia: Implications for Martian magmatism. *Icarus* 204, 418–442.
- Vaucher, J., Baratoux, D., Toplis, M.J., Pinet, P., Mangold, N., Kurita, K., 2009b. The morphologies of volcanic landforms at Central Elysium Planitia: Evidence for recent and fluid lavas on Mars. *Icarus* 200, 39–51.
- Veksler, I.V., 2009. Extreme iron enrichment and liquid immiscibility in mafic intrusions: Experimental evidence revisited. *Lithos* 111, 72–82.
- Veksler, I.V., Dorfman, A.M., Borisov, A.A., Wirth, R., Dingwell, D.B., 2007. Liquid immiscibility and the evolution of basaltic magma. *Journal of Petrology* 48, 2187–2210.
- Veksler, I.V., Dorfman, A.M., Borisov, A.A., Wirth, R., Dingwell, D.B., 2008. Liquid immiscibility and evolution of basaltic magma: Reply to S. A. Morse, A. R. McBirney and A. R. Philpotts. *Journal of Petrology* 49, 2177–2186.
- Villeneuve, N., Neuville, D., Boivin, P., Bachèlery, P., Richet, P., 2008. Magma crystallization and viscosity: A study of molten basalts from the Piton de la Fournaise volcano (La Réunion island). *Chemical Geology* 256, 242–251.
- Vogel, D., 1921. Temperaturabhängigkeitsgesetz der Viskosität von Flüssigkeiten. *Phys. Z.* 22, 645–646.
- Vona, A., Romano, C., Dingwell, D.B., Giordano, D., 2011. The rheology of crystal-bearing basaltic magmas from Stromboli and Etna. *Geochimica et Cosmochimica Acta*, 3214–3236.
- Walker, G.P.L., 1973. Lengths of lava flows. *Philosophical Transactions of the Royal Society, London* 274, 107–118.
- Wänke, H., 1981. Constitution of terrestrial planets. *Philosophical Transactions of the Royal Society of London.* 303, 287–302.
- Warner, N.H., Gregg, T.K.P., 2003. Evolved lavas on Mars? Observations from southwest Arsia Mons and Sabancaya volcano, Peru. *Journal of Geophysical Research* 108.
- Webb, S., 2005. Structure and rheology of iron-bearing $\text{Na}_2\text{O-Al}_2\text{O}_3\text{SiO}_2$. *European Journal of Mineralogy* 17, 223–232.

- Werner, S., 2005. Major aspects of the chronostratigraphy and geologic evolutionary history of Mars. PhD thesis, Freie Universität, Berlin .
- Werner, S., 2009. The global martian volcanic evolutionary history. *Icarus* 201, 44–68.
- Whittington, A., Richet, P., Linard, Y., Francois, H., 2001. The viscosity of hydrous phonolites and trachytes. *Chemical Geology* 174, 209–223.
- Wilke, M., 2005. Fe in magma – An overview. *Annals of Geophysics* 48.
- Wilke, M., Farges, F., Partzsch, G.M., Schmidt, C., Behrens, H., 2007. Speciation of Fe in silicate glasses and melts by in-situ XANES spectroscopy. *American Mineralogist* 92, 44–56.
- Williams, D.A., Greeley, R., Ferguson, R.L., Kuzmin, R., McCord, T.B., Combe, J.P., Head III, J.W., Xiao, L., Manfredi, L., Poulet, F., 2009. The Circum-Hellas Volcanic Province, Mars: Overview. *Planetary and Space Science* 57, 895–916.
- Wilson, L., 2001. Evidence for episodicity in the magma supply to the large Tharsis volcanoes. *J. Geophys. Res.* 106, 1423–1434.
- Wilson, L., Head, J.W., 1983. A comparison of volcanic eruption processes on Earth, Moon, Mars, Io, and Venus. *Nature* 302, 663–669.
- Wilson, L., Head, J.W., 1994. Mars review and analysis of volcanic eruption theory and relationships to observed landforms. *Reviews of geophysics* 32, 221–263.
- Wilson, L., Mouginis-Mark, P., Tyson, S., Mackown, J., Garbeil, H., 2009. Fissure eruptions in Tharsis , Mars implications for eruption conditions and magma sources. *Journal of Volcanology and Geothermal Research* 185, 28–46.
- Wilson, S., Koenig, A., Lowers, H., 2012. A new basaltic glass microanalytical reference material for multiple techniques. *Microscopy Today* 20, 12–16.
- Yoder, C.F., 2003. Fluid core size of Mars from detection of the solar tide. *Science* 300, 299–303.
- Zhou, J.Z.Q., Fang, T., Luo, G., Uhlerr, P.H.T., 1995. Yield stress and maximum packing fraction of concentrated suspensions. *Rheol. Acta* . 34, 544–561.
- Zimbelman, J.R., 1985. Estimates of rheologic properties for flows on the Martian Volcano Ascraeus Mons. *Journal of Geophysical Research* 90, D157, D162.

Zimbelman, J.R., 1998. Emplacement of long lava flows on planetary surfaces. *Journal of Geophysical research* 103, 27,503–27,516.

Zipfel, J., Anderson, R., Brückner, J., Clark, B.C., Dreibus, G., Economou, T., Gellert, R., Klingelhöfer, G., Lugmair, G., Ming, D., Reider, R., Squyres, S.W., d'Uston, C., Wänke, H., Yen, A., 2004. APXS analyses of bounce rock- the first shergottites on Mars. *Meteoritics and Planetary Science* 39 (Suppl): A118, –.

Acknowledgments

Time to thank everybody from the funding to whoever was around to support me at one point, supervisors, co-authors, administrative and technical support, colleagues, friends, and everybody that I forget to mention.

The first acknowledgments go to the THESIS program from the Elitenetzwerk von Bayern for the financial support, to my supervisors, Prof. Don. Dingwell and Dr. David Baratoux, and to my colleagues.

Don, I would like to thank you for the opportunity you gave to me to study, to work, to read, to analyze, to search, to travel, to present, to drill, to cut, to crush, to mix, to concentric cylinder, to quench, to fix, to heat, to screw, to wonder around, to look for, to hesitate, to try, to find, to retrieve, to enjoy and finally to melt rocks and investigate their flowing behavior! I'd like to thank you for the trust you put in me to manage this PhD and to handle your lab, for the freedom I had during those three years to experience what I found interesting. I'd like to thank you for your generosity in giving many opportunities to all your students by letting them do crazy experiments, go to field-trips and international meetings; that is, I guess, unique in the world.

David, mon martien, je tiens d'abord à remercier tes cours de L3, qui m'ont fascinée et ont renforcé ma motivation à étudier les planètes et leurs volcans. Je te remercie surtout pour ton soutien durant toutes ces années ; tu as toujours été là pour me soutenir, que ce soit pour aller au Canada, au Japon, en Allemagne et peut-être Mars un jour. Tu es celui grâce à qui j'ai fait cette thèse, tu es celui qui a eu l'idée et celui qui m'a offert l'opportunité de s'approprier ce sujet et de le traiter à ma guise. Je te remercie aussi pour cette volonté et cet enthousiasme dont tu fais preuve sans faillir, pour ta constante motivation pour apprendre et développer de nouvelles idées ! C'est un vrai plaisir de

travailler avec toi ! Que cela dure.

Kai and your critical view of science (mainly from french and italian scientific work), I thank you for your very helpful comments and suggestions all along my PhD and for the constant questioning of the existence of the universe around one, two, three glasses of beer or wine (french of course).

Werner, I'd like to acknowledge your kind help in showing me how to handle the lab, fix the furnaces, holding my hand when I was melting my first rock or when I thought I had put HF on my arm.

Special thanks to Betty and Ulli; you two were always there to take care of me and of us, you really helped to make us feel at home in this scientific group and in Bavaria; Yan and Corrado, with whom I discovered lava flow fields and active volcano, thank you guys for sharing exciting science and working with me; I hope that we will continue to do so.

Many thanks to the administrative support, to always keep the door open to have some coffee: Sandra, Margot, Yvonne, Helen, Rosa and Carina. To all the technical support staff, thank you for the help I received during my work here: Andre for the computers; Frau Wimmer and Thomas Dorfner for the chemical lab, Max and Markus for the electronic or mechanic hand and Hilger Lohringer for microprobe samples preparation. I would also like to thank Saskia, Dirk and Michael for their precious help with the microprobe. Special thank you to Sascha for developing the new viscometer software and to Lorenzo and Asher for the Matlab support.

Thanks as well to my co-authors who participated in the writing of my papers: Daniele Giordano, Marcel Potuzak (thank you for letting me use and interpret your experimental data), Philippe Courtial, the Berliners Thomas Platz and Ernst Hauber, with whom we camped for two weeks in the middle of Iceland.

I'd like to thank all my colleagues and friends that somehow have played their role in helping me going through this PhD: Basti, Benoit, Christoph, Diego, Mike, Cristina, Alex, Miguel, Rosie, Paul, Dominique, Jackie, Fabian, Jeremie, Laura, Cristian, Klaus. Special cheers to Jon (that I missed for half my PhD.) and my dear Lea for the awesome work we did together!

Guilhem, Amin, mon ami et compagnon de thèse, de soirée, d'escalade et de cosmic road trips! With a lot of love and positive vibrations, merci d'avoir été là, non-stop, pour tous ces moments partagés ensemble.

Daniele el sexiést italiano del mondo. Thank you my friend for crossing the "so big" America West desert. Thanks for your positive thoughts, for always giving me confidence and for all of those times when you cheered me up.

¡Gracias también a la Mamasita! For your support and friendship, your critical approach of the word, por el té, el café, el yoga, "a Mexico", y todo.

Un grand merci à Celinette, la magic geek, pour ton coup de main avec L^AT_EX, mais aussi pour ton amitié, ton écoute et les bons verres de vin rouge!

Thanks to my flat-mates, Andrea, Andi and Maria, and to my Münchner Freunde (Bayerische und Français) for supporting me at home, and for being there during the hard and the good times.

Je dois aussi écrire une ligne pour remercier Skype d'exister, car sans lui, je n'aurais pas pu profiter du soutiens de ceux qui habitent loin: mes amis de toujours (la Meuh, le Goof, le Mimi et le Bob), et la famille (spécial dédicace à Charlotton).

Merci et serrer fort à mes frérots et sister, pour aimer et croire en leur petite sœur! Et finalement, un grand remerciement à mon Papounet. Et oui Papa, voilà le résultat lorsque l'on pousse sa fille à faire des études ; je suis allée jusqu'au bout! Merci de toujours être de mon côté, de toujours me soutenir dans mes choix et de toujours me dire que ça va aller. Continue !

Curriculum Vitae

MSc. Magdalena Oryaëlle Chevrel

Experimental and Physical Volcanology
Department of Earth and Environmental Sciences
University of Munich (LMU)

Theresienstr. 41

80333 München

Germany

Phone: +49 (0)89 2180 4272

E-Mail: chevrel@min.uni-muenchen.de

<http://www.mineralogie.geowissenschaften.uni-muenchen.de/personen/phd/chevrel/index.html>

Education

Sept 2009 - Present PhD - Experimental Volcanology, *University of Munich (LMU), Germany*
2008 - 2009 Master 2nd year "Earth and Planetary Sciences", *University of Toulouse, France*
2007 - 2008 Master 1st year "Earth and Planetary Sciences", *University of Calgary, Canada*
2004 - 2007 Licence "Earth and Planetary Sciences", *University of Toulouse, France*
June 2004 Baccalaureate "Engineering Sciences, European language (Spanish)" *Lycée Déodat de Séverac, Toulouse, France*

Research

Sept 2009-present PhD in the Experimental Volcanology group with Prof. Donald. B. Dingwell and in collaboration with Dr. David Baratoux (IRAP, University of Toulouse): Rheology of Martian Lava Flows Derived from Experiments and Terrestrial Analogues.
Ludwig-Maximilians-University, München, Germany

January - June 2009 Master Thesis in the Laboratoire des Mécanismes et Transferts en Géologie (LMTG) with Prof. Anne Nédélec (University of Toulouse, France) and Dr. Jean-François Moyen (University of Stellenbosch, South Africa): Partial melting of Archean amphibolites from Barberton (South Africa).
LMTG, Toulouse, France

July - August 2008 Internship in the Institute for Study of the Earth's Interior (ISEI), Magma and Crystal Chemistry Group with Dr. Masami Kanzaki: In-situ Raman and IR spectroscopic study of hydrous GeO₂ glass under pressure.
ISEI, Misasa, Okayama University, Japan

February - April 2008 Rock analyses, use of electron microprobe and laser ablation ICP-MS with Dr. Paul Hoskin (University of Auckland, New Zealand): Silica-undersaturated volcanic rocks from eastern Anatolia, Turkey.
University of Calgary, Canada

Experimental work

2009 - present

- Silicate melts rheology: Viscosity measurements using the Concentric Cylinder method (Brookfield Rheometer). High-temperature furnaces (Deltec, Noberterm) equipped with gas-mixing line (CO-CO₂). Viscosity measurements by micro-penetration technique (push-rod Bähr 802 V dilatometer)
- Differential Scanning Calorimeter (NETZSCH DSC 404 Pegasus).
- Wave Dispersive electron microprobe analysis on a CAMECA SX100 scanning electron microprobe (SEM).

Sektion für Mineralogie, Petrologie und Geochemie, LMU, München, Deutschland

July - 2008 High pressure diamond cells; Internal High Pressure Vessel; Raman spectroscopy analyses
ISEI, Misasa, Okayama University, Japan

Fieldwork

August 2010 Ground-truth morphology, mapping, textural interpretation and sampling of lava flows and shield volcanoes. Use of Differential Global Positioning System in collaboration with E. Hauber (DLR-Berlin) and T.Platz (FU Berlin). *Western Volcanic Zone, Iceland*

June 2010	Sampling and texture interpretation of the Blue Dragon Lava flow and Geology of Yellow Stone, <i>Snake River Plain, Idaho, USA</i>
Sept 2008	Mapping of magmatic and metamorphic structures. <i>Cap de Creus, Spain</i>
Sept 2007	Ore deposit course: Contrasts in the geology and exploration of three Cordilleran mineral deposits. <i>Alberta and British Columbia, Canada</i>
August 2007	Geology and Structure course in the Rocky mountains, <i>Alberta and British Columbia, Canada</i>
2005-2007	Geology and Mapping course in the Pyrenees, <i>France</i>

Grants and Awards

2012	Registration Grant from IAVCEI for Cities on Volcanoes 7.
2012	Student grant from the European Space Agency to attend the European Geoscience Union General Assembly 2012.
2009 - 2012	Three years scholarship from the International Graduate School THESIS (Complex Processes in the Earth: Theory, Experiments, Simulations) of the Elite Network of Bavaria.
2011	Student poster award at the 9 th Silicate Melt Workshop. 'Physical properties of CaAl ₂ Si ₂ O ₈ -CaMgSi ₂ O ₆ -FeO-Fe ₂ O ₃ melts: analogues for extra-terrestrial basalt.'
2010	Student Travel Grant to attend the annual general meeting of the American Geophysical Union (AGU) 2010 fall meeting in San Francisco, for the poster presentation: 'Effect of Iron on Rheological Properties of Haplogranite Melt'

Membership

2010 - present	Member of the European Geophysical Union and American Geophysical Union
2005 - 2007	Member of Student Geological Association: MAGMA

Languages

Français	Mother's tongue
English	Fluent
Español	High school level
Deutsch	In progress

Publications

Chevrel M.O., Baratoux, D., Hess K-U, Dingwell, D. B., Viscous flow behaviour of tholeiitic and alkaline Fe-rich Martian Basalts. *Geochimica and Cosmochimica Acta*, in review, 2013.

Chevrel M.O., Platz T., Hauber E., Baratoux, D., Dingwell, D. B., Planetary lava flow rheology: a comparison of morphological and rheological methods. *Earth and Planetary Research Letters*, in review, 2013.

Chevrel M.O., Giordano D., Potuzak M. Courtial, P., Dingwell D.B. Physical properties of CaAl₂Si₂O₈-CaMgSi₂O₆-FeO-Fe₂O₃ melts: analogues for extra-terrestrial basalt. *Chemical Geology*, in press, 2012.

Kremers S., Hanson J.B., Lavallée Y. Hess K.-U., Chevrel M. O., J. Wassermann, Dingwell D.B. Shallow magma-mingling-driven Strombolian eruption at Mt. Yasur, Vanuatu. *Geophysical Research Letters*, VOL. 39, L21304, 2012

Nedelec A., Chevrel M.O., Moyen J-F., Ganne J., S. Fabre, TTGs in the making: natural evidence from Inyoni shear zone (Barberton, South Africa). vol. 153, Pages 25-38, *Lithos*, 2012.

